Escola Politécnica da Universidade de São Paulo

Departamento de Engenharia Mecânica

PMC-581 Projeto Mecânico II

"MODELAGEM DE JATOS DE REFRIGERAÇÃO"

Relatório Final

aluno : Jayson Lee 8238215

eng. mecânica - energia e fluidos

orientador : Prof. Dr. Marcos de Mattos Pimenta

dezembro/1992

Índice

1. INTRODUÇÃO

A energia liberada na câmara de combustão durante a queima de um combustível fornece o trabalho de impulsão do pistão e também um calor residual que é transmitido aos elementos circundantes à câmara como o pistão, a camisa, o conjunto de válvulas, o cabeçote e também aos gases de escape.

O pistão, geralmente de alumínio, recebe uma quantidade significativa desta energia que afeta a sua estrutura. As regiões do pistão que dissipam a maior parte deste calor são :

- zona de anéis;
- galeria;
- fundo do pistão (parte inferior).

Com o aumento de potência dos motores e consequente aumento do calor gerado para o pistão, o fluxo de calor na zona dos anéis demanda a utilização de novas tecnologias de fabricação como materiais mais resistentes e porta-anéis. Consequentemente o custo do produto final aumenta bastante. Deste modo, faz-se necessário o estudo de otimização de refrigeração na galeria e na parte inferior do pistão.

2. OBJETIVOS

O grande problema do estudo de transferência de calor no fundo do pistão é o desconhecimento da distribuição do coeficiente de troca de calor por convecção (**h**) ao longo de sua superfície. Este trabalho tem como principal objetivo estudar modelos de jatos de óleo em meio ar incidindo sobre superfícies côncavas e aquecidas de forma a simular o problema na parte inferior do pistão.

Os modelos estudados resultaram de uma pesquisa bibliográfica realizada em institutos de pesquisa, Escola Politécnica e Metal Leve S.A.. Estes modelos definem diversas formas de distribuição de **h**, cuja influência no perfil de temperaturas internas ao pistão e no fluxo de calor será avaliada através de aplicação numérica (método dos elementos finitos), verificando a validade dos modelos.

Esta análise através da simulação numérica permitirá a avaliação de dois pontos importantes para a refrigeração de pistões :

1. a influência da presença do jato de refrigeração no fundo do pistão no perfil de temperaturas e fluxo de calor no seu interior;

2. a influência da posição de impacto do jato livre sobre a superfície inferior do pistão.

3. DEFINIÇÃO DO PROBLEMA

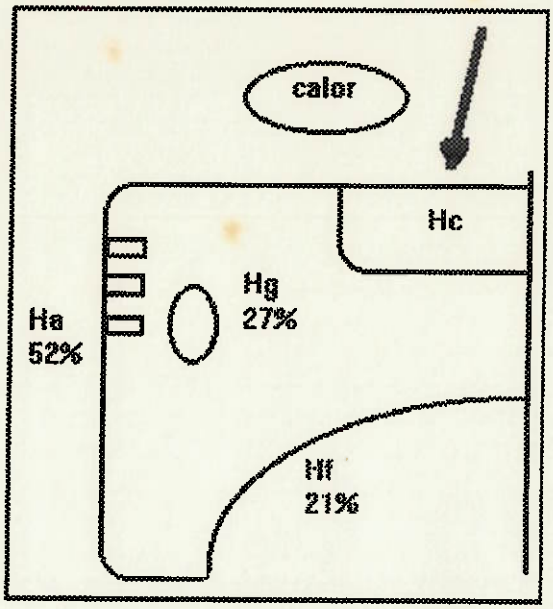

figura 3.1

Considerando a figura 3.1 (ref. [4]) verificamos que da fração de calor resultante do processo de combustão que penetra no pistão, grande parte é removida pela zona de anéis (52%) sendo a galeria responsável por 27% e a parte inferior do pistão por 21%, aproximadamente. Este calor deve ser removido com eficiência, visto que com o aumento de potência dos motores de combustão interna, a temperatura intena do pistão também aumentou, causando alteração nas propriedades mecânicas do material possibilitando a ocorrência de dilatação e danos estruturais ao conjunto.

O coeficiente de transferência de calor **h** neste trabalho é assumido como conhecido na câmara de combustão e na zona de anéis, sendo estes dados fornecidos por uma empresa de consultoria especializada em combustão. O valor adotado usualmente para o coeficiente de transferência de calor na parte inferior do pistão é um valor médio determinado experimentalmente sendo o objetivo deste trabalho a determinação da distribuição deste coeficiente ao longo da superfície interna ao pistão.

A simulação numérica será desenvolvida sobre a geometria de um pistão real já definido.

As condições de contorno do problema que devem ser consideradas no estudo dos modelos de jato para o fundo dos pistão são:

- jato único, líquido e circular;
- óleo em meio ar;
- número de Reynolds (Re) = 4000 (aproximado);
- número de Prandtl (Pr) = 200 (aproximado);
- superfície de impacto côncava;
- impacto não normal;
- distância bico X superfície variável.

4. ANÁLISE DO MATERIAL BILIOGRÁFICO

A pesquisa bibliográfica foi realizada a partir de uma busca de informações nas bibliotecas da *Metal Leve S.A.*, *Escola Politécnica da USP*, *Instituto de Pesquisas Tecnológicas (IPT)*, *Instituto de Pesquisa de Energia Nuclear (IPEN)*; com base em palavras chave e na referência [1].

A lista de referências obtidas encontra-se no apêndice I. Grande parte deste material foi descartado devido à não conformidade com o problema proposto (pistão) como os "arrays" (arranjos) de jatos, os "slot jets" (rasgos) e os jatos de aquecimento.

A partir da análise do material bibliográfico, cuja lista é apresentada no Apêndice I, alguns modelos para a distribuição do coeficiente de transferência de calor sobre uma superfície sólida foram selecionados para posterior análise numérica.

Woschni, em [2] encontra uma equação universal para a determinação do coeficiente médio de transferência de calor na câmara de combustão ou outro processo a volume constante. Em [3] é feita uma análise completa do fluxo de calor no interior do pistão e de temperaturas locais. Alguns experimentos foram feitos isolando-se partes do pistão (canal de anel, galeria de refrigeração, parte inferior) e avaliando as alterações nos resultados.

Sttoter [4] disserta sobre os métodos existentes para a refrigeração de pistões utilizando como fluido refrigerante água, ar e óleo.

A pesquisa bibliográfica (ref. [1]) é a base para este trabalho. Apresenta uma lista de 48 artigos sobre jatos de impacto, contendo o campo de aplicação (Re, Pr), a correlação utilizada, as condições do jato líquido e escoamento (aquecimento ou refrigeração, meio líquido ou gasoso,superfície plana ou inclinada) e o tipo do jato (arranjo, circular ou rasgo).

O uso de jatos de ar (gás) em meio gás considerando tanto os jatos únicos de rasgo ou circulares é estudado por *Martin* [5], calculando o coeficiente de transferência de calor a partir da analogia com a transferência de massa.

Stevens [6] estuda o desenvolvimento do perfil de velocidades tanto no escoamento sobre a superfície como no jato livre com o auxílio da técnica de LDV (Laser-Doppler Velocimetry).

Os autores das referências [7], [8] e [9] tratam do aumento do coeficiente de transferência de calor **h** através da presença de geradores de vórtices no escoamento.

Ward [10] determina o coeficiente de transferência de massa do impacto ortogonal de um jato de ar simples com "Swirl" sobre uma superfície plana através da técnica de "thin-film naphtalene sublimation". O coeficiente de transferência de calor é obtido pela analogia de Chilton-Colburn.

Na referência [11], *Chupp et Al.* tratam da refrigeração de pás de turbinas a gás através de impacto de jatos internos de ar.

Amano e *Brandt* [12] estudam a aplicação de jatos fluidos para cortar materiais sólidos. O estudo numérico é baseado na solução exata da equação de Navier - Stokes de um jato incompressível submerso com o modelo de turbulência k-ε. Neste trabalho observa-se a ocorrência de um 2° máximo no perfil de distribuição do coeficiente de descarga. Este fato pode ser explicado analiticamente pela presença de partículas de fluido com alta energia cinética.

Gardon e *Conboque* [13] estudam arranjos de jatos de ar com utilização voltada para o processo de endurecimento de vidro, variando experimentalmente a velocidade do ar desde poucos pés/min até velocidades sônicas. Apresentam uma correlação para o coeficiente de transferência de calor na região de estagnação e estabelecem uma relação para a sua determinação local em função da relação entre a distância radial e a distância entre o bico e a superfície de impacto.

Goldstein e *Timmers* [14] demonstram com experimentos práticos, a utilização da técnica de "liquid crystal" para a medição visual de temperaturas e consequentemente a determinação do coeficiente de transferência de calor em um prato plano sofrendo impacto de jatos de ar (simples e arranjos). O "liquid crystal" tem a propriedade de refletir determinadas cores do espectro de acordo com a temperatura. Sua faixa

de atuação nos experimentos é de 30 a 35 graus Celsius porém é sabido que já alcançou -40 a 285 graus Celsius.

Hricak [15] estuda a incidência de jatos circulares de ar em superfícies concavas, simulando em pequena escala um modelo de pá de turbina, obtendo uma correlação para a região de estagnação.

Beltaos [16] faz uma extensa análise do comportamento dinâmico do fluido em impacto de um jato turbulento circular.

Amano e *Sugiyama* [17] executam um estudo numérico de transferência de calor utilizando o modelo de viscosidade de Boussinesq (BMV) k-ε para solucionar a equação de Navier-Stokes. Os resultados de simulação numérica de 3 modelos diferentes são comparados com resultados experimentais, apresentando boa aproximação.

Daane e *Han* [18] conduziram um trabalho voltado para o processo de secagem de papel, avaliando a transferência de calor e massa envolvidas através de resultados experimentais de impacto de um jato turbulento de ar aquecido supondo a distância entre o bico e a superfície muito pequena.

Huang [19] investiga o processo de troca de calor em impacto normal de jatos de ar e determina equações empíricas para os coeficientes de transferência de calor local e médio. Estas equações são determinadas a partir de resultados experimentais de jatos de aquecimento atingindo uma superfície plana.

Fant [20] enfatiza o uso de jatos de impacto em refrigeração de pás de turbinas.

Donaldson e *Snedecker* [21] aproximam os resultados turbulentos perto da região se estagnação, pelos valores de um escoamento laminar, corrigidos por um fator de conversão. Os resultados analíticos são avaliados através de experiências utilizando ar. Vários parâmentros como variação radial e axial da velocidade, turbulência no ponto de estagnação, flutuação da pressão total e fluxo de calor foram medidos.

Wang et al [22] investigam as características de transferência de calor de um jato circular impactando sobre a superfície plana de um

disco sólido ao qual é atribuído uma temperatura arbitrária ou uma distribuição de fluxo de calor, sendo estes problemas solucionados analiticamente.

Gardon e *Akfirat* [23] avaliam o coeficiente de transferência de calor de jatos de impacto através de medições experimentais de velocidade e turbulência. Com isto é possível estudar a influência da turbulência nos valores locais de "h".

Sparrow et al [24] fazem um estudo de transferência de calor em impacto de jatos de ar em uma superfície plana com escoamento tal como no caso de refrigeração de pás de turbinas. Verificam também as influências da distância entre o jato e a superfície e da configuração da saída do jato nos valores de h local, experimentalmente através de medição de temperaturas locais.

Sparrow e *Lovell* [25] obtém dados experimentais sobre o impacto de um jato de ar circular sobre uma superfície plana em ângulos oblíquos (90^o - 30^o). Avaliação do coeficiente de transferência de massa através da técnica de sublimação de naftaleno a partir do princípio de que se os números de PRANDTL e SCHMIDT são iguais, para um dado escoamento (REYNOLDS), SHERWOOD e NUSSELT também são iguais; é possível estimar o coeficiente de transferência de calor. Neste trabalho verificou-se o fato de que o ponto de máximo (ponto de estagnação) é deslocado para a montante do escoamento à medida em que se diminui o ângulo de impacto. Isto, porém , não afeta significativamente o valor médio do coeficiente de transferência de calor.

Liu et al [26] apresentam um modelo para a distribuição de **h** para um escoamento laminar e turbulento a partir de impacto normal de jato líquido sobre uma superfície plana.

Stevens et al [27] apresentam um estudo que caracteriza o coeficiente de transferência de calor em impacto normal de um jato líquido e circular.

Hricak [28] estuda a transferência de calor em jatos de ar em meio ar que impactam sobre uma superfície hemisférica côncava, apresenando correlações para o coeficiente médio e no ponto de estagnação.

5.MODELOS ESCOLHIDOS

Os modelos propostos pelas referências [26], [27] e [28] foram escolhidas para a aplicação numérica pelos seguintes motivos :

- estudo de jato líquido (exceto [28]) e circular;
- impacto em superfície curva (em [28])
- apresentam correlações para a obtenção da distribuição de transferência de calor;
- estas correlações têm sua faixa de validade abrangendo as condições do problema (Re, Pr, d, Z);
- * comprovação experimental de seus resultados.
- A seguir, os modelos escolhidos são descritos sucintamente.

5.1.Modelo A

Liu et Al. [26] apresentam um modelo para a determinação do coeficiente de transferência de calor de um escoamento sobre uma superfície plana a partir da incidência normal de um jato líquido, circular, sem mudança de fase. O escoamento laminar é dividido em quatro fases diferentes, de acordo com a figura 5.1:

a) região de estagnação;

b) região onde nem a camada limite térmica nem a cinemática atingiram a superfície;

c) região onde a camada limite cinemática já atingiu a superfície e, por fim;

d) a região onde ambas as camadas limite atingiram a superfície.

As correlações desenvolvidas para cada uma das regiões bem como sua faixa de validade encontram-se na tabela 5.1. Em comparação com resultados experimentais, as correlações apresentaram erro menor que 10 %.

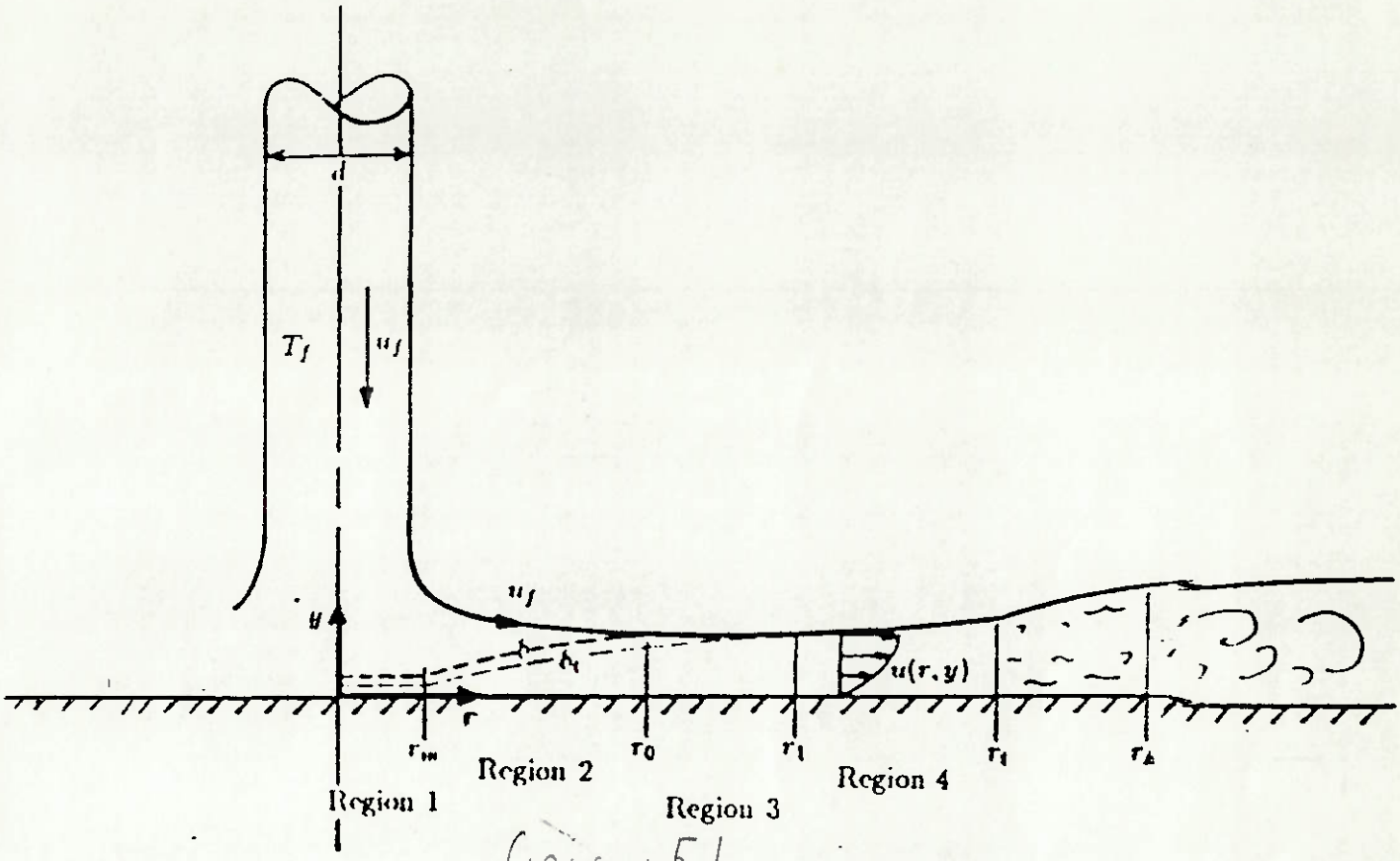

figura 5.1

Table 1 Suggested formulae for local Nusselt number for Pr ≥ O(1)

Region	Range	Nu_d
Stagnation zone	$0 \le r/d < 0.787, \quad 0.15 \le Pr \le 3$ $Pr > 3$	$0.715\,Re_d^{1/2}Pr^{0.4}$ $0.797\,Re_d^{1/2}Pr^{1/3}$
Transition: stagn. to b.l.	$0.787 < r/d < 2.23$	$\left(\frac{\frac{27}{80}Re_dPr\frac{r}{d}}{\frac{1}{2}\left(\frac{r}{d}\right)^3-0.2535}\right)^{1/3}$
b.l. region (2)	$2.23 < r/d < 0.1773\,Re_d^{1/3}$	$0.632\,Re_d^{1/2}Pr^{1/3}\left(\frac{d}{r}\right)^{1/2}$
Similarity region (3 & 4)	$0.1773\,Re_d^{1/3} < r/d < 1200\,Re_d^{-0.422}$ $(r_0/d < r/d < r_t/d)$	$\frac{0.407\,Re_d^{1/3}Pr^{1/3}\left(\frac{d}{r}\right)^{2/3}}{\left[0.1713\left(\frac{d}{r}\right)^2+\frac{5.147\,r}{Re_dd^2}\right]^{2/3}\left[\frac{1}{2}\left(\frac{r}{d}\right)^2+C_3\right]^{1/3}}$ $\left(C_3=\frac{0.267\,(d/r_0)^{1/2}}{\left[0.1713\left(\frac{d}{r_0}\right)^2+\frac{5.147\,r_0}{Re_dd^2}\right]^2}-\frac{1}{2}\left(\frac{r_0}{d}\right)^2\right)$
Transition: laminar/turb	$1200\,Re_d^{-0.422} < r/d < 2.86\times10^4\,Re_d^{-0.68}$	$Nu_{lam}(r_t)+[Nu_{turb}(r_h)-Nu_{lam}(r_t)]\frac{(r-r_t)}{(r_h-r_t)}$
Turbulent region	$r/d > 2.86\times10^4\,Re_d^{-0.68}$	$\frac{8\,Re_dPr\,f/(C_f,Pr)}{49(h/r)(r/d)+28(r/d)^2\,f/(C_f,Pr)}$

tabela 5.1

5.2.Modelo B

Stevens et Al [27] apresentam um outro modelo para o coeficiente de transferência de calor baseado no escoamento a partir do impacto normal sobre uma superfície plana com fluxo de calor constante de um jato líquido circular, fase única. Os parâmetros considerados experimentalmente são : número de Reynolds (Re), diâmetro do bico (d) e distância do bico até a superfície (z).As correlações obtidas encontram-se na tabela 5.2, bem como a faixa de validade. As correlações obtiveram erro percentual de 8 % em relação a experimentos realizados pelos autores.

Faixa de Aplicação :

Número de Reynolds (Re) 4000 - 52000

zona de estagnação

$$Nu_o = 2,67 \cdot \mathrm{Re}^{0,567} \cdot \mathrm{Pr}^{0,4} \cdot (Z/d)^{-0,0336} \cdot (V/d)^{0,237}$$

onde V é a velocidade de saída do jato.

Nusselt local

$$Nu / Nu_o = \{C^{-P} + f(r/d)^{-P}\}^{-1/P}$$

onde : P = 9,0

C = 1,0

$$f(r/d) = a' \cdot e^{b' \cdot (r/d)}$$

Diâmetro (mm)	2.20	2.30	4.10	5.80	8.90
a'	1.13	1.1411	1.34	1.48	1.57
b'	-0.23	-0.2395	-0.41	-0.56	-0.70

tabela 5.2

5.3.Modelo C

Outro modelo é proposto por Hricak [28] que estuda a transferência de calor com medição do perfil de velocidades e distribuição de pressão estática no impacto de jatos de ar em meio ar com as seguintes condições :

número de Reynolds (Re) : 1200 a 88000

relação entre a distância do jato e diâmetro (Zn/d) : 3 a 20

A partir de medições experimentais, Hricak observou que a curvatura da superfície de impacto não altera a troca de calor na região de estagnação.

As correlações apresentadas são :

1) Nusselt médio :

$$\overline{Nu_d} = 2{,}51 \cdot \mathrm{Re}_d^{\,0{,}604} \cdot \mathrm{Pr}^{0{,}33} \cdot (d/d_p)^{1{,}07}$$

2) Nusselt na zona de estagnação :

$$Nu_o = 0{,}798 \cdot \mathrm{Re}_d^{\,0{,}604} \cdot \mathrm{Pr}^{0{,}4} \cdot (Z_n/d)^{-0.22}$$

onde : d : diâmetro do bico;

d_p : diâmetro do prato (pistão);

Z_n :distância entre o bico e a superfície de impacto.

6.APLICAÇÃO NUMÉRICA

Após a escolha dos modelos, para simular numericamente a distribuição de temperaturas no pistão, construiu-se uma malha com a geometria de um pistão Diesel real para avaliar a validade dos modelos definidos em uma condição de Potência Máxima através do programa ANSYS versão 4.2.

6.1.EXECUÇÃO DA MALHA

O modelo Axissimétrico bidimensional (2-D) foi feito baseado nas informações contidas nas referências do Apêndice II.e com o suporte técnico dado pelos analistas da Metal Leve S.A.

Duas malhas foram geradas sendo a única diferença a presença da galeria de refrigeração.

O procedimento básico adotado para a construção da malha foi :

1) A partir dos desenhos de fabricação do pistão, escolheu-se pontos básicos (keypoints) que definem a geometria superficial do pistão;

2) Unido estes pontos com curvas ou retas, sempre seguindo à risca a geometria do pistão, obtemos um contorno fiel de sua forma (fig. 6.1);

3) A área interna deve, então, ser dividida em regiões, pois a discretização deve ser feita sobre uma área quadrilátera (fig. 6.2);

4) Definido o tipo de elemento para simulação (STiFF=55), discretiza-se cada região, escolhendo os números de subdivisões em cada face dos "quadriláteros" (fig. 6.3 e 6.4).

Prontas as malhas, deve-se associar as propriedades dos materiais (no caso, a condutividade térmica do alumínio e do porta anel) e também, determinar as condições de contorno, que para a simulação de distribuição de temperatura devem ser o coeficiente de película ***h*** e a temperatura da face para todas as superfícies do pistão, que são atribuídas à face de cada elemento definida entre 2 nós.

A simulação do tipo Kan=-1 (Distribuição de Temperatura) e o número de iterações (ITER) devem ser estabelecidos e o arquivo de entrada para a execução da simulação propriamente dita deve ser gerado a partir do comando AFWRITE (FILE27.DAT).

As condições de contorno aplicadas, incluindo-se um valor médio empírico para toda a parte inferior do pistão estão mostradas na tabela 6.1 a seguir, relacionada à figura 6.5, representando uma condição de potência máxima :

REGIÃO	H [W/MM².°C]	T[°C]
1	630E-6	850
2	915E-6	850
3	916E-6	850
4	631E-6	850
5	712E-6	160
6	4104E-6	160
7	11638E-6	160
8	712E-6	140
9	10000E-6	140
10	712E-6	130
11	4104E-6	130
12	712E-6	120
13	712E-6	110
14	712E-6	100
15	4200E-6	120

tabela 6.1

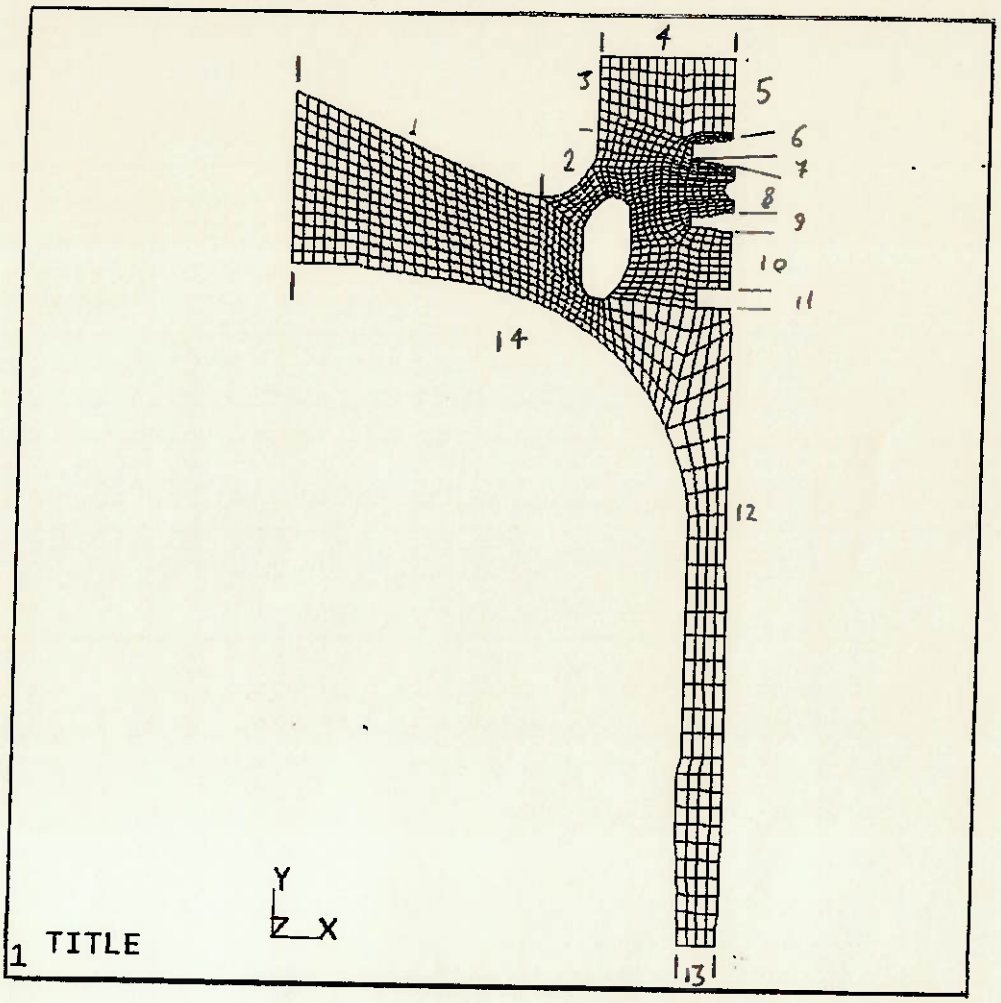

figura 6.5

6.2. DADOS NUMÉRICOS DO JATO

Os dados numéricos necessários para a aplicação numérica dos modelos estão listados abaixo :

diâmetro do pistão :	137	mm
distância do jato ao centro do pistão ($r_{impacto}$):	44,53	mm
altura de impacto no BDC (Z) :	54,65	mm
curso do pistão (h):	165	mm
diâmetro do Cooler Jet (d):	2,3	mm
temperatura do óleo :	100	°C
tipo de óleo :	15W - 40	
vazão de óleo :	4,8 (8.10^{-5})	litros/min.(m^3/s)
calor específico (Cp) :	2,219	kJ/kg.K
condutividade térmica do óleo ($k_{óleo}$):	0,137	W/m.°C
viscosidade cinemática do óleo (ν) :	$14,1.10^{-6}$	m^2/s
massa específica do óleo (ρ) :	847	kg/m^3
condutividade térmica do alumínio ($k_{alumínio}$) :	137	W/m.°C
condutividade térmica do aço ($k_{aço}$) :	40	W/m.°C
número de Reynolds :	Re	
número de Prandtl :	Pr	
número de Nusselt :	Nu	

Cálculo de parâmetros :

$$Q = \frac{V \cdot \pi \cdot d^2}{4} \Rightarrow V = \frac{4 \cdot Q}{\pi \cdot d^2}$$

$$\mathrm{Re} = \frac{V \cdot d}{\upsilon}$$

$$\therefore \mathrm{Re} = \frac{4 \cdot Q}{\upsilon \cdot \pi \cdot d} = 3140,9$$

$$\mathrm{Pr} = \frac{c_p \cdot \mu}{k} = \frac{c_p \cdot \upsilon \cdot \rho}{k} = 193,4$$

Velocidade de Saída do Jato : *V=19,2550 m/s*

6.3. APLICAÇÃO DOS MODELOS

Os modelos escolhidos devem ser adaptados às condições do problema de acordo com os dados da seção 6.2 e medidas inerentes à geometria do pistão escolhido, substituindo assim o valor constante da região 14 da tabela 6.1 (712E-06 W/mm².°C) atribuído pelo modelo atual à parte inferior do pistão.

O modelo A fornece correlações para o cálculo do número de Nusselt para diferentes regiões do escoamento assim como as amplitudes de validade das mesmas. O modelo B fornece uma correlação para o ponto de impacto (zona de estagnação) e uma função de dependência para o cálculo de Nusselt local. O modelo C também fornece uma correlação para a região de estagnação e outra para o cálculo do valor médio de Nusselt de acordo com o diâmetro total.

Os modelos A e B foram preparados em duas versões cada um : a 1º versão dos modelos considera a distância radial como o comprimento característico para cálculo, enquanto que a 2º versão considera a distância superficial para este fim. As distâncias radiais são tomadas em relação ao ponto de impacto.

Todos os cálculos estão demonstrados sucintamente a seguir.

6.3.1 Modelo A

Para este modelo os valores calculados são os mesmos para as duas versões (radial e superficial).

1. Stagnation Zone

$0 \le r/d \le 0,787$

$0 \le r \le 1,8101 mm$

$Nu_d = 0,797 \cdot \mathrm{Re}_d^{0,5} \cdot \mathrm{Pr}^{1/3}$

$Nu_d = 258,3078$

$h = 15386,16\ W/m^2.°C$

3.Boundary Layer

$2,23 \le r/d \le 0,1773 \cdot \mathrm{Re}_d^{1/3} = 2,5965$

$5,1290 \le r \le 5,9720 mm$

$r_{médio} = 5,5505$

$Nu_d = 0,632 \cdot \mathrm{Re}_d^{1/2} \cdot \mathrm{Pr}^{1/3} \cdot \left(\frac{d}{r}\right)^{1/2} = 131,8543$

$h = 7853,93 W/m^2 \cdot^o C$

4.Similarity Region

$2,5965 \le r/d \le 1200 \cdot \mathrm{Re}_d^{-0,422} = 40,1259$

$5,9720 \le r \le 92,2896 mm$

$r_{médio} = 49,1308mm$

$$Nu_d = \frac{0,407 \cdot \mathrm{Re}_d^{1/3} \cdot \mathrm{Pr}^{1/3} \cdot \left(\frac{d}{r}\right)^{2/3}}{\left[0,1713 \cdot \left(\frac{d}{r}\right)^2 + \frac{5,147 \cdot r}{\mathrm{Re}_d \cdot d}\right]^{2/3} \cdot \left[C_3 + \frac{1}{2} \cdot \left(\frac{r}{d}\right)^2\right]^{1/3}}$$

$$C_3 = \frac{0,267 \cdot \left(\frac{d}{r_o}\right)^{1/2}}{\left[0,1713 \cdot \left(\frac{d}{r_o}\right)^2 + \frac{5,147 \cdot r_o}{\mathrm{Re}_d \cdot d}\right]^2} - \frac{1}{2} \cdot \left(\frac{r_o}{d}\right)^2$$

$Nu_d = 5,5785$

$h = 332,28 W/m^2 .^o C$

5.Transition Laminar to Turbulent

$1200 \cdot \mathrm{Re}_d^{-0,422} = 40,1259 \le r/d \le 2,8 \cdot 10^4 \cdot \mathrm{Re}_d^{-0,68} = 117,2631$

$92,2896 \le r \le 269,7051mm$

$r = 180,9974mm$

$$Nu_d = Nu_{lam.}(r_t) + \left[Nu_{turb}(r_h) - Nu_{lam.}(r_t)\right] \cdot \frac{(r - r_t)}{(r_h - r_t)}$$

$Nu_{lam}(r_t)$

$r = r_t = 92,2896mm \rightarrow r_t/d = 40,1259$

$$Nu_d = \frac{0,407 \cdot \mathrm{Re}_d^{1/3} \cdot \mathrm{Pr}^{1/3} \cdot \left(\frac{d}{r}\right)^{2/3}}{\left[0,1713 \cdot \left(\frac{d}{r}\right)^2 + \frac{5,147 \cdot r}{\mathrm{Re}_d \cdot d}\right]^{2/3} \cdot \left[C_3 + \frac{1}{2} \cdot \left(\frac{r}{d}\right)^2\right]^{1/3}}$$

$C_3 = 184,9388$

$\therefore Nu_d = 1,8093$

$Nu_{turb}(r_h)$

$r_h = 269,7051mm$

$r_h/d = 117,2631$

$$Nu_d = \frac{8 \cdot \mathrm{Re}_d \cdot Pf \cdot f(C_f, \mathrm{Pr})}{49 \cdot \left(\frac{h}{r}\right) \cdot \left(\frac{r}{d}\right) + 28 \cdot \left(\frac{r}{d}\right)^2 \cdot f(C_f, \mathrm{Pr})}$$

$$C_f = 0,073 \cdot \mathrm{Re}_d^{-1/4} \cdot \left(\frac{r}{d}\right)^{1/4} = 0,0321$$

$$h = d \cdot \left(\frac{0,02091}{\mathrm{Re}_d^{1/4}} \cdot \left(\frac{r}{d}\right)^{5/4} + C \cdot \frac{d}{r} \right)$$

$$onde\ C = 0,1713 + \frac{5,147 \cdot r_t}{\mathrm{Re}_d \cdot d} - \frac{0,02091}{\mathrm{Re}_d^{1/4}} \cdot \left(\frac{r_t}{d}\right)^{1/4} = 0,23$$

$h = 2,4835mm$

$$f(C_f, \mathrm{Pr}) = St = \frac{C_f}{2} \cdot \frac{1}{1,07 + 12,7 \cdot (\mathrm{Pr}^{2/3} - 1) \cdot \sqrt{\frac{C_f}{2}}} = 0,0003$$

$\therefore Nu_d = 0,2062$

Portanto para a Região de Transição :

Nu_d=1,0078
h=60,03 W/m².°C

6.3.2 Modelo B

Neste nodelo os cálculos para as duas versões diferenciam-se nas regiões mais afastadas do ponto de impacto. A partir da aplicação das fórmulas abaixo, obtemos os valores para a região de estagnação e regiões afastadas da seguinte maneira :

zona de estagnação

$$Nu_o = 2,67 \cdot \mathrm{Re}^{0,567} \cdot \mathrm{Pr}^{0,4} \cdot (Z/d)^{-0,0336} \cdot (V/d)^{0,237}$$

Nusselt local

$$Nu / Nu_o = \{C^{-P} + f(r/d)^{-P}\}^{-1/P}$$

onde : $P = 9,0$

$C = 1,0$

$f(r/d) = a' \cdot e^{b' \cdot (r/d)}$

Diâmetro (mm)	2.20	2.30	4.10	5.80	8.90
a'	1.13	1.1411	1.34	1.48	1.57
b'	-0.23	-0.2395	-0.41	-0.56	-0.70

tabela 6.2

Versão 1

Região de Estagnação :

$r/d = 0,75$

$0 \le r \le 1,725mm$

$z/d = 23,7609$

$V/d = 8371,7381s^{-1}$

$\therefore Nu_o = 222,8370$

$h = 13273,33W/m^{2}.^{o}C$

Valores Locais :

Região A

$1,725 \le r \le 5mm$

$r_{médio} = 3,3625mm$

$f(r,d) = 0,8040$

$Nu/Nu_o = 0,7928$

$\therefore h = 10517,79W/m^2.^oC$

Região B

$15 \le r \le 10mm$

$r_{médio} = 7,5mm$

$f(r,d) = 0,5226$

$Nu/Nu_o = 0,5224$

$\therefore h = 6933,99W/m^2.^oC$

Região C Centro

$10 \le r \le 44,53mm$

$r_{médio} = 27,265mm$

$f(r,d) = 0,0660$

$Nu/Nu_o = 0,0660$

$h = 876,04W/m^2.^oC$

Região C Saia

$10 \le r \le 18,07mm$

$r_{médio} = 14,035mm$

$f(r,d) = 0,2646$

$Nu/Nu_o = 0,2646$

$\therefore h = 3512,12W.m^{2}.^{o}C$

Versão 2

Região de Estagnação :

$r/d = 0,75$

$0 \le r \le 1,725mm$

$z/d = 23,7609$

$V/d = 8371,7381s^{-1}$

$\therefore Nu_o = 222,8370$

$h = 13273,33W/m^{2}.^{o}C$

Valores Locais :

Região A

$1,725 \le r \le 5mm$

$r_{médio} = 3,3625mm$

$f(r,d) = 0,8040$

$Nu/Nu_o = 0,7928$

$\therefore h = 10517,79W/m^{2}.^{o}C$

Região B Centro

$5 \le r \le 18,19mm$

$r_{médio} = 11,365mm$

$f(r,d) = 0,3044$

$Nu/Nu_o = 0,3044$

$\therefore h = 4040,15W/m^2.^oC$

Região B Saia

$5 \le r \le 37,39mm$

$r_{médio} = 21,195mm$

$f(r,d) = 0,0995$

$Nu/Nu_o = 0,0995$

$\therefore h = 1321,16W/m^2.^oC$

Região C Centro

$18,19 \le r \le 46,54mm$

$r_{médio} = 35,365mm$

$f(r,d) = 0,0271$

$Nu/Nu_o = 0,0271$

$h = 876,04W/m^2.^oC$

Região C saia

$37,39 \le r \le 100,86$

$r_{médio} = 69,125mm$

$f(r,d) = 0,0004$

$Nu/Nu_o = 0,0004$

$\therefore h = 4,98W.m^2.^oC$

6.3.3 Modelo C

Neste modelo são calculados os valores para o coeficiente de transferência de calor no ponto de estagnação e um valor médio para os outros pontos da superfície.

Zona de Estagnação

$$Nu_o = 0,798 \cdot \mathrm{Re}_d^{\,0,604} \cdot \mathrm{Pr}^{0,4} \cdot \left(\frac{Z_n}{d}\right)^{-0,22}$$

$$Nu_o = 422,78$$

$$\therefore h = 25183,09 W/m^2.^oC$$

Nusselt Médio

$$Nu_{médio} = 2,51 \cdot \mathrm{Re}_d^{\,0,604} \cdot \mathrm{Pr}^{0,33} \cdot \left(\frac{d}{d_p}\right)^{1,07}$$

$$Nu_{médio} = 53,84$$

$$\therefore h_{médio} = 3207,2 W/m^2.^oC$$

6.3.4 Resumo

Em resumo obtemos os seguintes dados para a execução numérica (tabelas 6.3) :

Nó	r (mm)	Liu - v1
313 - 336	-44,53 a -5,972	332.28
336 - 351	-5,972 a -5,129	7853.93
351 -393	-5,129 a -1,8101	10798.57
393 - 996	-1,8101 a 1,8101	15386.16
996 - 1035	1,8101 a 5,129	10798.57
1035 - 1036	5,129 a 5,972	7853.93
1036 - 1188	5,972 a 18,07	332.28

Nó	r (mm)	Liu - v2
313 - 365	-46,54 a -5,972	332.28
365 - 379	-5,972 a -5,129	7853.93
379 -407	-5,129 a -1,8101	10798.57
407 - 996	-1,8101 a 1,8101	15386.16
996 - 1035	1,8101 a 5,129	10798.57
1035 - 1036	5,129 a 5,972	7853.93
1036 - 1188	5,972 a 100,86	332.28

Nó	r (mm)	Stevens - v1
313 - 334	-44,53 a -10	876.04
334 - 337	-10 a -5	6933.99
337 -379	-5 a -1,725	10517.79
379 - 996	-1,725 a 1,725	13273.33
996 - 1035	1,725 a 5	10517.79
1035 - 1039	5 a 10	6933.99
1039 - 1188	10 a 18,07	3512.12

Nó	r (mm)	Stevens - v2
313 - 333	-46,54 a -18,19	359.85
333 - 337	-18,19 a -5	4040.15
337 - 379	-5 a -1,725	10517.79
379 - 996	-1,725 a 1,725	13273.33
996 - 1035	1,725 a 5	10517.79
1035 - 1036	5 a 18,19	1321.16
1036 - 1188	18,19 a 100,86	4.98

Nó	r (mm)	Hricak
313 - 393	-44,53 a -1,725	3207.2
393 - 996	-1,725 a 1,725	25183.09
1036 - 1188	1,725 a 18,07	3207.2

Obs. : Valores em W/m².°C

Obs. : r (mm) é a distância em relação ao ponto de impacto com valores negativos para o lado do centro do pistão

tabelas 6.3

7. RESULTADOS

7.1. Modelagem de Jatos de Refrigeração

Escolhidos e definidos os modelos, a simulação numérica foi executada e os perfis obtidos para cada caso para as duas geometrias, assim como tabelas comparativas de valores pontuais de temperatura em pontos estratégicos do pistão.

Os perfis de temperatura gerados estão apresentados nas figuras 7.1 a 7.12, as temperaturas pontuais estão apresentadas nas tabelas 7.1 a 7.3 e os valores médios dos coeficientes de transferência de calor estão no gráfico 7.1.

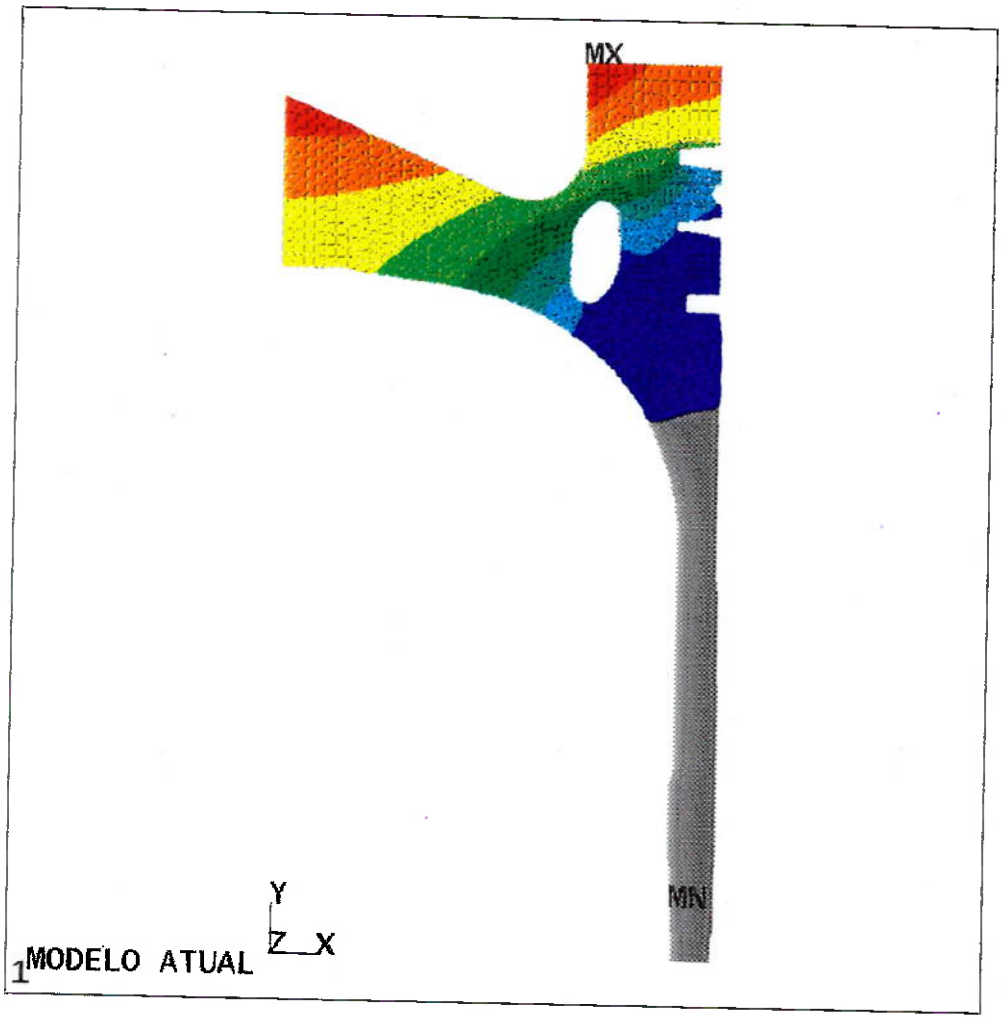
MX
MN
Y
Z
X
1
MODELO ATUAL
ANSYS 4.2
NOV 24 1992
16:00:46
POST1 STRESS
STEP=1
ITER=1
TEMP
ZV=1
DIST=75.9
XF=34.4
YF=69
MX=319
MN=113
135
158
181
204
227
250
273
296
319

figura 7.1

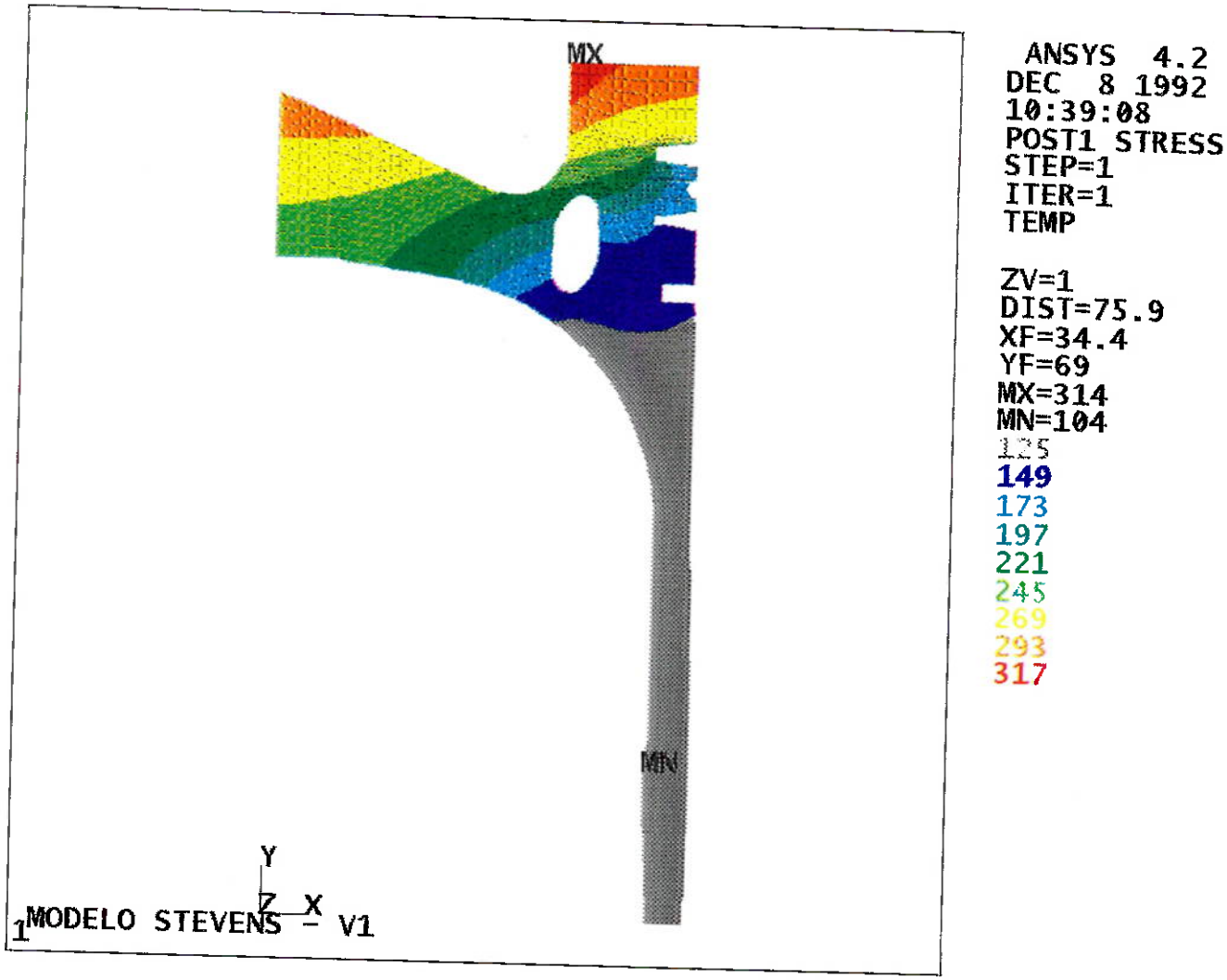
MX
MN
Y
Z X
1MODELO STEVENS - V1
ANSYS 4.2
DEC 8 1992
10:39:08
POST1 STRESS
STEP=1
ITER=1
TEMP
ZV=1
DIST=75.9
XF=34.4
YF=69
MX=314
MN=104
125
149
173
197
221
245
269
293
317

figura 7.2

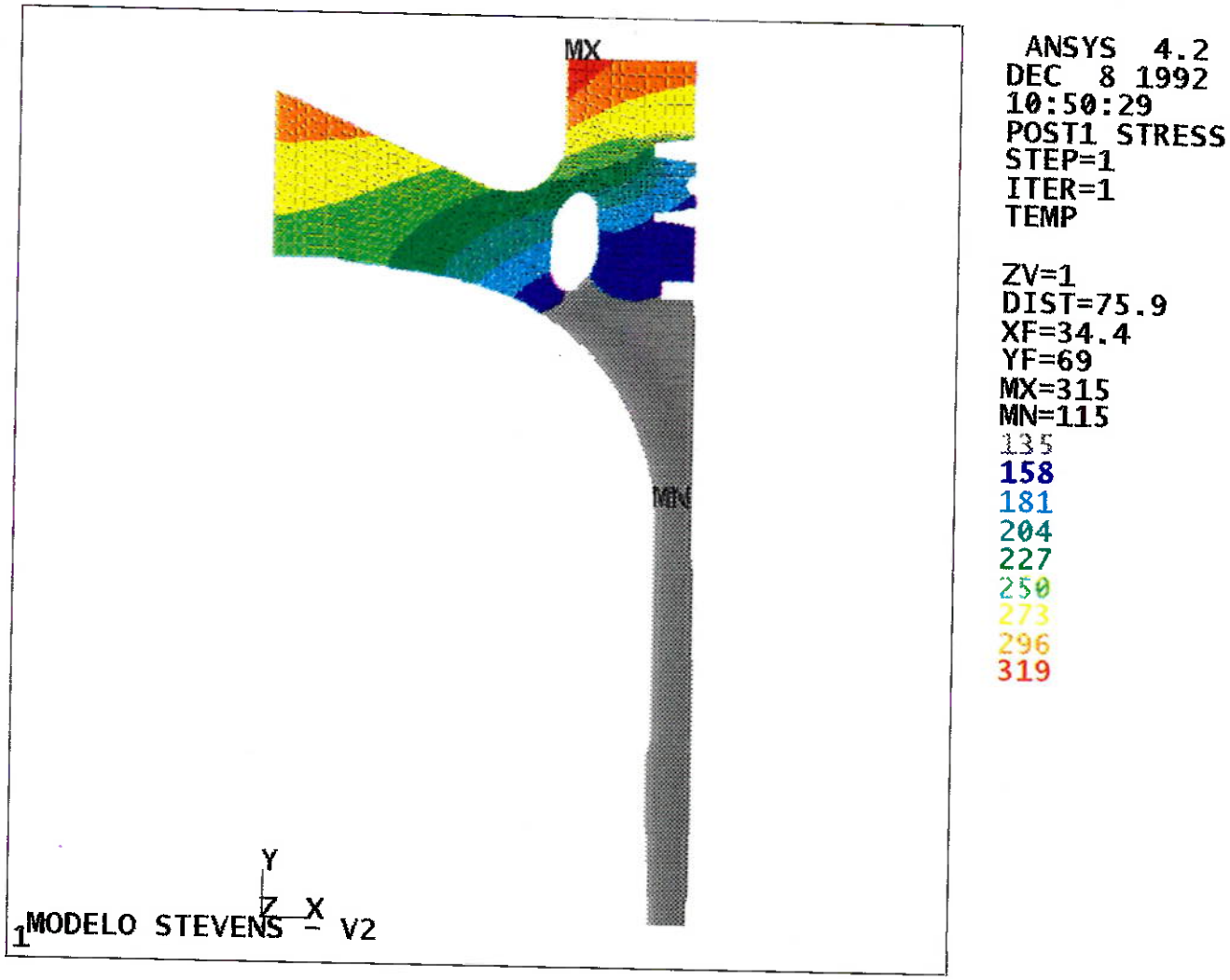
MX
MN
Y
Z
X
1
MODELO STEVENS - V2
ANSYS 4.2
DEC 8 1992
10:50:29
POST1 STRESS
STEP=1
ITER=1
TEMP
ZV=1
DIST=75.9
XF=34.4
YF=69
MX=315
MN=115
135
158
181
204
227
250
273
296
319

figura 7.3

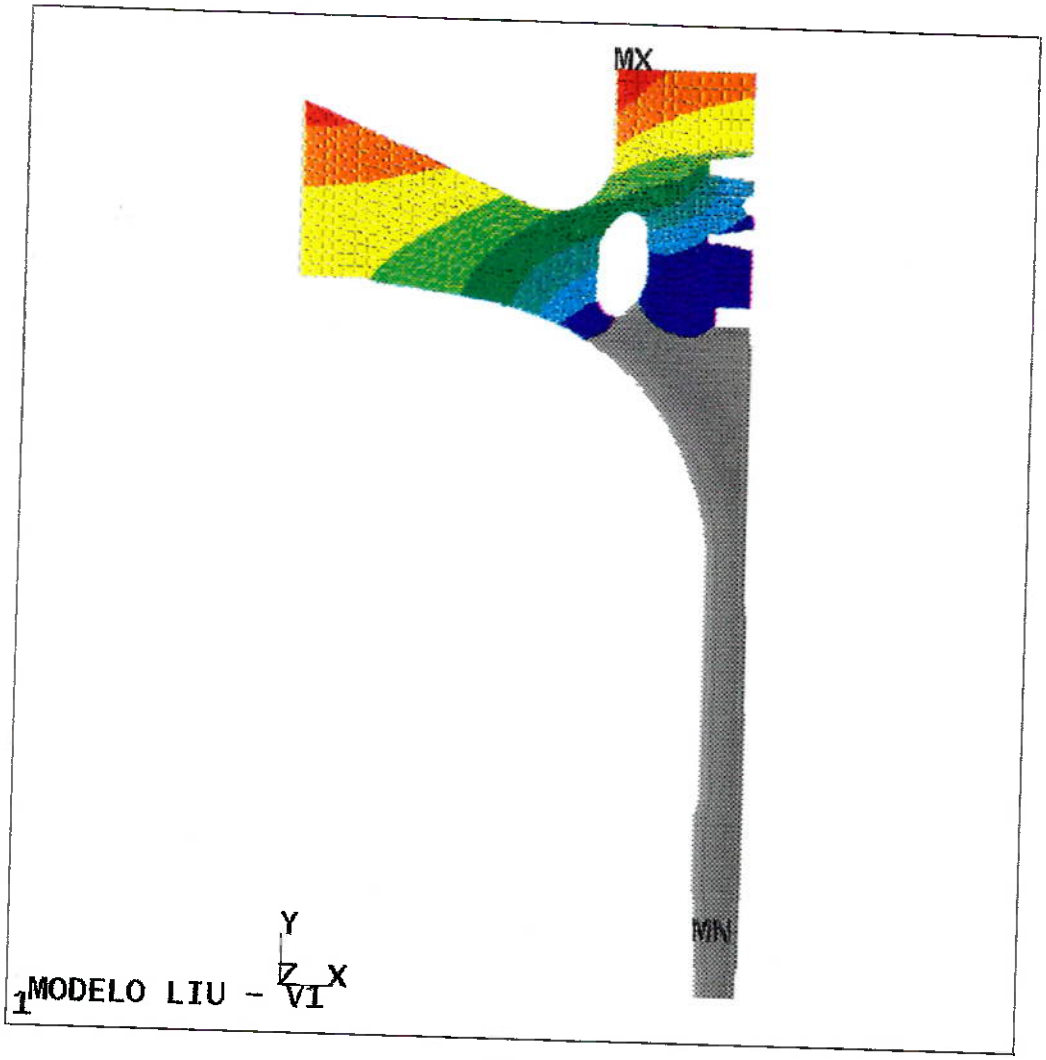
MX
MN
Y
Z
X
1
MODELO LIU - VI
ANSYS 4.2
DEC 8 1992
10:26:15
POST1 STRESS
STEP=1
ITER=1
TEMP
ZV=1
DIST=75.9
XF=34.4
YF=69
MX=316
MN=116
136
159
182
205
228
251
274
297
320

figura 7.4

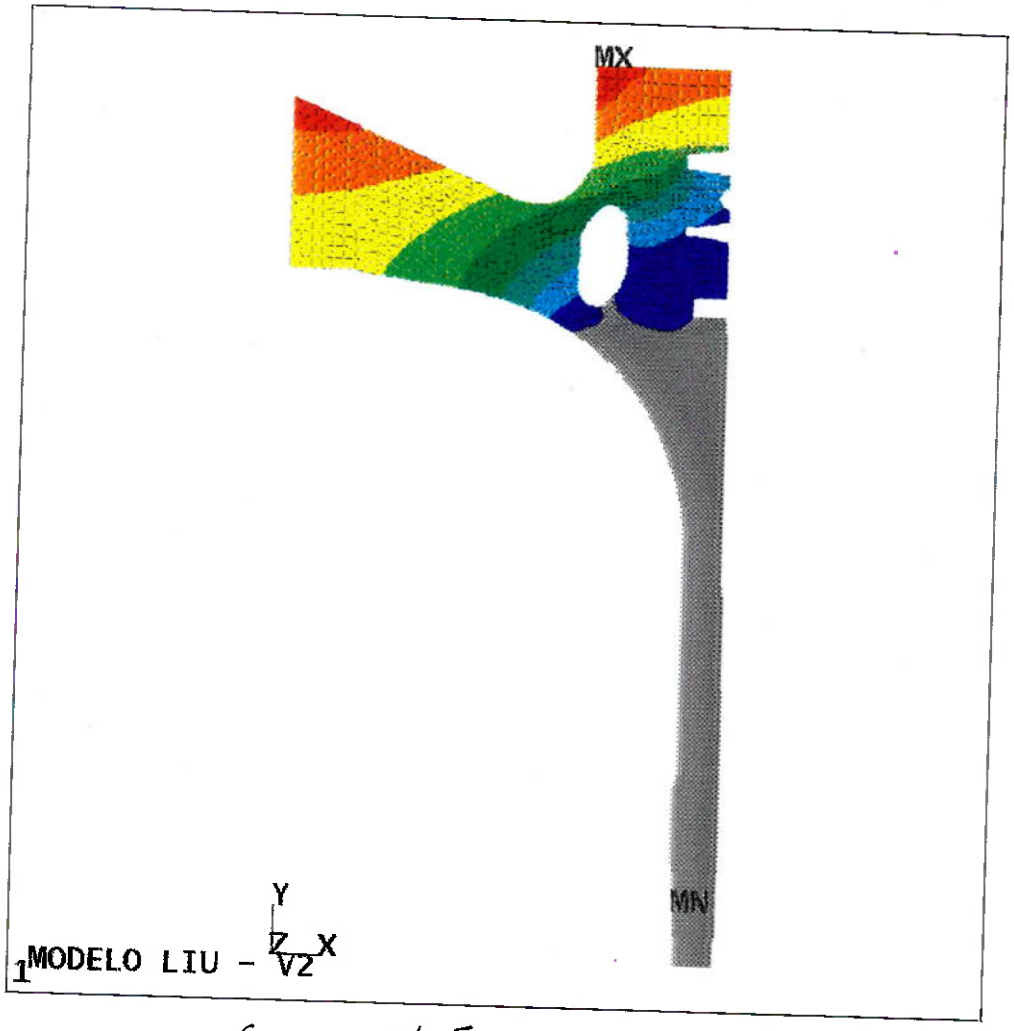
MX
MN
Y
Z
X
V2
1MODELO LIU -
ANSYS 4.2
NOV 25 1992
13:47:03
POST1 STRESS
STEP=1
ITER=1
TEMP
ZV=1
DIST=75.9
XF=34.4
YF=69
MX=317
MN=116
136
159
182
205
228
251
274
297
320

figura 7.5

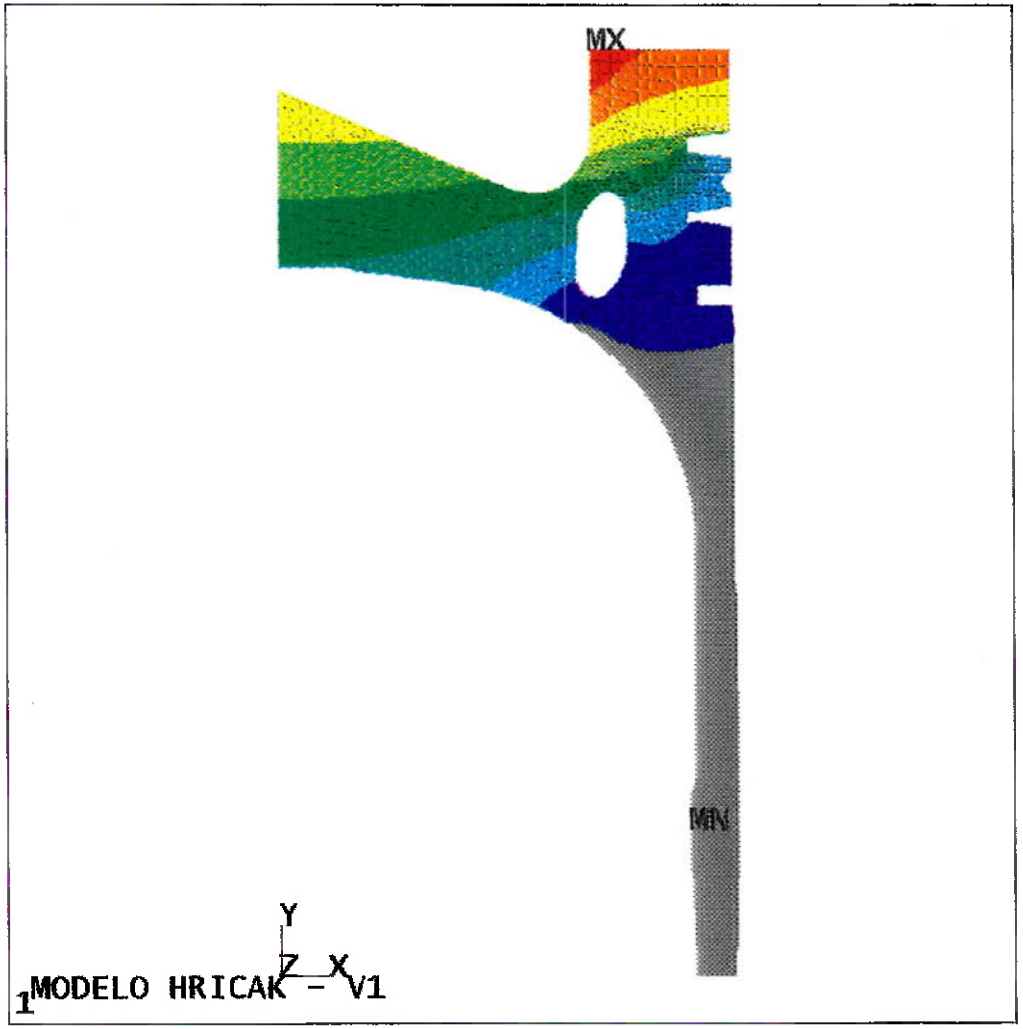

ANSYS 4.2
DEC 8 1992
10:58:39
POST1 STRESS
STEP=1
ITER=1
TEMP

ZV=1
DIST=75.9
XF=34.4
YF=69
MX=313
MN=104
125
149
173
197
221
245
269
293
317

figura 7.6

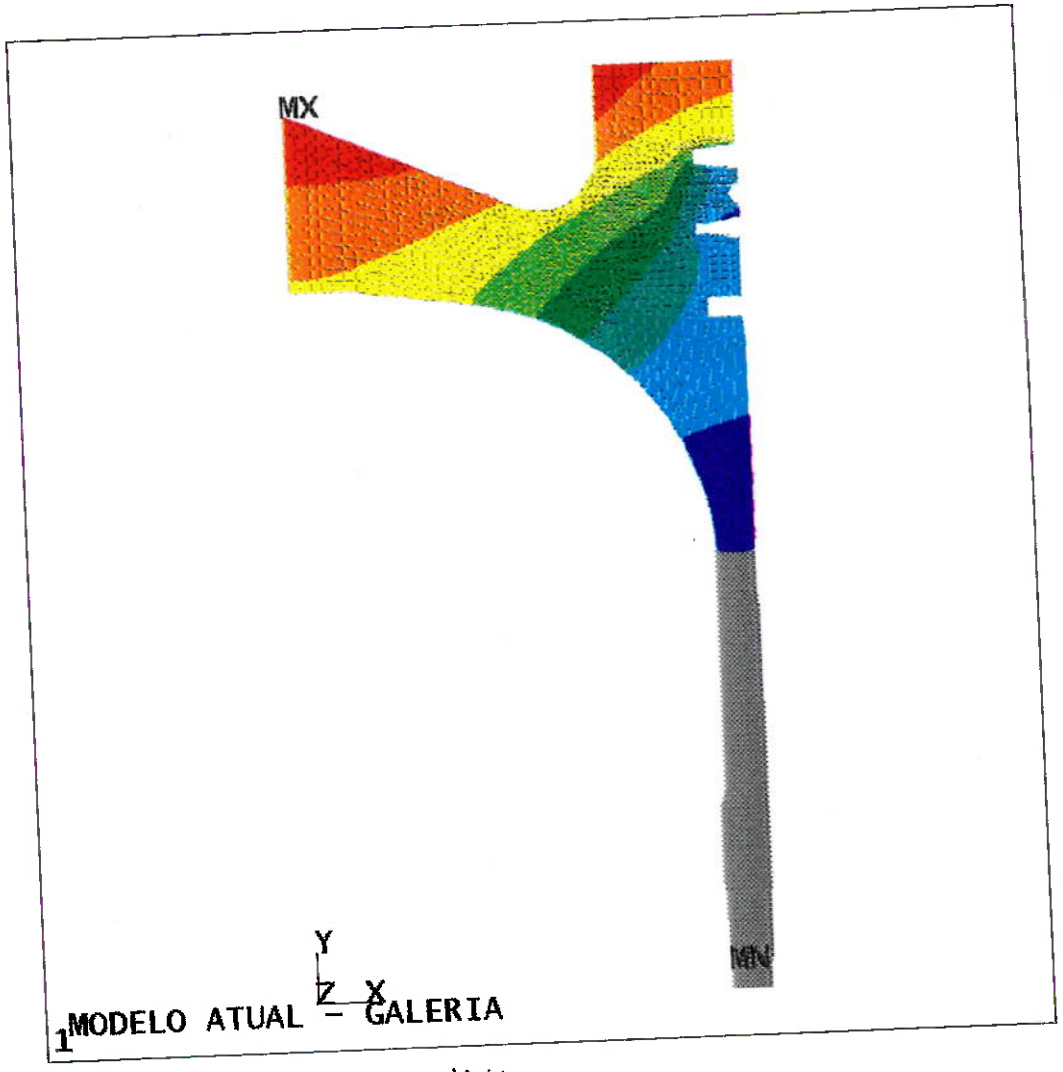
MX
MN
Y
Z X
1 MODELO ATUAL - GALERIA
ANSYS 4.2
DEC 8 1992
11:06:28
POST1 STRESS
STEP=1
ITER=1
TEMP
ZV=1
DIST=75.9
XF=34.4
YF=69
MX=346
MN=115
139
165
191
217
243
269
295
321
347

figura 7.7

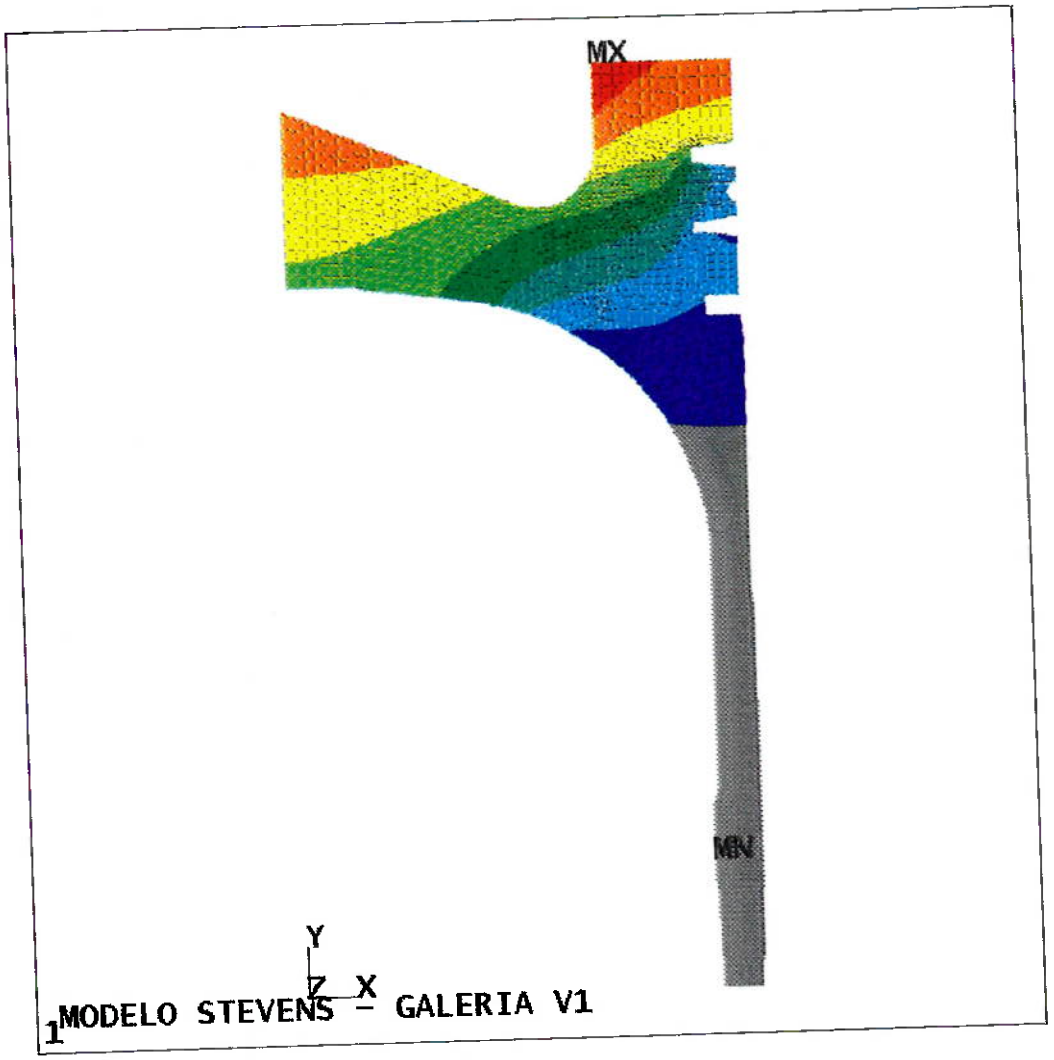
MX
MN
Y
Z
X
1
MODELO STEVENS – GALERIA V1
ANSYS 4.2
DEC 8 1992
11:31:59
POST1 STRESS
STEP=1
ITER=1
TEMP
ZV=1
DIST=75.9
XF=34.4
YF=69
MX=326
MN=104
128
153
178
203
228
253
278
303
328

figura 7.8

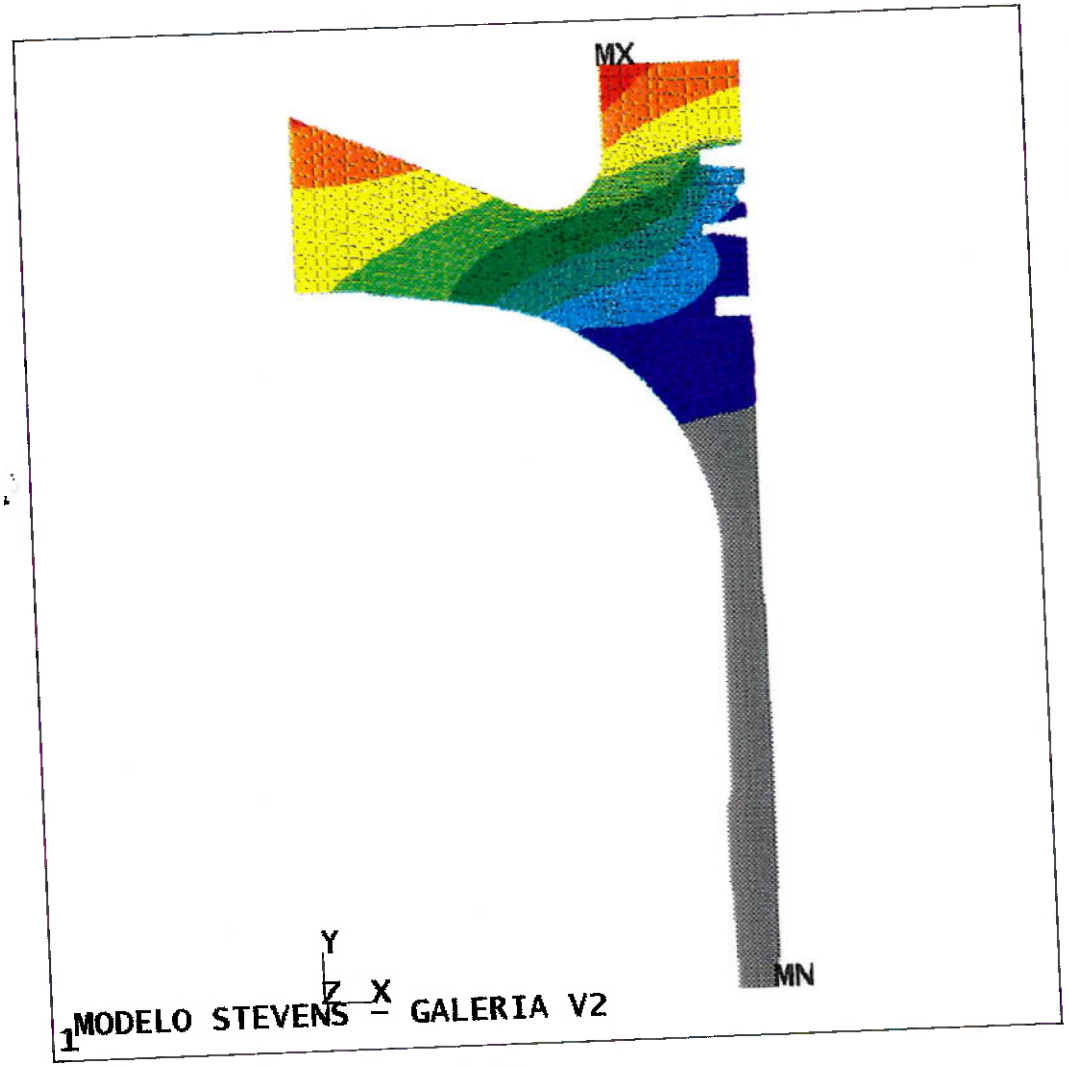
MX
MN
Y
Z
X
1
MODELO STEVENS - GALERIA V2
ANSYS 4.2
DEC 8 1992
11:42:00
POST1 STRESS
STEP=1
ITER=1
TEMP
ZV=1
DIST=75.9
XF=34.4
YF=69
MX=330
MN=121
141
165
189
213
237
261
285
309
333

figura 7.9

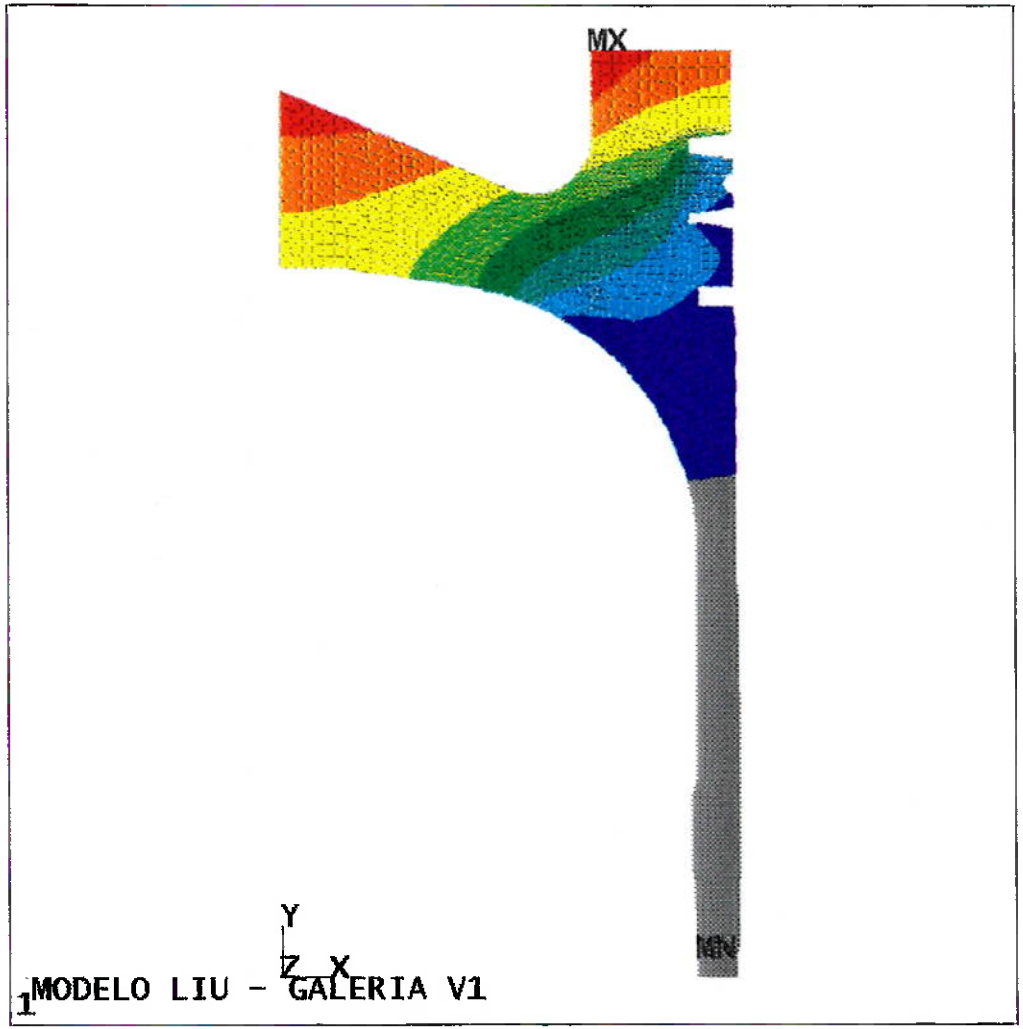

ANSYS 4.2
DEC 8 1992
11:14:55
POST1 STRESS
STEP=1
ITER=1
TEMP

ZV=1
DIST=75.9
XF=34.4
YF=69
MX=332
MN=118
141
165
189
213
237
261
285
309
333

figura 7.10

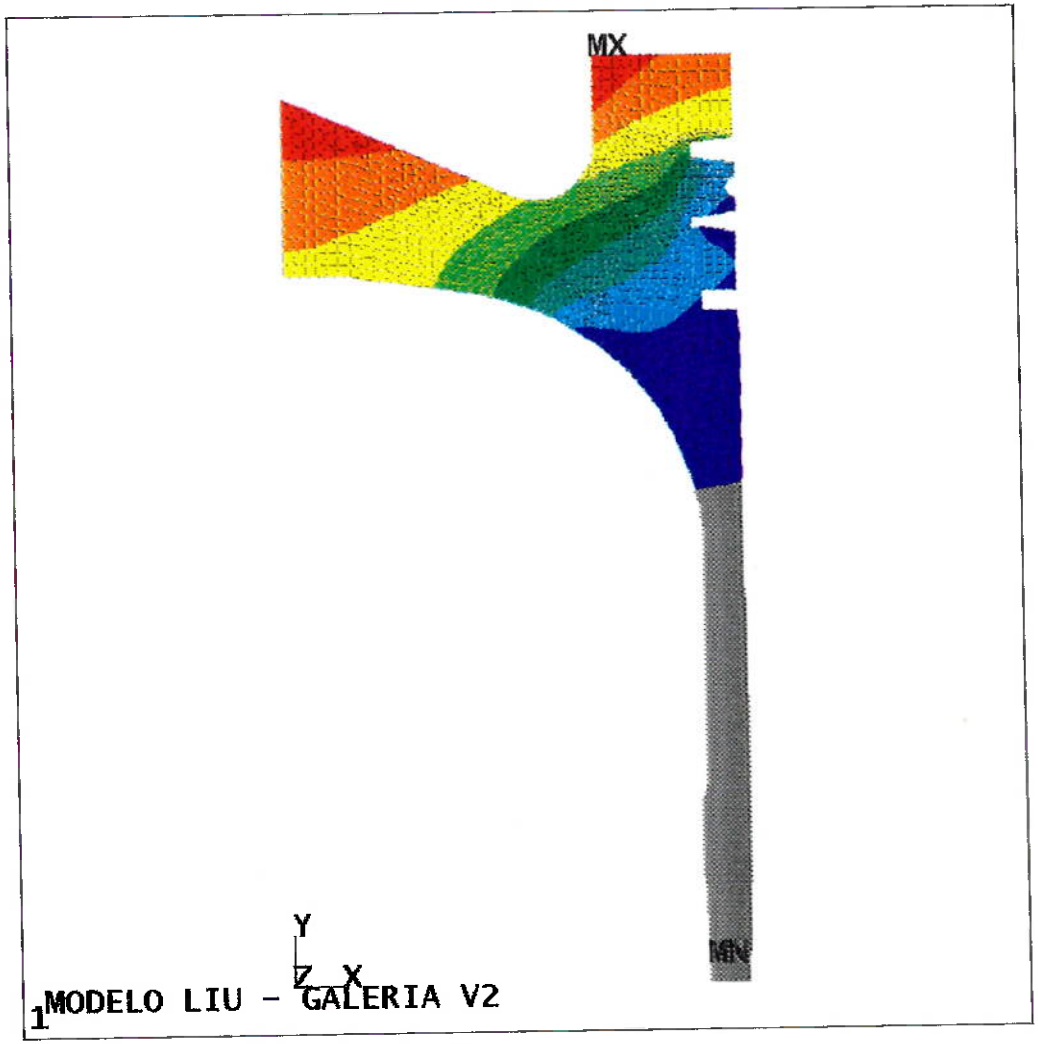

ANSYS 4.2
DEC 8 1992
11:23:58
POST1 STRESS
STEP=1
ITER=1
TEMP

ZV=1
DIST=75.9
XF=34.4
YF=69
MX=334
MN=118
142
166
190
214
238
262
286
310
334

figura 7.11

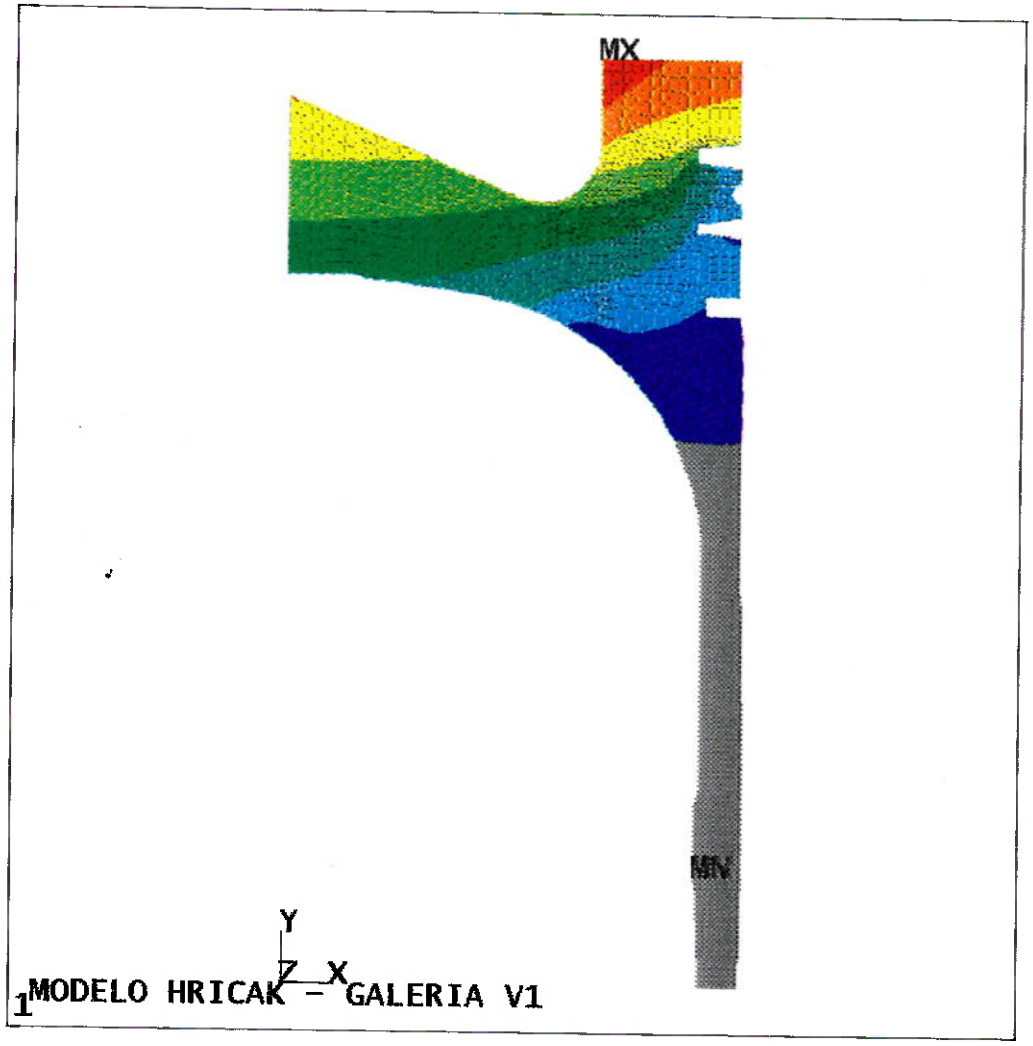

ANSYS 4.2
DEC 8 1992
11:49:58
POST1 STRESS
STEP=1
ITER=1
TEMP

ZV=1
DIST=75.9
XF=34.4
YF=69
MX=325
MN=105
127
152
177
202
227
252
277
302
327

figura 7.12

Distribuição de Temperaturas Pontuais - com Galeria

	Medido	Liu - v1	erro (%)	Liu - v2	erro (%)	Stevens - v1	erro (%)	Stevens - v2	erro (%)	Hricak	erro (%)
Borda de Câmara	280.4	297.3	6%	298.1	6.31%	295.0	5.21%	296.0	5.56%	294.1	4.89%
Centro da Câmara	271.0	294.8	8.78%	299.2	10.41%	277.6	2.44%	283.3	4.54%	254.7	-6.01%
1a Canaleta	247.3	244.0	-1.33%	244.8	-1.01%	241.6	-2.30%	242.6	-1.90%	240.8	-2.63%
Topo da Galeria	220.2	223.6	1.54%	224.9	2.13%	219.9	-0.14%	221.3	0.50%	218.3	-0.86%
Fundo da Galeria	160.3	131.1	-18.22%	133.5	-16.72%	125.3	-21.83%	130.1	-18.84%	125.0	-22.02%
Galeria Interior	184.5	140.9	-23.63%	146.7	-20.49%	133.8	-27.48%	139.5	-24.39%	131.8	-28.56%
Galeria Exterior	175.8	156.8	-10.81%	157.6	-10.35%	153.1	-12.91%	155.4	-11.60%	153.1	-12.91%
Centro do Undercrown	204.9	258.2	26.01%	262.8	28.26%	237.2	15.76%	245.7	19.91%	204.9	0.00%

tabela 7.1

Distribuição de Temperaturas Pontuais - com Galeria

	Atual	Liu - v1	erro (%)	Liu - v2	erro (%)	Stevens - v1	erro (%)	Stevens - v2	erro (%)	Hricak	erro (%)
Borda de Câmara	300.3	297.3	-1%	298.1	-0.73%	295.0	-1.76%	296.0	-1.43%	294.1	-2.06%
Centro da Câmara	300.7	294.8	-1.96%	299.2	-0.50%	277.6	-7.68%	283.3	-5.79%	254.7	-15.30%
1a Canaleta	247.1	244.0	-1.25%	244.8	-0.93%	241.6	-2.23%	242.6	-1.82%	240.8	-2.55%
Topo da Galeria	228.1	223.6	-1.97%	224.9	-1.40%	219.9	-3.59%	221.3	-2.98%	218.3	-4.30%
Fundo da Galeria	153.7	131.1	-14.70%	133.5	-13.14%	125.3	-18.48%	130.1	-15.35%	125.0	-18.67%
Galeria Interior	171.9	140.9	-18.03%	146.7	-14.66%	133.8	-22.16%	139.5	-18.85%	131.8	-23.33%
Galeria Exterior	162.6	156.8	-3.57%	157.6	-3.08%	153.1	-5.84%	155.4	-4.43%	153.1	-5.84%
Centro do Undercrown	261.9	258.2	-1.41%	262.8	0.34%	237.2	-9.43%	245.7	-6.19%	204.9	-21.76%

tabela 7.2

Distribuição de Temperaturas Pontuais - sem Galeria

	Atual	Liu - v1	erro (%)	Liu - v2	erro (%)	Stevens - v1	erro (%)	Stevens - v2	erro (%)	Hricak	erro (%)
Borda de Câmara	326.7	313.7	-4%	316.1	-3.24%	308.0	-5.72%	311.2	-4.74%	306.8	-6.09%
Centro da Câmara	335.9	315.2	-6.16%	321.8	-4.20%	292.5	-12.92%	301.5	-10.24%	267.4	-20.39%
1a Canaleta	275.5	261.9	-4.94%	264.3	-4.07%	255.8	-7.15%	259.2	-5.92%	254.6	-7.59%
Topo da Galeria	267.8	247.4	-7.62%	251.1	-6.24%	238.3	-11.02%	243.3	-9.15%	236.4	-11.73%
Fundo da Galeria	208.9	160.3	-23.26%	165.1	-20.97%	149.4	-28.48%	158.5	-24.13%	149.0	-28.67%
Centro do Undercrown	298.2	279.6	-6.24%	286.4	-3.96%	252.4	-15.36%	264.7	-11.23%	216.8	-27.30%

tabela 7.3

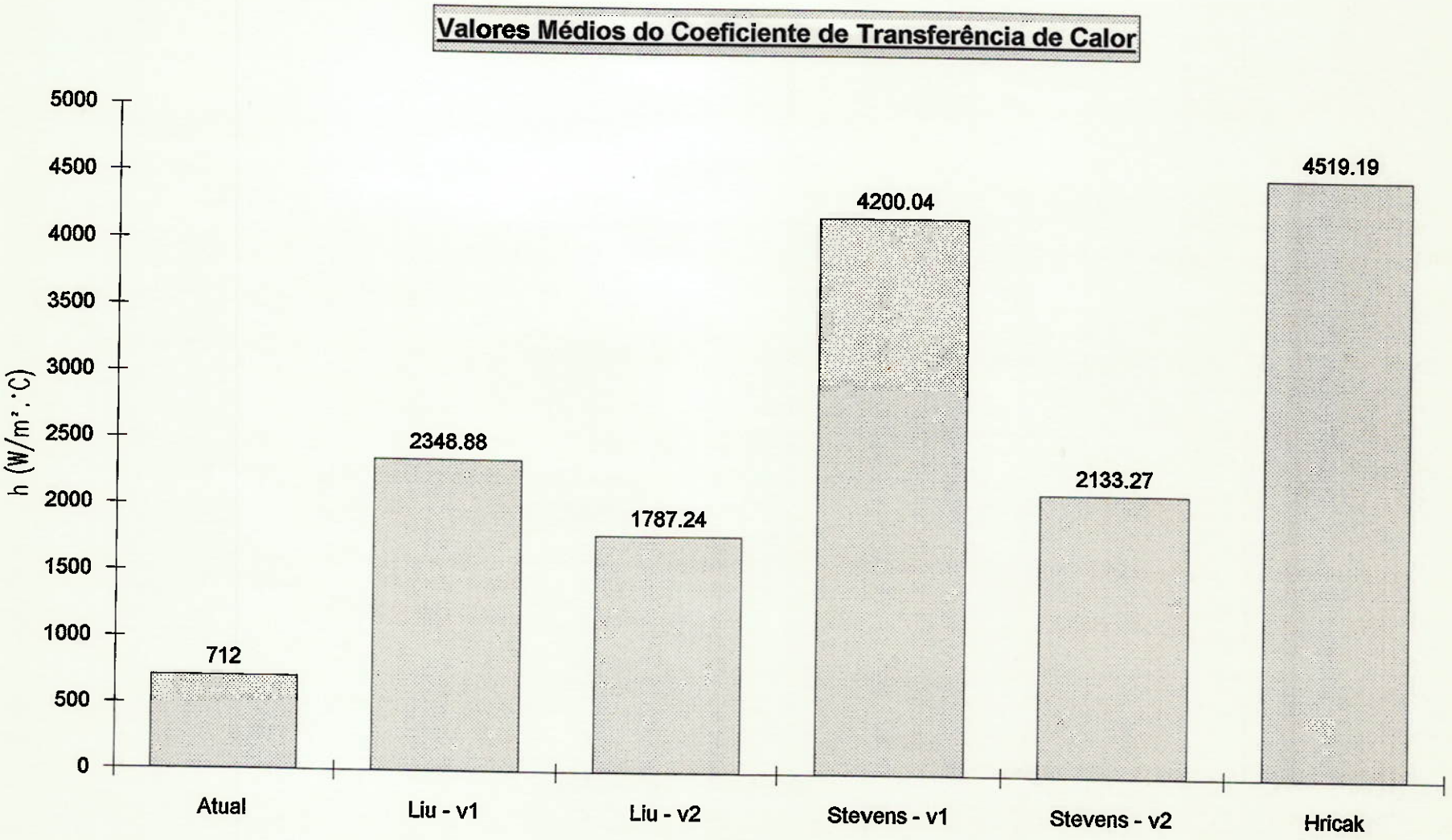
Valores Médios do Coeficiente de Transferência de Calor
h (W/m².°C)
5000
4500
4000
3500
3000
2500
2000
1500
1000
500
0
712
2348.88
1787.24
4200.04
2133.27
4519.19
Atual
Liu - v1
Liu - v2
Stevens - v1
Stevens - v2
Hricak

gráfico 7.1

7.2. Variação do Posicionamento de Impacto

A partir da definição de um modelo, o ponto de impacto do jato no undercrown (44,53mm em relação ao centro do pistão) foi deslocado em intervalos de 10 mm para o lado do centro do pistão a fim de se avaliar a influência do mesmo no perfil de temperaturas no pistão para as duas geometrias gerando novos perfis (figuras 7.13 a 7.20) e temperaturas nodais (tabelas 7.4 e 7.5 e gráficos 7.2 e 7.3).

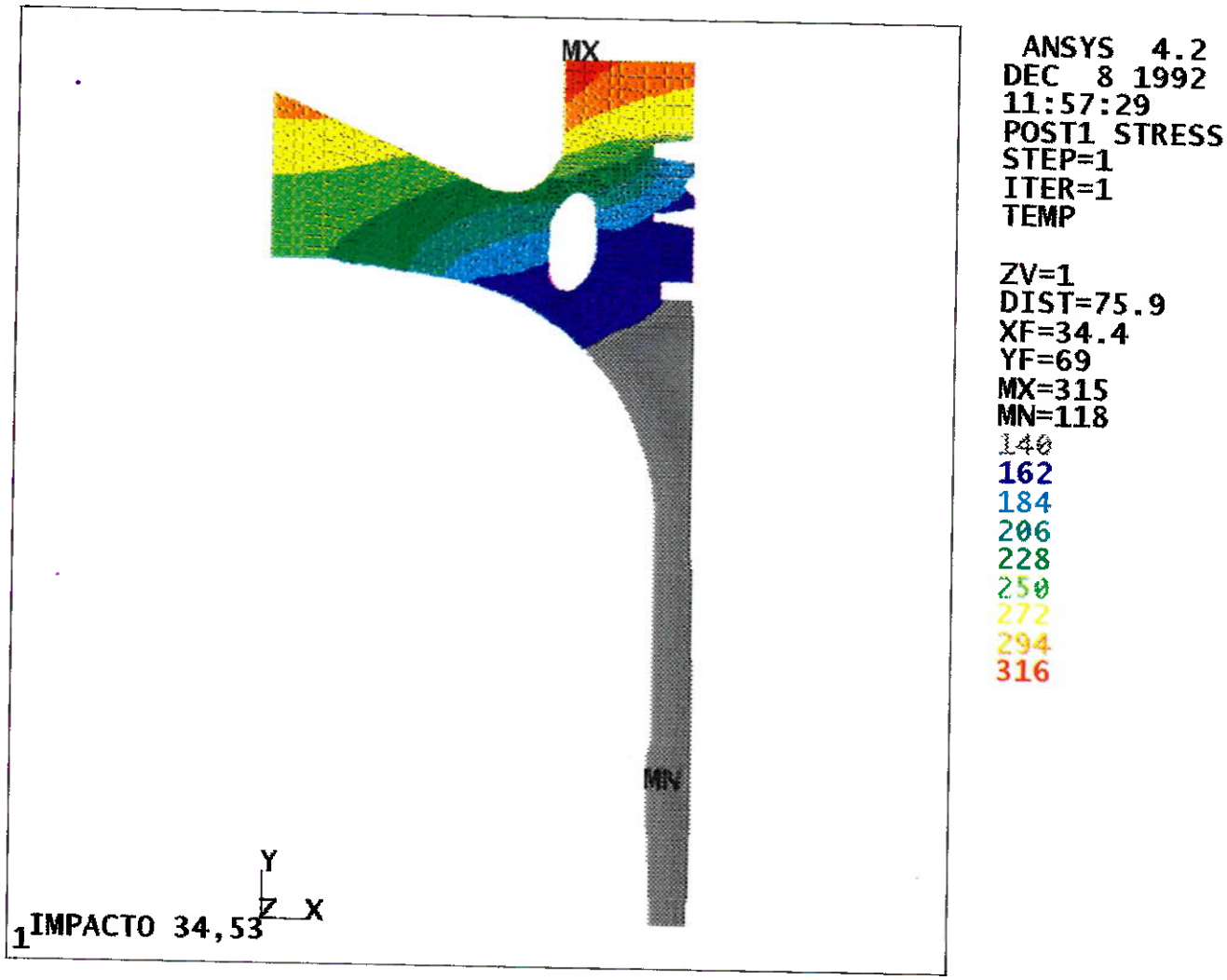
MX
MN
Y
Z
X
1 IMPACTO 34,53
ANSYS 4.2
DEC 8 1992
11:57:29
POST1 STRESS
STEP=1
ITER=1
TEMP
ZV=1
DIST=75.9
XF=34.4
YF=69
MX=315
MN=118
140
162
184
206
228
250
272
294
316

figura 7.13

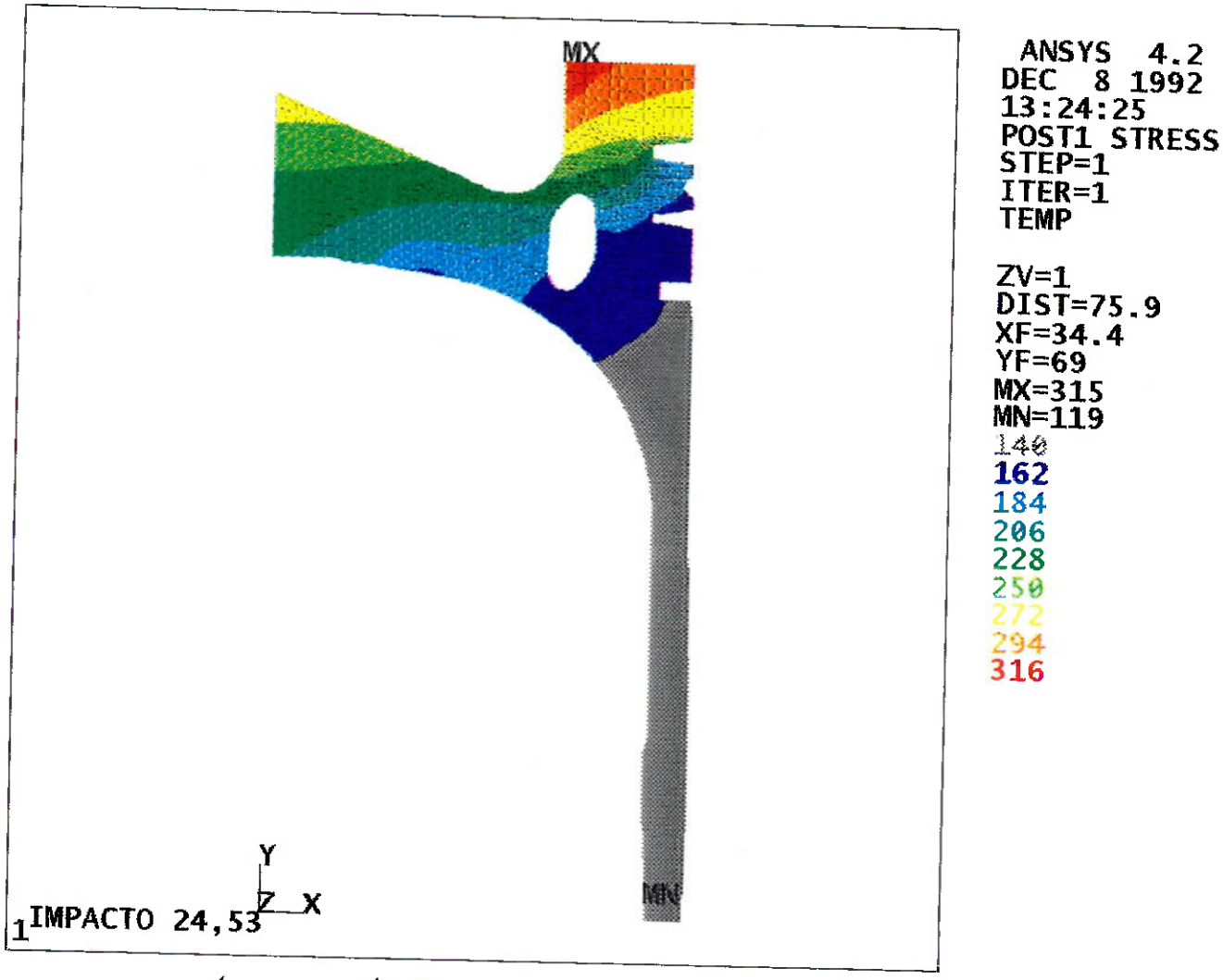
MX
MN
Y
Z
X
1
IMPACTO 24,53
ANSYS 4.2
DEC 8 1992
13:24:25
POST1 STRESS
STEP=1
ITER=1
TEMP
ZV=1
DIST=75.9
XF=34.4
YF=69
MX=315
MN=119
140
162
184
206
228
250
272
294
316

figura 7.14

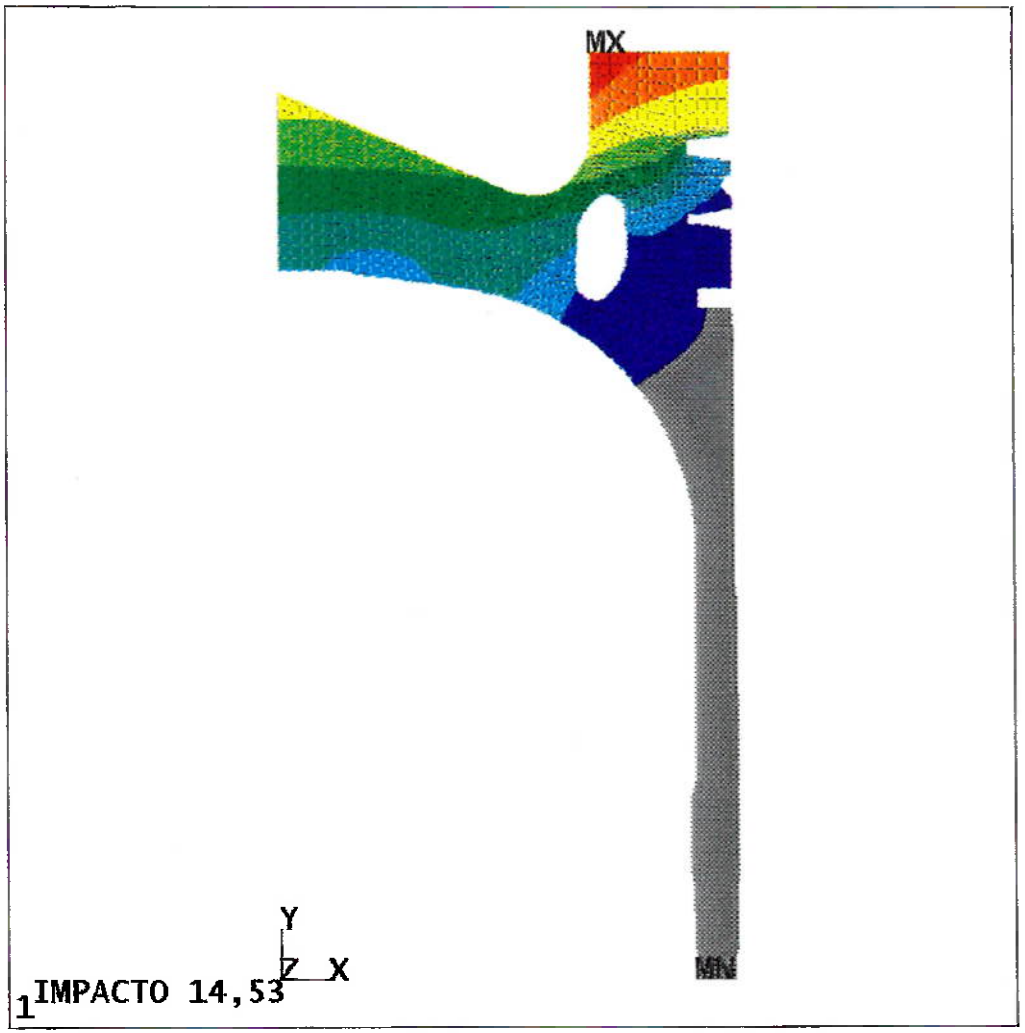

ANSYS 4.2
DEC 8 1992
13:32:12
POST1 STRESS
STEP=1
ITER=1
TEMP

ZV=1
DIST=75.9
XF=34.4
YF=69
MX=317
MN=120
141
163
185
207
229
251
273
295
317

figura 7.15

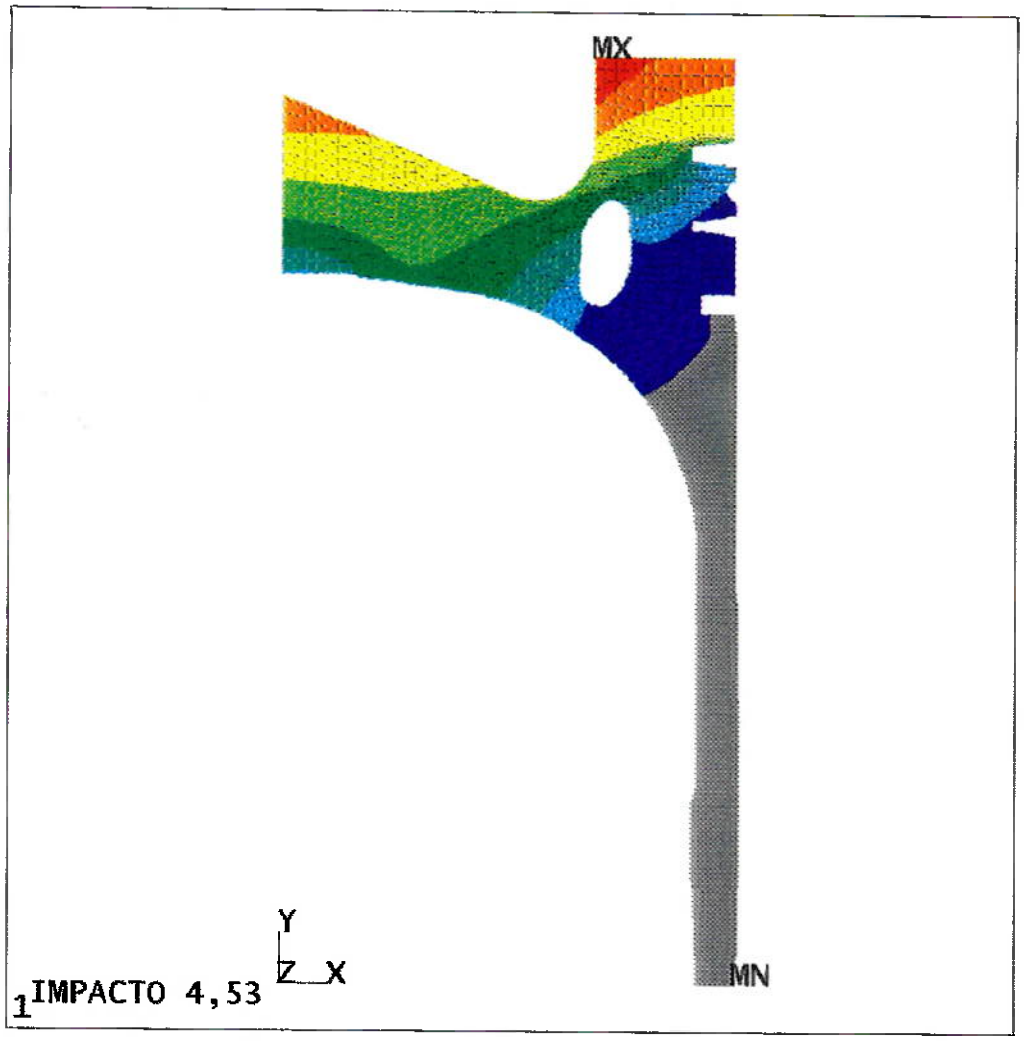

ANSYS 4.2
DEC 8 1992
13:37:32
POST1 STRESS
STEP=1
ITER=1
TEMP

ZV=1
DIST=75.9
XF=34.4
YF=69
MX=319
MN=122
143
165
187
209
231
253
275
297
319

figura 7.16

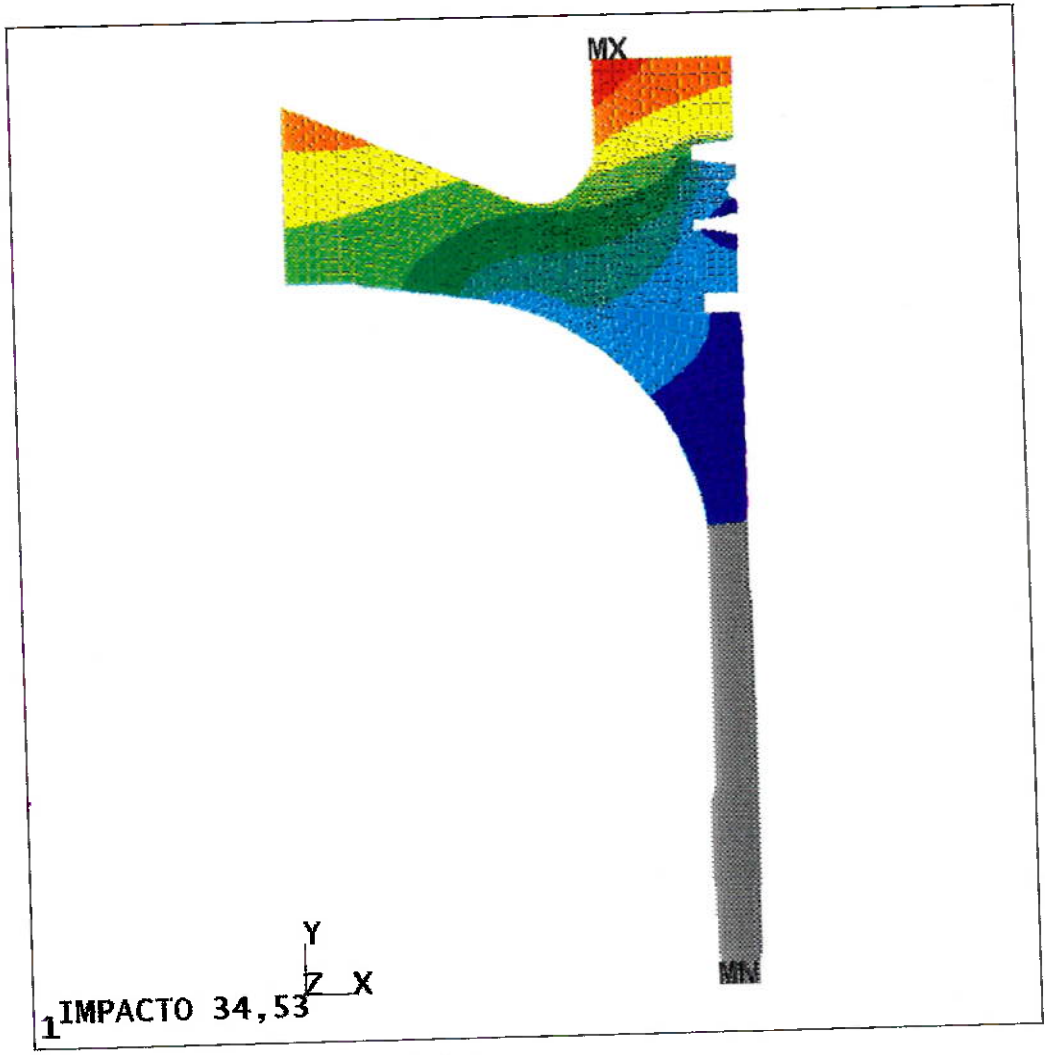
MX
MN
Y
Z
X
1
IMPACTO 34,53
ANSYS 4.2
DEC 8 1992
13:43:01
POST1 STRESS
STEP=1
ITER=1
TEMP
ZV=1
DIST=75.9
XF=34.4
YF=69
MX=333
MN=121
143
167
191
215
239
263
287
311
335

figura 7.17

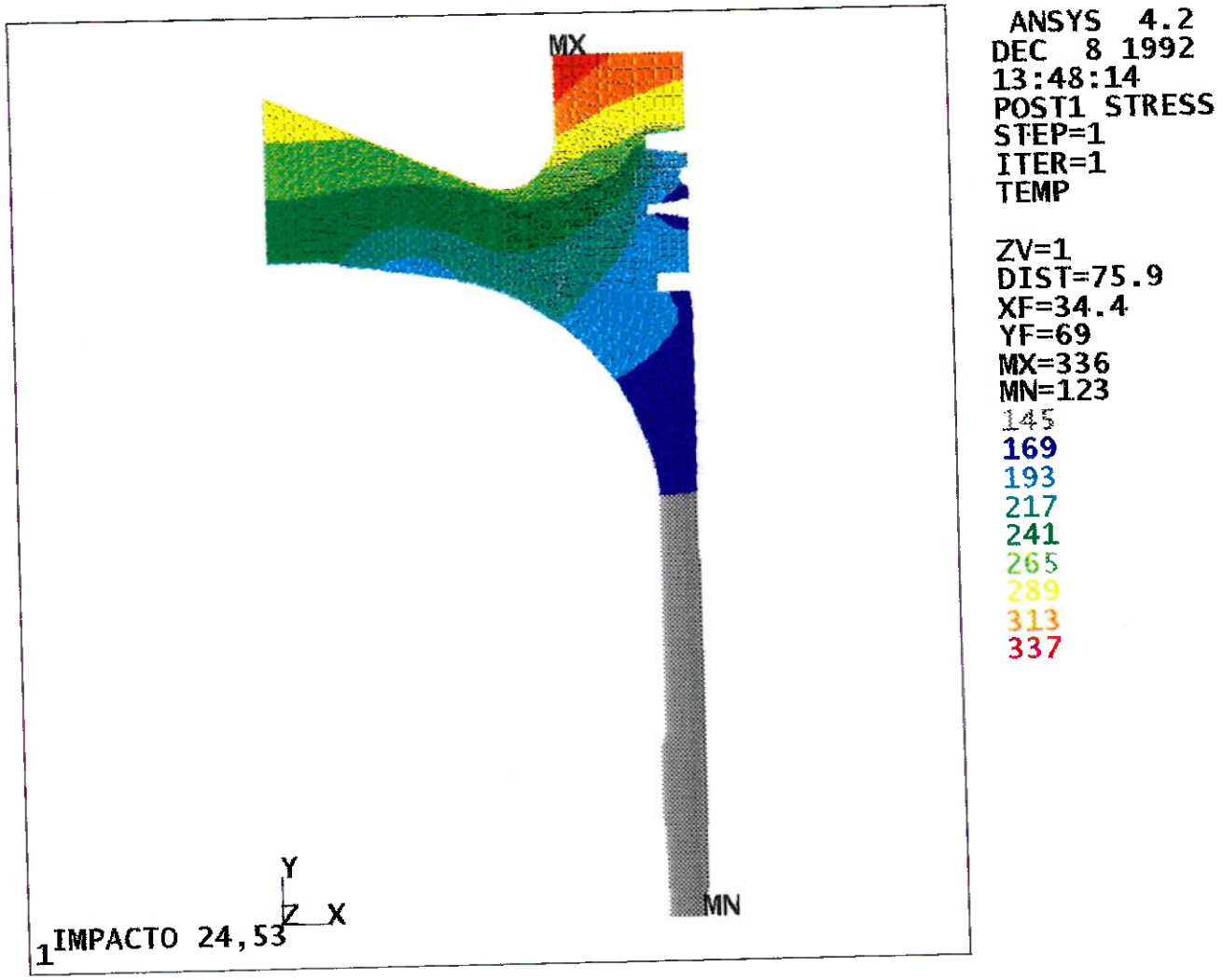
MX
MN
Y
Z
X
1
IMPACTO 24,53
ANSYS 4.2
DEC 8 1992
13:48:14
POST1 STRESS
STEP=1
ITER=1
TEMP
ZV=1
DIST=75.9
XF=34.4
YF=69
MX=336
MN=123
145
169
193
217
241
265
289
313
337

figura 7.18

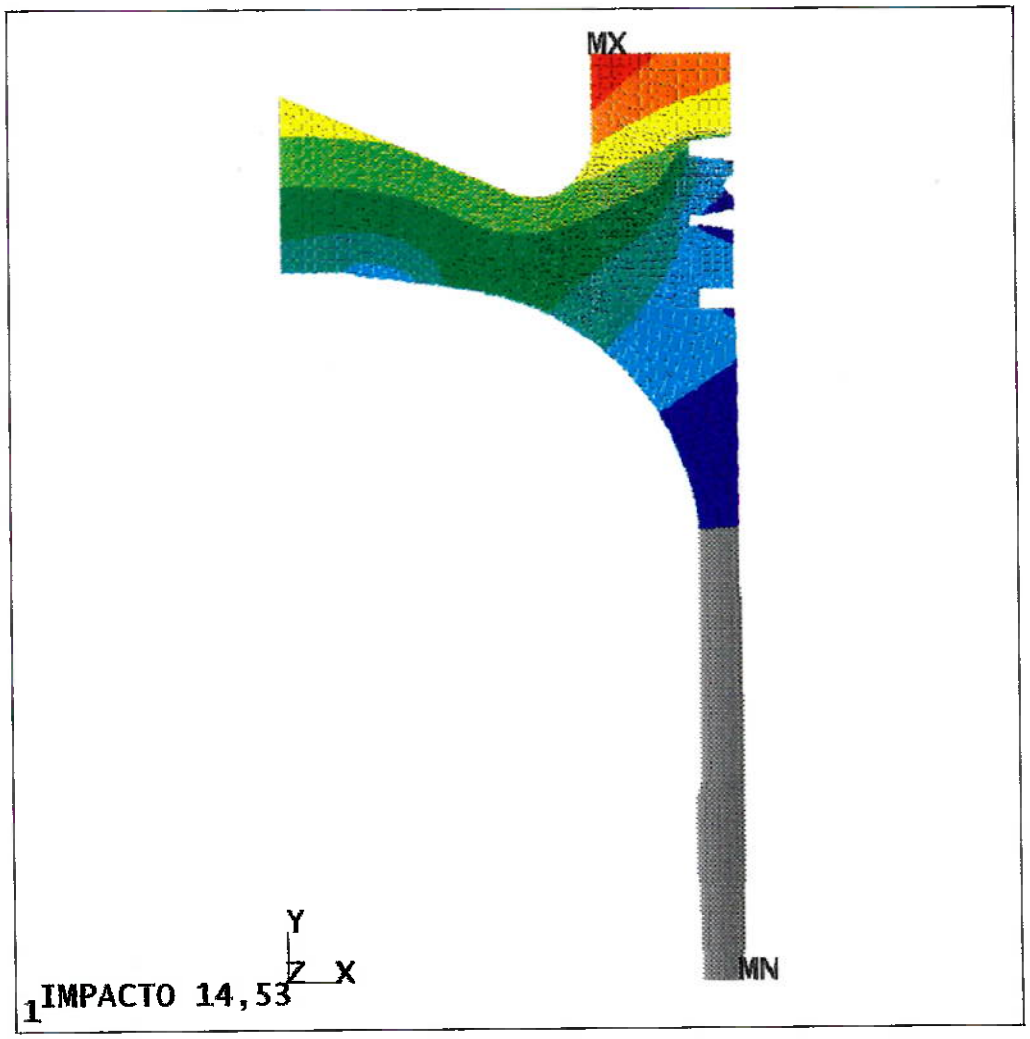

ANSYS 4.2
DEC 8 1992
14:02:29
POST1 STRESS
STEP=1
ITER=1
TEMP

ZV=1
DIST=75.9
XF=34.4
YF=69
MX=340
MN=124
148
172
196
220
244
268
292
316
340

figura 7.19

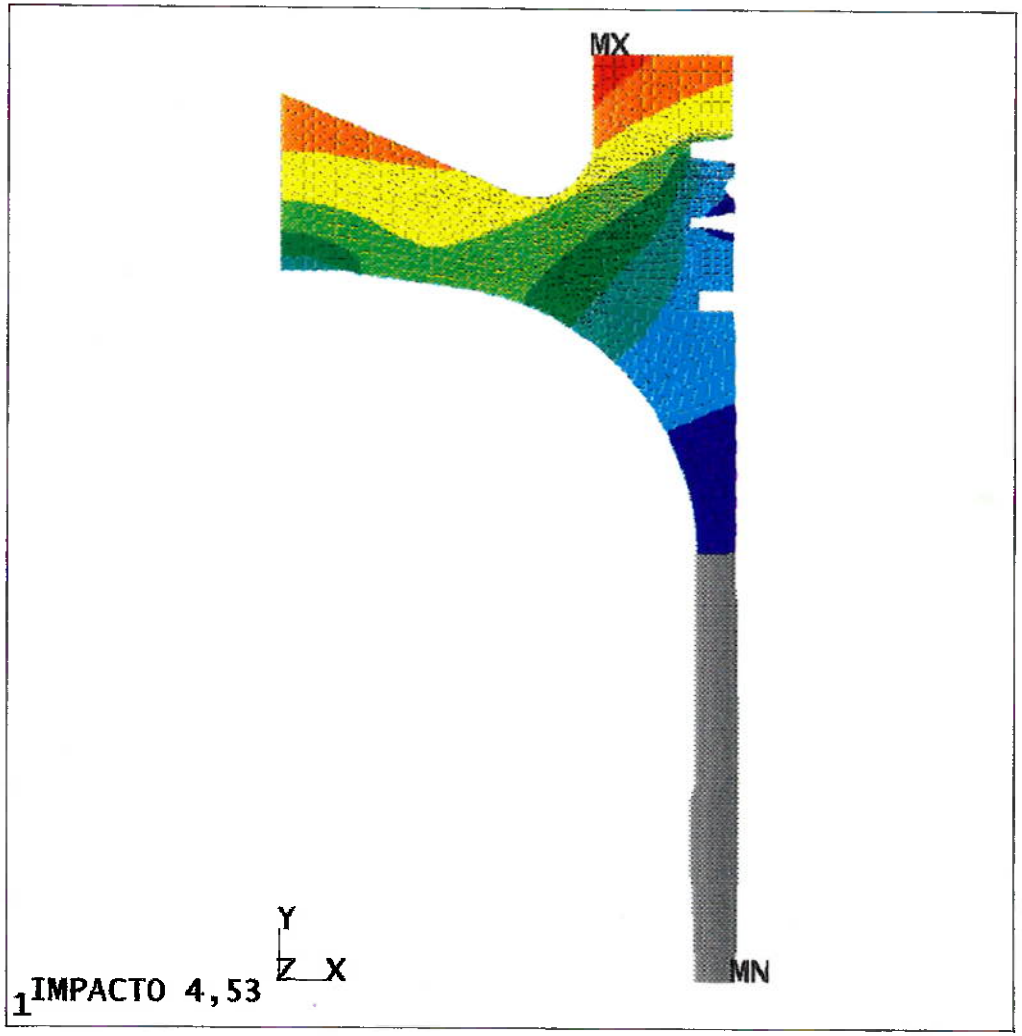

ANSYS 4.2
DEC 8 1992
14:10:47
POST1 STRESS
STEP=1
ITER=1
TEMP

ZV=1
DIST=75.9
XF=34.4
YF=69
MX=345
MN=126
148
173
198
223
248
273
298
323
348

figura 7.20

Distribuição de Temperaturas Pontuais
Variação de Posicionamento de Impacto

Modelo Liu - V2	44,53	34,53	24,53	14,53	4,53
Borda de Câmara	316.1	295.8	296.2	297.7	300.1
Centro da Câmara	321.8	271.7	251.5	249.7	278.7
1a Canaleta	264.3	242.6	243.1	244.6	246.9
Topo da Galeria	251.1	220.6	221.3	223.8	227.7
Fundo da Galeria	165.1	142.5	146.9	150.6	155.6
Centro do Undercrown	286.4	233.6	209.5	197.2	210.3

tabela 7.4

Distribuição de Temperaturas Pontuais sem Galeria
Variação de Posicionamento de Impacto

Modelo Liu - V2	44,53	34,53	24,53	14,53	4,53
Borda de Câmara	316.1	314.3	317.6	321.8	327.3
Centro da Câmara	321.8	293.4	272.4	272.9	311.1
1a Canaleta	264.3	262.6	266.1	270.4	276.3
Topo da Galeria	251.1	248.0	253.2	259.9	268.9
Fundo da Galeria	165.1	184.5	194.8	203.1	222.9
Centro do Undercrown	286.4	256.2	230.4	218.1	236.6

tabela 7.5

Variação da Distribuição de Temperatura com posição de Impacto
Pistão com Galeria

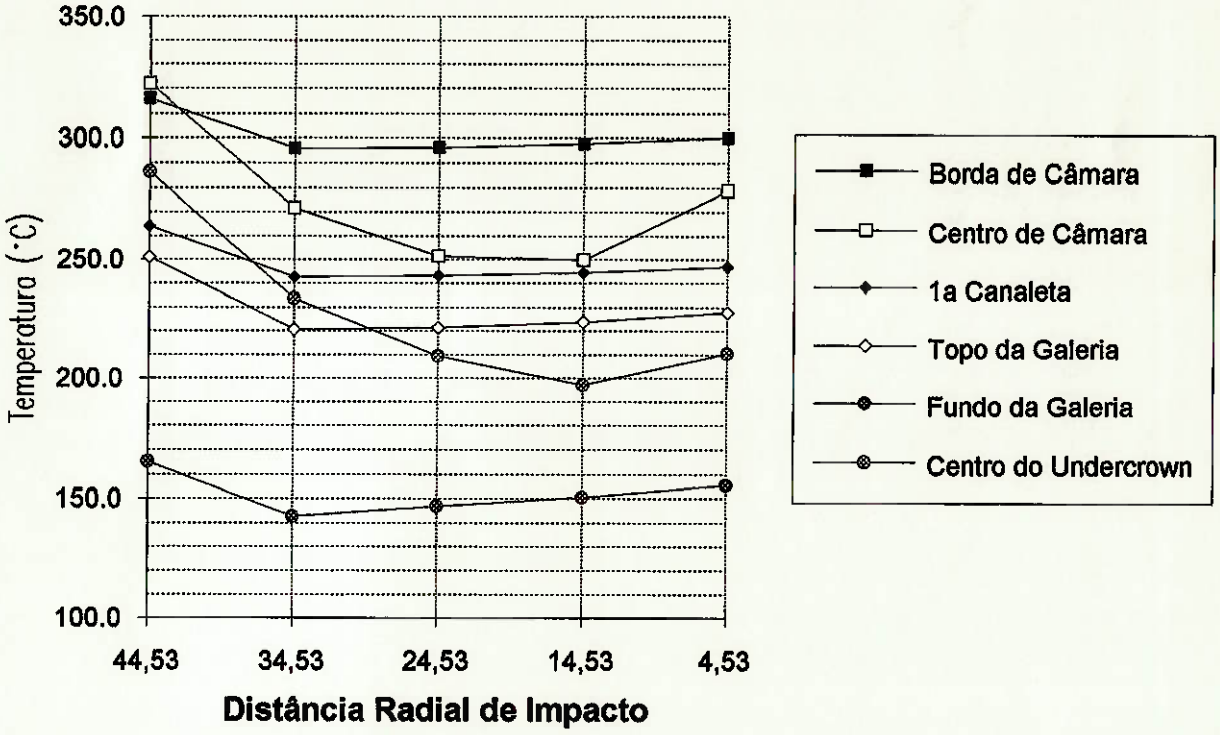

gráfico 7.2

Variação da Distribuição de Temperatura com posição de Impacto
Pistão sem Galeria

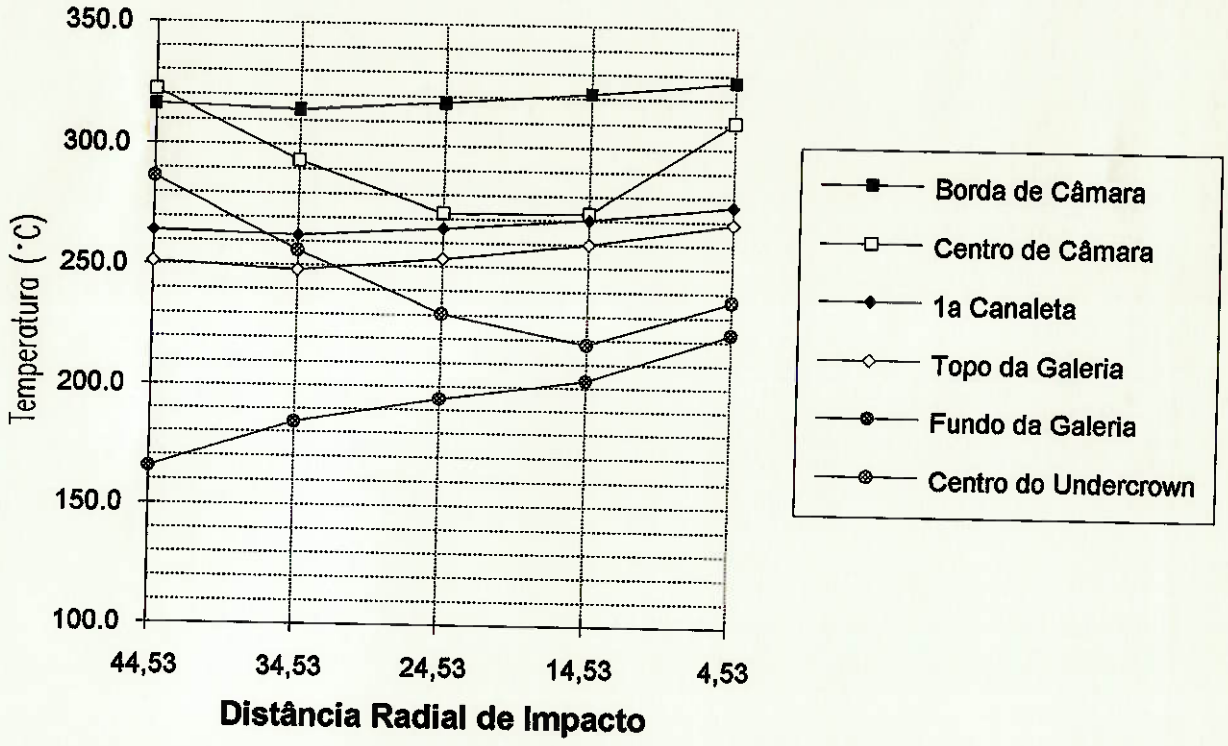

gráfico 7.3

8. ANÁLISE

8.1. Modelagem de Jatos de Refrigeração

Após a execução do modelo atual e dos 5 modelos propostos para ambas as geometrias (pistão com e sem galeria), pode-se analisar a validade dos mesmos a partir dos perfis de temperatura interna obtidos (figuras 7.1 a 7.12) e das tabelas com as temperaturas pontuais (tabelas 7.1 a 7.3) e valores médios de coeficiente de transferência de calor (gráfico 7.1).

O modelo proposto por Hricak (figuras 7.6 e 7.12), além de apresentar altos valores de erro, tem o maior valor do coeficiente de transferência de calor médio (gráfico 7.1).

Pode-se verificar que as diferenças entre os erros as versões 1 e 2 dos modelos de Liu e Stevens não são distantes, mostrando que esta variação de modelagem não influencia muito no resultado final.

Em relação ao modelo atual, as regiões mais críticas de comparação destes dois modelos (Liu e Stevens) são as proximidades da galeria de refrigeração. Fora destas regiões, os resultados são da ordem de menos de 10% no pistão com galeria. No pistão sem galeria, a sensibilidade do perfil em relação à distribuição de **h** no undercrown aumenta e também os erros relativos.

Em relação aos valores medidos há um acréscimo nas diferenças dos valores no centro da câmara e no undercrown.

Apesar de o modelo Liu versão 2 (figuras 7.5 e 7.11) apresentar os maiores valores de erro percentual na comparação com os valores medidos para o pistão com galeria, pode-se verificar que este modelo apresenta os menores erros na comparação com o modelo atual que vem sendo utilizado no desenvolvimento de novos projetos de pistões, com resultados satisfatórios.

8.2 Variação do Posicionamento de Impacto

A partir do modelo Liu (versão 2) original, a posição de impacto foi deslocada em intervalos constantes de 10mm em direção ao centro do pistão. Os resultados (tabelas 7.4 e 7.5, gráficos 7.2 e 7.3 e figuras 7.13 a 7.20) devem ser comparados aos perfis obtidos com impacto original (44,53mm em relação ao centro do pistão, figuras 8.5 e 8.11).

As tabelas 7.4 e 7.5 juntamente com os gráficos 7.2 e 7.3 mostram que há sensível diminuição de temperatura no centro da câmara e fundo do undercrown para o pistão sem galeria. Este efeito se repete para o pistão com galeria mas acompanhado de diminuição em todos os pontos quando impactamos em 34,53mm.

9. CONCLUSÃO

Neste trabalho, um modelo de distribuição de coeficiente de transferência de calor por convecção (h) para a parte inferior do pistão (undercrown) foi obtido a partir de um conjunto de modelos oriundos de uma pesquisa bibliográfica.

Para verificação destes modelos, estes foram aplicados em simulação numérica (Método dos Elelentos Finitos) e seus resultados comparados com valores de temperaturas pontuais medidos além do perfil do modelo utilizado atualmente.

O modelo (Liu - versão 2) foi escolhido em função da análise do perfil de distribuição interna de temperatura e comparação de temperaturas pontuais (nodais) em alguns pontos estratégicos do pistão com valores medidos experimentalmente e pirncipalmente com o perfil gerado pelo modelo atual, cujas isotermas tem se mostrado compatíveis com os resultados obtidos durante o desenvolvimento de pistões. A partir do modelo escolhido, variou-se a posição de impacto do jato para que a influência deste parâmetro pudesse ser avaliada, mostrando que existem pontos ótimos de impacto para a refrigeração de determinados pontos do pistão.

Algumas sugestões para a continuidade deste trabalho :

- Inclusão da dinâmica do pistão (movimento alternativo da superfície de impacto) nos modelos dos jatos, com distribuição 3-D;
- Refinamento da aplicação do modelo na simulação numérica (aumento nas faixas de aplicação dos modelos);
- Otimização do projeto do pistão, com base na análise da variação do posicionamento de impacto do jato.

APÊNDICES

APÊNDICE I

REFERÊNCIAS BIBLIOGRÁFICAS

REFERÊNCIAS BIBLIOGRÁFICAS

[1] Downs, S. J., James, E. H., 1987, "Jet Impingement Heat Transfer - A Literature Survey".

[2] Woschni, G., and Fieger, J., 1979, "Determination of Local Heat Transfer Coefficients at the Piston of a High Speed Diesel Engine by Evaluation of Measured Temperature Distribution".

[3] Woschni, G., "A Universally Applicable Equation for the Instantaneous Heat Transfer Coefficient in the Internal Combustion Engine".

[4] Stotter, A., "Heat Transfer in Piston Cooling".

[5] Martin, H., "Heat and Mass Transfer between Impinging Gas Jets and Solid Surfaces".

[6] Stevens, J., Webb, B. W., "Measurements of the Free Surface Flow Structure Under a Impinging, Free Liquid Jet".

[7] Torii, K., and Yanagihara, J. I., 1989, "The Effects of Longitudinal Vortices on Heat Transfer of Laminar Boundary Layers".

[8] Torii, K., Yanagihara, J. I., Nagai, Y., 1991, "Heat Transfer Enhancement by Vortex Generators".

[9] Yanagihara, J. I.,and Torii, K., 1990, "Heat Transfer Characteristics of Laminary Boundary In The Presence of Vortex Generators".

[10] Ward, J., Mahmood, M., "Heat Transfer from a Turbulent, Swirling, Impinging Jet".

[11] Chupp, R. E., Helms, H. E., McFadden, P. W., and Brown, T. R., 1968, "Evaluation of Internal Heat Transfer Coefficients for Impingement Cooled Turbines Aerofoils".

[12] Amano R. S., and Brandt H., 1985, "Numerical Study of turbulent axisymmetric jets impinging on a flat plate and flowing into an axisymmetric cavity".

[13] Gardon R., and Conboque J., 1961, "Heat Tansfer Between a Flat Plate and Jets of Air Impinging on it"

[14] Goldstein, R. J., and Timmers, J. F., 1982, "Visualization of Heat Transfer from Arrays of Impinging Jets"

[15] Hrycak, P., 1981, "Heat Transfer from a row of Impinging Jets to Concave Cylindrical Surfaces"

[16] Beltaos, S., 1976, "Oblique Impinging of Circular Turbulent Jets".

[17] Amano, R. S., and Sugiyama, S., 1985, "An Investigation on Turbulent Heat Transfer of an Axisymmetric Jet Impinging on a Flat Plate".

[18] Daane, R. A., and Han, S. T., 1961, "An Analysis of Air Impinging Drying ".

[19] Huang, G. C., 1963, "Investigation of Heat Transfer Coefficients for Air Flow Through Round Jets Impinging Normal to a Heat Transfer Surface".

[20] Fant, D., 1992, "Total Temperature Separation Enhances Turbine Cooling".

[21] Donaldson, C. D., Snedeker , R. S., and Margolis, D. P., 1971, "A Study of Free Jet Turbulent Structure and Impingement Heat Transfer".

[22] Wang, X. S., Dagon, Z., and Jiji, L. M., 1989, "Conjugate Heat Transfer between a Laminar Impinging Liquid Jet and a Solid Disk".

[23] Gardon, R., and Akfirat, J. C., 1965, "The Role of Turbulence in Determining the Heat Transfer Characteristics of Impinging Jets".

[24] Sparrow, E. M., Goldstein, R. J., and Rouf, M. A., 1975, "Effect of Nozzle-Surface Separation Distance on Impinging Heat Transfer for a Jet in a Crossflow".

[25] Sparrow, E. M., and Lovell, B. J., 1980, "Heat Transfer Characteristics of an Obliquely Impinging circular Jet".

[26] Liu, X., Lienhard V, J. H., Lombara, J. S., 1991, "Convective Heat Transfer by Impingement of Circular Liquid Jets".

[27] Stevens, J., Webb, B. W., 1989, "Local Heat Transfer Coefficients Under an Axisymmetric, Single-Phase Liquid Jet".

[28] Hrycak, P., 1982, "Heat Transfer and Flow Rate Characteristics of Jet Impinging on Concave Hemispherical Plate".

APÊNDICE II

BIBLIOGRAFIA

BIBLIOGRAFIA

1. Oswaldo Urbani Filho e Ednilson de A. Cavaco, "Manual de Orientação Básica para Usuários de ANSYS", fev. 1987.

2. Gabriel J. Desalvo, Ph.D e J. A. Swanson, Ph.D; "Engineering Analisys System User's Manual", Rev. 4.2, vol. I,II,III; Jun. 1985.

3. Holman, J. P., "Transferência de Calor", McGraw - Hill, 1983.

APÊNDICE III

ARTIGOS DOS MODELOS ESCOLHIDOS

Convective Heat Transfer by Impingement of Circular Liquid Jets

X. Liu
Student Mem. ASME

J. H. Lienhard V
Mem. ASME

J. S. Lombara[1]

Department of Mechanical Engineering,
Massachusetts Institute of Technology,
Cambridge, MA 02139

The impingement of circular, liquid jets provides a convenient method of cooling surfaces. Here, jet impingement cooling of uniformly heated surfaces is investigated analytically and experimentally for stable, unsubmerged, uniform velocity laminar jets in the absence of phase change. Analytical and numerical predictions are developed for a laminar radial film flow. Experiments using undisturbed laminar jets were performed to determine local Nusselt numbers from the stagnation point to radii of up to 40 diameters. Turbulent transition in the film flow is observed experimentally at a certain radius. Beyond this transition radius, a separate turbulent analysis is constructed. Integral method results are compared to numerical results, and Prandtl number effects are investigated. The predictions are found to agree well with the measurements for both laminar and turbulent flow. Predictive formulae are recommended for the entire range of radii.

Introduction

Cooling a surface with an impinging liquid jet is an attractive technique because of its high efficiency and unsophisticated hardware requirements. Applications of jet impingement cooling are varied, and include processing of both metals and molded plastics, cooling of high-efficiency (aircraft) generator coils, and cooling of certain electronic modules. Such jets lend themselves to either convective boiling or to nonevaporative convection, but in both situations the cooling efficiency varies with the radial distance from the point of impact. In this study, we consider the impingement of a circular, unsubmerged, laminar liquid jet on a surface of uniform heat flux. Convective transport, without change of phase, is analyzed theoretically and experimentally, taking account of both the initial laminar flow and the downstream turbulent flow.

An axisymmetric, laminar impinging jet spreads into a thin, laminar liquid film when it impacts a plane surface normal to its axis (Fig. 1). The hydrodynamics of this film have previously been studied theoretically by Watson (1964) and experimentally by Azuma and Hoshino (1984a, 1984b, 1984c, 1984d) and by Olsson and Turkdogan (1966). Watson divided the flow radially into a stagnation region, a boundary layer region with surface velocity equal to jet speed, and a region of viscous similarity with decreasing surface velocity; he noted that the film flow would be terminated by a hydraulic jump at a location independently controlled by downstream conditions. The thickness of the film initially decreases and then increases with radius as viscous wall effects slow the spreading film. Watson employed both viscous similarity and momentum integral solutions.

Watson's theoretical expressions for the laminar boundary layer and similarity region velocity profiles and film thickness were experimentally verified by Azuma and Hoshino (1984b, 1984c) using laser-Doppler measurements. This is in contrast to the results of Olsson and Turkdogan (1966), who measured the surface velocity by dropping bits of cork onto the liquid. Olsson and Turkdogan found poor agreement with Watson's predictions, observing a constant surface velocity lower than the jet speed, and their results have sometimes been used to deny the presence of a similarity region. However, no conclusive evidence showed that the dropped, buoyant cork actually moved at the liquid surface speed. Since the experimental approach of Azuma and Hoshino is clearly more accurate, we are inclined to give their conclusions greater weight. For the details of Watson's flow field, the reader is referred to his paper. His expressions, and those of a later independent study by Sharan (1984), are quoted hereinafter when needed.

Azuma and Hoshino measured the turbulent transition radius in their system (which used an annular orifice mounted on the plate, rather than an actual impinging jet) and also measured the subsequent velocity profiles. The turbulent film was well characterized by standard boundary layer results, but it did appear to show relaminarization farther downstream as the film slowed and its stability increased.

Using Watson's similarity solution, Chaudhury (1964) analyzed the heat transfer from an isothermal wall in terms of a series solution for the similarity region and an integral solution for the boundary layer region; Carper (1989) has also presented a solution to that problem. Liu and Lienhard (1989) developed predictions of the Nusselt number for uniform heat flux using an integral method and presented limited comparisons to ex-

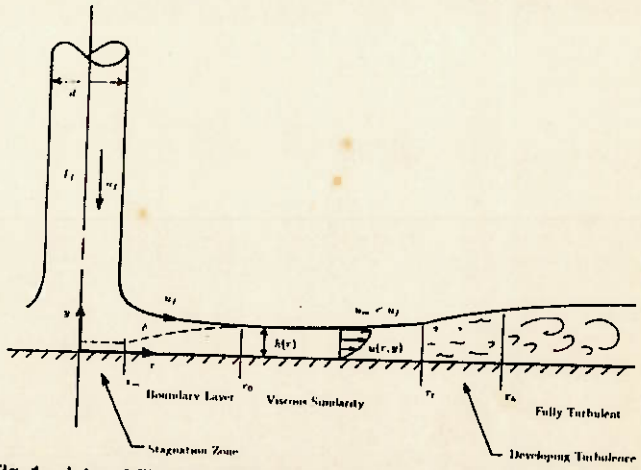

Fig. 1 Jet and film flow field showing hydrodynamic evolution (not to scale)

[1]Present address: Leutron Corporation, Allentown, PA.

Contributed by the Heat Transfer Division for publication in the JOURNAL OF HEAT TRANSFER. Manuscript received by the Heat Transfer Division July 4, 1990; revision received September 29, 1990. Keywords: Forced Convection, Jets, Thin Film Flow.

perimental data. Wang et al. (1989a, 1989b, 1989c) gave detailed theoretical solutions for heat transfer in the stagnation and boundary layer regions; these solutions account for variable wall conditions as well as for conjugate heat transfer between the jet and the wall. They did not consider the downstream similarity region, in which surface velocity declines with radius; at common Reynolds numbers, the stagnation zone and boundary layer regimes are confined to radii of 3 to 7 diameters from the point of impact. When a jet is used to cool large areas, the similarity region and turbulent transition must also be accounted for.

Experimental studies have been few, particularly in regard to local, rather than average, heat transfer. Ishigai et al. (1977) measured local heat transfer coefficients in the hydraulic jump region and presented a limited, graphic set of data for the local heat transfer coefficient in the plane of impact. They mentioned that the data showed a downstream transition from laminar to turbulent flow; their jets were produced by a short tube, three diameters in length. Stevens and Webb (1989) investigated turbulent impinging jet heat transfer experimentally and developed a correlation for Nu_d. Their data are confined to $r/d < 15$ and their correlation is accurate in a region $r/d < 5$ for $d = 2.2$ mm and a smaller region for larger diameter of jets. The radial transition from laminar to turbulent flow was not mentioned, but it must be noted that their jets were deliberately made turbulent prior to impact.

Nakoryakov et al. (1978) used electrodiffusion to obtain local mass transfer coefficients beneath a laminar jet and compared them to an appropriate boundary layer analysis. Their study applies to very high Schmidt number ($Sc \gg 1$) and a boundary condition of uniform wall concentration, correspondent to uniform wall temperature conditions at $Pr \gg 1$. Their experiments showed the mass transfer coefficient to rise above the laminar prediction downstream, and they argued this to result from surface waves. However, the present results suggest that transition to turbulence is a more likely cause in their range of Reynolds number. The incoming jet velocities for their experiments were calculated on the basis of the apparently theoretical stagnation zone result

$$Nu_l = 0.753\ Pr^{1/3}\ Re_l^{1/2} \qquad (1)$$

where l is the radius of their electrodiffusion probe. However, this correlation was not independently corroborated in their paper.

The present paper develops radially complete results for the liquid film heat transfer with uniform heat flux; most of these results are analytically derived, and all are validated experimentally. Particular attention is devoted to the similarity region, employing numerical solutions for the uniform flux condition (which is not self-similar) to investigate the role of wall boundary conditions, simplified correlations, and the integral method prediction of a critical Prandtl number above which the thermal boundary layer does not reach the free surface (Liu and Lienhard, 1989). Our previous integral method solutions are extended to include $Pr < 1$. The laminar predictions are then compared to new experimental data from an experimental apparatus configured to achieve very clean, stable, laminar jets. The laminar predictions are generally found to agree very well with the data. In addition, turbulent transition is observed in the similarity region, and separate analytical predictions are developed to account for the turbulent augmentation of the heat transfer. A correlation is given for the turbulent transition point.

Nomenclature

c_p = heat capacity
C_c = jet contraction coefficient = 0.611
C_f = friction factor
d = contracted jet diameter = $\sqrt{C_c} \times$ (diameter of orifice)
$f'(\eta)$ = similarity function, equation (24)
h = local thickness of liquid sheet
h_{r1} = liquid sheet thickness at the position where thermal boundary layer reaches the free surface
h_t = liquid sheet thickness at transition point from laminar to turbulence
h_{T0} = liquid sheet thickness at r_{T0}
k = thermal conductivity of the liquid
k_w = thermal conductivity of the heater
Nu_d = Nusselt number = $q_w d/k(T_w - T_f)$
Nu_r = Nusselt number based on r, = $q_w r/k(T_w - T_f)$ = $Nu_d(r/d)$
Pr = Prandtl number
q_w = wall heat flux
Q = volume flow rate of jet = $u_f \pi d^2/4$
r = radius measured from point of jet impact
r_h = hump radius, at which turbulence is fully developed
r_o = radius at which δ reaches the surface of the liquid sheet
r_1 = radius where thermal boundary layer reaches the free surface for $Pr > 1$
$r_{T,i}$ = location of the initial temperature profile given
r_{T0} = radius where thermal boundary layer reaches the free surface for $Pr < 1$
$r_{u,i}$ = location of the initial velocity profile given
r_t = radius at transition point from laminar to turbulent flow
R = Reynolds number defined by Watson = $2Q/d\nu$ = $(\pi/2)\ Re_d$
Re_d = Reynolds number of the jet = $u_f d/\nu$
St = Stanton number = $q_w/\rho c_p u_{max}\ (T_w - T_{sf})$
t = heater sheet thickness
$T(r, y)$ = liquid temperature distribution
T_f = jet temperature at impingement
T_m = measured temperature on the back of the heater
T_{sf} = free surface temperature
T_{sat} = liquid saturation temperature
T_w = wall temperature on the liquid side of the heater
$u(r, y)$ = radial velocity distribution in liquid film
u_f = velocity of impinging jet
u_{max} = local maximum film velocity (liquid free surface velocity), equal to u_f in regions 2, 2l, and 3l
y = distance normal to the wall
z = distance between nozzle and target plate
δ = viscous boundary layer thickness
δ_t = thermal boundary layer thickness
Δ = δ/h
Δ_{T0} = Δ at r_{T0}
ϵ = (t/d); ϵ^2 is the order of radial to vertical conduction in the heater sheet
η = similarity variable
θ = nondimensional temperature
μ = dynamic viscosity
ν = kinematic viscosity
ρ = density
ϕ = δ/δ_t

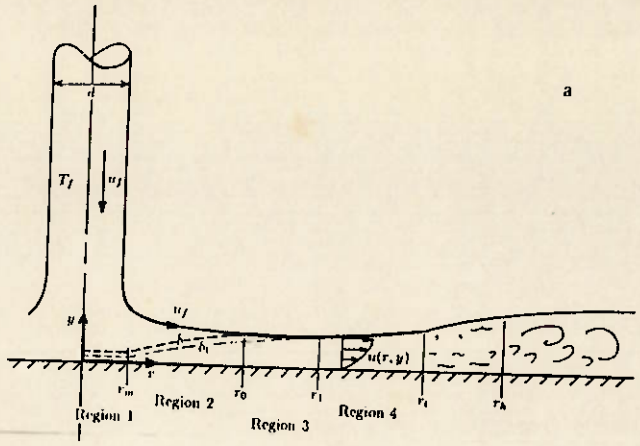

(a)

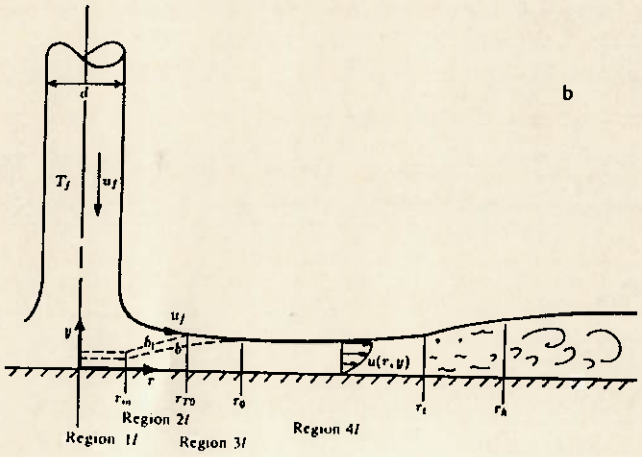

(b)

Fig. 2 Development of the thermal boundary layer: (*a*) Pr > 1; (*b*) Pr < 1 (not to scale)

2 Predictions From the Laminar Theory

2.1 Integral Solutions for the Heat Transfer: Pr ≥ 1. In a previous study (Liu and Lienhard, 1989), we obtained integral solutions for the heat transfer in the boundary layer and similarity regions for Prandtl number greater than the unity. The regions identified and results found are as follow (see Fig. 2*a*):

Region 1. The stagnation zone.

Region 2. $\delta < h$ region: Neither the thermal nor viscous boundary layer reach the free surface; surface temperature and velocity, T_{sf} and u_{max}, are the inlet temperature and velocity, T_f and u_f.

Region 3. $\delta = h$ and $\delta_t < h$ region: The viscous boundary layer has reached the free surface. The velocity outside the viscous boundary layer decreases with radius, but the surface temperature remains at the inlet temperature, T_f.

Region 4. $\delta = h$, $\delta_t = h$, and $T_w < T_{sat}$ region: In this region, the thermal boundary layer has reached the surface of the liquid sheet, and the temperature of the liquid surface increases with radius.

For region 2, the boundary layer region follows the stagnation zone:

$$\mathrm{Nu}_d = 0.632\ \mathrm{Re}_d^{1/2}\ \mathrm{Pr}^{1/3}\left(\frac{d}{r}\right)^{1/2} \tag{2}$$

Region 2 ends and region 3 begins where the viscous boundary layer reaches the film surface at $r = r_0 = 0.1773 d\,\mathrm{Re}_d^{1/3}$. In region 3:

$$\mathrm{Nu}_d = \frac{0.407\ \mathrm{Re}_d^{1/3}\ \mathrm{Pr}^{1/3}\left(\frac{d}{r}\right)^{2/3}}{\left[0.1713\left(\frac{d}{r}\right)^2 + \frac{5.147 r}{\mathrm{Re}_d d}\right]^{2/3}\left[\frac{1}{2}\left(\frac{r}{d}\right)^2 + C_3\right]^{1/3}} \tag{3}$$

where[2]

$$C_3 = \frac{0.267(d/r_0)^{1/2}}{\left[0.1713\left(\frac{d}{r_0}\right)^2 + \frac{5.147 r_0}{\mathrm{Re}_d d}\right]^2} - \frac{1}{2}\left(\frac{r_0}{d}\right)^2 \tag{4}$$

Region 3 ends and region 4 begins where the thermal boundary layer reaches the liquid surface at $r = r_1$; equations defining r_1 are given in our previous paper. In region 4:

$$\mathrm{Nu}_d = \frac{0.25}{\frac{1}{\mathrm{PrRe}_d}\left(1 - \frac{r_1^2}{r^2}\right)\left(\frac{r}{d}\right)^2 + 0.130\frac{h}{d} + 0.0371\frac{h_{r1}}{d}} \tag{5}$$

where h is given by equation (20) below. Note that region 4 will occur only for Pr less than a critical value near five[3]; otherwise, the thermal boundary layer does not grow fast enough to reach the surface of the liquid film, which thickens at increasing radius owing to viscous retardation. This Prandtl number prediction is of particular interest, and we shall explore it further using numerical solutions for the viscous flow regime below. Regions 3 and 4 correspond to Watson's self-similar viscous flow regime.

2.2 Integral Solutions for the Heat Transfer: Pr < 1. As noted in our previous paper, the region map changes for small Prandtl number (see Fig. 2*b*):

Region 1I. The stagnation zone.

Region 2I. $\delta_t < h$ region: Neither the thermal nor viscous boundary layer reaches the free surface; surface temperature and velocity, T_{sf} and u_{max}, are the inlet temperature and velocity, T_f and u_f.

Region 3I. $\delta_t = h$ and $\delta < h$ region: The thermal boundary layer has reached the free surface. The surface temperature increases with radius, but the velocity outside the viscous boundary layer is still the jet velocity, u_f.

Region 4I. $\delta = h$, $\delta_t = h$, and $T_w < R_{sat}$ region: In this region, the viscous boundary layer has reached the surface of the liquid sheet, and the velocity of the liquid surface decreases with radius.

The integral energy equation may be used to estimate the Nusselt number:

$$\frac{d}{dr}\int_0^{\delta_t} ru(T - T_f)\,dy = \frac{q_w}{pc_p} r \tag{6}$$

In region 2I, we approximate the velocity and temperature profiles as

$$T - T_w = (T_f - T_w)\left[\frac{3}{2}\frac{y}{\delta_t} - \frac{1}{2}\left(\frac{y}{\delta_t}\right)^3\right] \tag{7}$$

$$u = u_{\max}\left[\frac{3}{2}\frac{y}{\delta} - \frac{1}{2}\left(\frac{y}{\delta}\right)^3\right] \quad y < \delta$$
$$= u_f \quad y \geq \delta \tag{8}$$

These profiles satisfy no slip at the wall, have no shear or heat flux at the free surface (i.e., negligible evaporation; Liu and Lienhard, 1989), and match the local wall temperature. Integration of equation (6) with these profiles yields

[2] We have here corrected a minor typographical error in the expression for C_3 appearing in our previous paper.

[3] Our previous paper gave this value as 4.86. If the higher-order terms in the integral analysis are retained, the value becomes 5.23, which is 7 percent higher than the previous one.

$$\mathrm{Nu}_d=\left[\frac{\frac{9}{16}\mathrm{Re}_d\mathrm{Pr}\left(\frac{r}{d}\right)\left(1-\phi+\frac{2}{5}\phi^2-\frac{1}{35}\phi^4\right)}{\frac{1}{2}\left(\frac{r}{d}\right)^2+C}\right]^{1/2} \tag{9}$$

$$\phi=\frac{\delta}{\delta_t}=1.786\,\mathrm{Nu}_d\left(\frac{r}{d\,\mathrm{Re}_d}\right)^{1/2} \tag{10}$$

and C is a constant used to match to the stagnation zone. (The stagnation zone is discussed in Section 4.4 below.) If we assume that at the match point r_m, $\mathrm{Nu}_d = \mathrm{Nu}_{d,m}$ and $\phi = \phi_m$, then

$$C=\frac{9}{16}\frac{\mathrm{Re}_d\mathrm{Pr}}{\mathrm{Nu}_{d,m}^2}\left(\frac{r_m}{d}\right)\left(1-\phi_m+\frac{2}{5}\phi_m^2-\frac{1}{35}\phi^4\right)-\frac{1}{2}\left(\frac{r_m}{d}\right)^2 \tag{11}$$

If δ/δ_t is very small and C is also negligible (as shown in section 4), equation (11) can be further simplified to

$$\mathrm{Nu}_d=1.06\,\mathrm{Re}_d^{1/2}\mathrm{Pr}^{1/2}\left(\frac{d}{r}\right)^{1/2} \tag{12}$$

Region 2*l* ends where the thermal boundary layer reaches the surface of the liquid sheet at $r=r_{T0}$:

$$\frac{r_{T0}}{d}=\frac{0.1984\mathrm{Re}_d^{1/3}\mathrm{Pr}^{1/3}}{\left(1-0.7107\mathrm{Pr}^{1/2}\right)^{2/3}} \tag{13}$$

In region 3*l*, $\delta_t = h$ and the temperature of the liquid surface, T_{sf}, is an increasing function of r. The temperature profile in this region is

$$T-T_w=(T_{sf}-T_w)\left[\frac{3}{2}\frac{y}{h}-\frac{1}{2}\left(\frac{y}{h}\right)^3\right] \tag{14}$$

At r_{T0}, the beginning of region 3*l*, $\mathrm{Nu}_d = \mathrm{Nu}_{d,T0}$, $h = h_{T0}$, and $\delta = \delta_{T0}$, where h and δ can be computed from Sharan's equations (1984):

$$\frac{h}{d}=0.125\left(\frac{d}{r}\right)+1.005\left(\frac{r}{\mathrm{Re}_d d}\right)^{1/2} \tag{15}$$

$$\frac{\delta}{d}=2.679\left(\frac{r}{\mathrm{Re}_d d}\right)^{1/2} \tag{16}$$

Integration of equation (6) from $r = r_{T0}$ with equations (8) and (14) gives

$$\left(\frac{\mathrm{Nu}_d}{2(1-\frac{3}{8}\Delta)}\right)^{-1}=\frac{r}{\mathrm{Re}_d\mathrm{Pr}h}\left(1-\left(\frac{r_{T0}}{r}\right)^2\right)+\frac{4}{3}\frac{h}{d}\left(\frac{5}{8}-\frac{3}{20}\Delta^2+\frac{3}{280}\Delta^4\right)-\frac{4}{3}\frac{h_{T0}}{d}\left(\frac{5}{8}-\frac{3}{20}\Delta_{T0}^2+\frac{3}{280}\Delta_{T0}^4\right)+2\frac{r_{T0}h_{T0}}{rh}\left(1-\frac{3}{8}\Delta_{T0}\right)\frac{1}{\mathrm{Nu}_{T0}} \tag{17}$$

where $\Delta = \delta/h$. If the terms in Δ are neglected, this simplifies to

$$\mathrm{Nu}_d=\frac{2}{\frac{r}{\mathrm{Re}_d\mathrm{Pr}h}\left(1-\left(\frac{r_{T0}}{r}\right)^2\right)+0.833\frac{h}{d}-0.833\frac{h_{T0}}{d}+2\frac{r_{T0}h_{T0}}{rh}\frac{1}{\mathrm{Nu}_{T0}}} \tag{18}$$

Region 4*l* begins at $r_0 = 0.1773\,d\mathrm{Re}_d^{1/3}$, where the viscous boundary layer reaches the surface; here, the surface velocity decreases with radius. Sharan's integral analysis (1984) shows that

$$u_{\max}=\frac{1}{5}\frac{u_f d^2}{hr} \tag{19}$$

where

$$h=0.1713\left(\frac{d^2}{r}\right)+\frac{5.147}{\mathrm{Re}_d}\left(\frac{r^2}{d}\right) \tag{20}$$

(Equation (20) is in good agreement with Watson's expression for h, which is based on velocity profile of the similarity solution.) The velocity profile is equation (8) with $\delta = h$ and u_{max} from equation (19), while the temperature profile is still equation (14). At $r = r_0$, $h = h_0$ and $\mathrm{Nu}_d = \mathrm{Nu}_{d,0}$. Integration of equation (6) from $r = r_0$ yields

$$\mathrm{Nu}_d=\frac{0.25}{\frac{1}{\mathrm{Re}_d\mathrm{Pr}}\left(\frac{r^2}{d^2}-\frac{r_0^2}{d^2}\right)+0.130\left(\frac{h_0}{d}-\frac{h}{d}\right)+0.25\frac{1}{\mathrm{Nu}_{d,0}}} \tag{21}$$

2.3 Numerical Integration in the Viscous Similarity Region. In the region of viscous similarity, we may solve the nonsimilar boundary-layer energy equation numerically in order to evaluate the accuracy of the integral method solutions for regions 3 and 4 ($\mathrm{Pr}>1$) and for region 4*l* ($\mathrm{Pr}<1$). In addition, we may probe the predicted critical Prandtl number for the occurrence of region 4 and the general differences between regions 3 and 4.

Chaudhury (1964) used Watson's velocity similarity to transform the energy equation in the film into the following form:

$$\frac{\partial^2 T}{\partial\eta^2}=\mathrm{Pr}f'\frac{(r^3+l^3)}{r^2}\frac{\partial T}{\partial r} \tag{22}$$

Here, the velocity similarity profile is (Watson, 1964)

$$\frac{2}{c^2}f'(\eta)=\sqrt{3}+1-\frac{2\sqrt{3}}{1+cn\left[3^{1/4}c(1-\eta)\right]} \tag{23}$$

where cn is a Jacobi elliptic function, $c = 1.402$, the similarity coordinate is

$$\eta=\frac{y}{h}=\frac{3\sqrt{3}Qr}{2\pi^2\nu(r^3+l^3)}y \tag{24}$$

and the length l is

$$l=0.3243d\,\mathrm{Re}_d^{1/3} \tag{25}$$

We may nondimensionalize r and l in equation (22) with r_0, the radius at which the viscous boundary layer reaches the liquid surface ($0.1833d\,\mathrm{Re}_d^{1/3}$, according to Watson's analysis[4]). Temperature is nondimensionalized as

$$\theta=\frac{T-T_f}{\Delta T} \tag{26}$$

where ΔT is chosen for convenience as $\Delta T = (2\pi^2\nu q_w r_0^2)/(3\sqrt{3}kQ)$ for uniform wall heat flux and as $\Delta T = T_w - T_f$ for uniform wall temperature. The differential equation is then

$$\frac{\partial^2\theta}{\partial\eta^2}=\mathrm{Pr}f'(\eta)\frac{\bar{r}^3+\bar{l}^3}{\bar{r}^2}\frac{\partial\theta}{\partial\bar{r}} \tag{27}$$

The thermal boundary condition at the wall is

$$\left.\frac{\partial\theta}{\partial\eta}\right|_{\eta=0}=-\frac{\bar{r}^3+\bar{l}^3}{\bar{r}} \tag{28}$$

for uniform flux and

$$\theta|_{\eta=0}=1 \tag{29}$$

for uniform temperature. The free surface is assumed to experience negligible evaporation or convection, so that

[4]Watson found a Blasius velocity profile upstream of the similarity region. The integral method's algebraic velocity profile gives a constant of 0.1773, rather than 0.1833 (3.4 percent lower). To maintain consistency within each approach, we apply 0.1773 with our integral solutions and 0.1833 with the differential equation solutions.

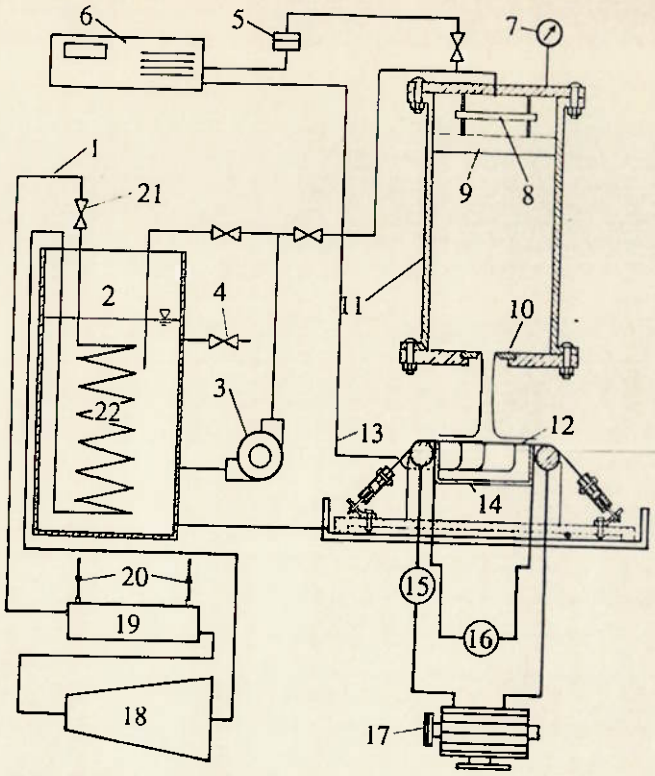

Fig. 3 Experimental apparatus: 1. Freon line; 2. chilled water tank; 3. pump; 4. water supply line; 5. pressure transducer; 6. digital voltmeter; 7. pressure gage; 8. momentum dissipating plate; 9. honeycomb; 10. sharp-edged orifice plate; 11. plenum; 12. steel heater sheet; 13. thermocouple leads; 14. pressurized plastic box; 15. ammeter; 16. voltmeter; 17. 30 kW generator; 18. compressor; 19. heat exchanger; 20. cooling water; 21. throttling valve; 22. evaporator

$$\left.\frac{\partial\theta}{\partial\eta}\right|_{\eta=1} = 0 \tag{30}$$

This approximation is valid for low liquid surface temperatures (Liu and Lienhard, 1989).

The numerical integration begins at $\bar{r} = 1$ ($r = r_0$). The temperature profile at this station is the initial condition for the solution; tests (see below) show that the initial profile is quickly damped and has little influence on the Nusselt number downstream. The following initial profile was employed:

$$\frac{T-T_f}{T_w-T_f} = 1-\frac{3_y}{2\delta_t}+\frac{1}{2}\left(\frac{y}{\delta_t}\right)^3 \quad y\le\delta_t \tag{31}$$

$$= 0 \qquad \delta_t\le y\le\delta \tag{32}$$

which again satisfies the boundary conditions (no surface flux and matching to T_w). The wall temperature and boundary layer thickness were selected to match those of the upstream boundary layer as calculated from the integral solution. The differential equation was integrated using the Crank-Nicholson procedure.

3 Experiments

Experiments were performed to determine the wall temperature distribution and Nusselt number that actually occur in jet impingement cooling. The experimental arrangement is shown in Fig. 3. The apparatus is in three primary parts: a water jet loop, a refrigerating system, and an electrical heating system.

In our previous paper, the experimental jets showed significant disturbances and sometimes splattered. To prevent splattering, a new apparatus was built specifically to produce uniform velocity-profile, laminar jets free of the surface disturbances that produce splattering (Vasista, 1989). A large plenum with an inlet momentum-breakup plate and turbulence dissipating honeycomb was used to create a pressurized liquid supply free of disturbances from the incoming flow. The jets studied were produced at the bottom of the plenum. The stability of liquid jets is very sensitive to the type of nozzle producing the jet. Pipelike nozzles provide turbulent liquid to the jet when the Reynolds number exceeds a relatively small value (2000–4000); this turbulence generally leads to disturbances in the liquid surface, which are unstable and which are strongly amplified when the jet impacts a flat surface (Errico, 1986). In the present experiments, carefully machined sharp-edged orifice plates were used, rather than pipelike nozzles. Sharp-edged orifices yield laminar, undisturbed jets of high stability. Thus, splattering was entirely suppressed in the present experiments.

The liquid supply was chilled by a mechanical refrigerator before being pumped to the plenum. The water was cooled to near 4°C. This cooling served two purposes. The first was to ensure that the liquid free-surface temperature would not become high enough to produce significant evaporative heat loss at any point along the heater surface (Liu and Lienhard, 1989). The second was to increase the accuracy of the experiments: The requirement of low evaporative loss necessitates relatively low heat fluxes and consequently small differences between wall and inlet temperatures. Subcooling the liquid supply maximized the measured ΔT, without creating evaporative loss, and thus decreased the uncertainty in the measured Nusselt number.

The liquid jets impinge on a heater made of 0.10-mm-thick, 15.2-cm-wide stainless steel sheet. The sheet is stretched over the open top of a 15.2 cm by 17.7 cm plexiglass insulation box and over 2.54-cm-dia. copper rods, which serve as electrodes; springs maintain the tension in the sheet as it expands thermally and prevent its vibration or deflection. The insulation box keeps water away from the underside of the heater sheet, and restricts underside heat losses to a negligible natural convection loss. The box is slightly pressurized with compressed air to prevent liquid inflow. A 15 V, 1200 amp generator powers the sheet directly; the generator was run at up to 20 percent of full power.

The wall temperature distribution is measured by 0.076 mm J-type thermocouples attached to the underside of the sheet and electrically insulated from it by high-temperature Kapton tape. Starting at the stagnation point of the jet, the thermocouples are placed at radial increments of 1.27 cm along the arcs of circle centered at the stagnation point, within a sector of very small angle. The azimuthal symmetry of the flow is very high, and the mechanical convenience of this arrangement was found to introduce no error.

Radial conduction in the heater sheet may be shown to be of order $\epsilon^2 = (t/l)^2$ relative to vertical conduction, where l is the length scale associated with radial changes in the heat transfer coefficient. For the jets, l is essentially the jet diameter, d, so that $\epsilon^2 \approx 0.001$. Radial conduction is thus negligible in comparison to vertical conduction; a formal perturbation solution of the heat equation substantiates this conclusion.

Convective backloss, via natural convection below the heater, is likewise negligible relative to the convective cooling at the upper surface of the heater; the back is essentially adiabatic. At the stagnation point, backloss is less than 0.2 percent of the total flux, owing to the very high liquid-side Nusselt number. The backloss increases downstream, as the Nusselt number declines, but even in the worst case, at the largest radius, this loss is less than 4 percent. Because the backloss is so small, the temperature drop through the 0.06 mm thick Kapton tape (which electrically isolates the thermocouples) was entirely negligible and required no temperature correction.

The vertical conductive temperature drop through the electrical heater, however, can be appreciable in regions where the surface heat transfer coefficient becomes large, principally the stagnation zone. Solution of the heat equation, through terms

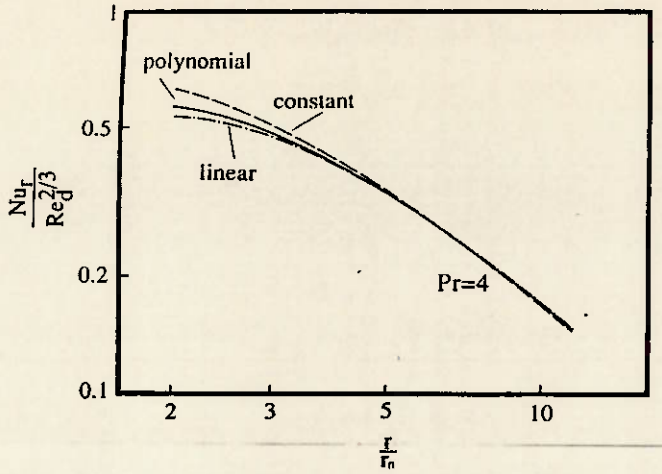

Fig. 4 Effect of initial conditions on the solution of the differential equations in the viscous similarity region for Pr = 4

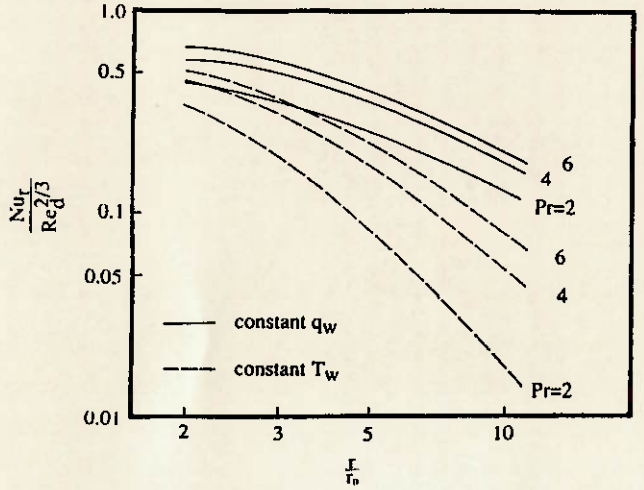

Fig. 5 Comparison of uniform heat flux and uniform temperature wall conditions in the viscous similarity region (from differential equation)

of order $\epsilon = t/d$, shows that the ratio of the true Nusselt number, based on liquid-side temperature ($Nu_t = q_w d/k(T_w - T_f)$) to the measured Nusselt number, based on temperature at the back of the heater ($Nu_m = q_w d/k(T_m - T_f)$) is

$$\frac{Nu_t}{Nu_m} = \frac{1}{1 - \zeta Nu_m/2} \tag{33}$$

where $\zeta = tk/k_w d$ relates the Biot number to the true Nusselt number. This temperature correction was applied in reducing the measured data. For the majority of our measurements, the correction is less than 10 percent of the Nusselt number. However, in the stagnation region, particularly when using the smallest orifice (3.18 mm), the correction could be as large as 30 percent.

For each thermocouple measurement, a number of values were taken to reduce random error. These measured values were averaged to get the actual values for the calculations. The thermocouples were also calibrated under isothermal conditions before and after each run to reduce systematic errors. The wall temperature increases with radius and the local Nusselt number is based on the temperature differences between the wall and the incoming jets. At the stagnation point, the temperature differences are smallest and the uncertainty is largest. For 3/8 in. (9.5 mm) diameter orifice it is ±30 percent. The uncertainty goes down very rapidly as radius increases and for most positions uncertainty is less than ±5 percent. Further reduction of stagnation zone uncertainty, by increasing the heat flux, was untenable as a result of the requirement of minimizing downstream evaporation. The uncertainty for Re_d is less than ±2 percent and that for r is less than ±0.25 mm.

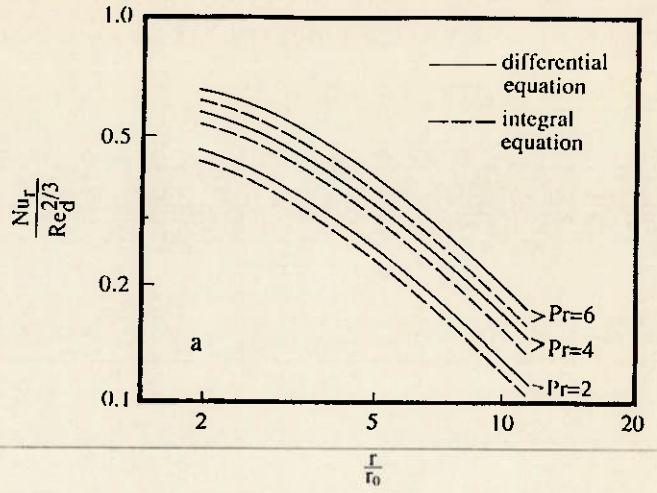

(a)

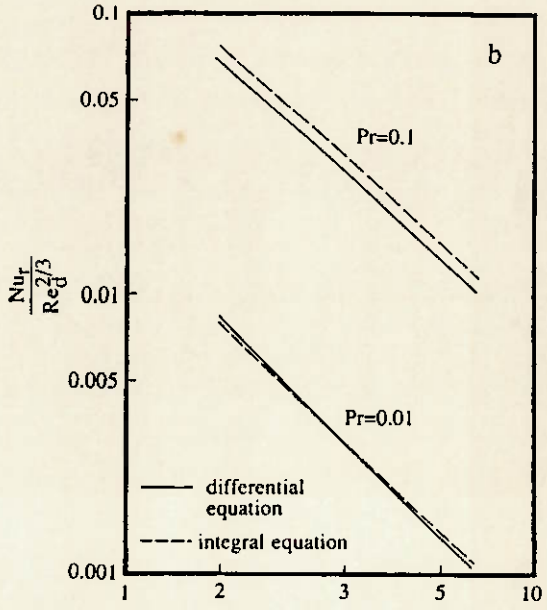

(b)

Fig. 6 Comparison of the solutions from differential and integral analysis of the viscous similarity region at $Re_d = 10^4$ for: (a) Pr > 1; and (b) Pr < 1

Discussion

4.1 Comparison of Integral and Differential Solutions. Numerical integration of the differential equation (22) requires the temperature distribution at the beginning of the similarity region. The exact temperature distribution depends on the upstream stagnation and boundary layer regions. In our calculations, that distribution is based on the polynomial solution from the integral method. However, to test the effects of this initial condition, the computation was also run with an initially linear temperature distribution, between T_w and T_f, in the boundary layer and with a uniform initial temperature, at T_f. The bulk temperatures of these two profiles are larger and smaller, respectively, than that of the polynomial, while the initial slopes of the profiles near the wall are smaller and larger, respectively. Thus, the linear profile gives a lower initial Nu_d and the uniform profile gives a higher initial Nu_d. Figure 4 compares the computations for the different initial temperature profiles. By $r/r_0 = 3$, the difference between the linear, polynomial, and constant initial temperature profiles has decreased to less than 10 percent, and the profiles are indistin-

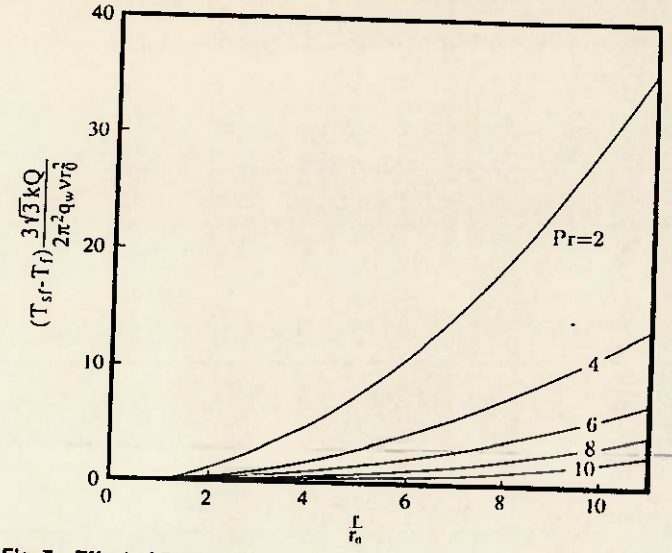

Fig. 7 Effect of Prandtl number on the free surface temperature in the viscous similarity region (from differential equation)

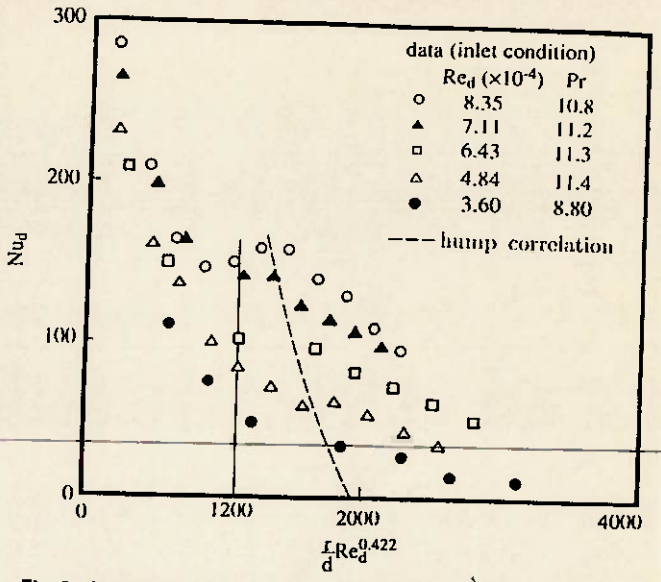

Fig. 9 Turbulent transition as manifested in the Nusselt number

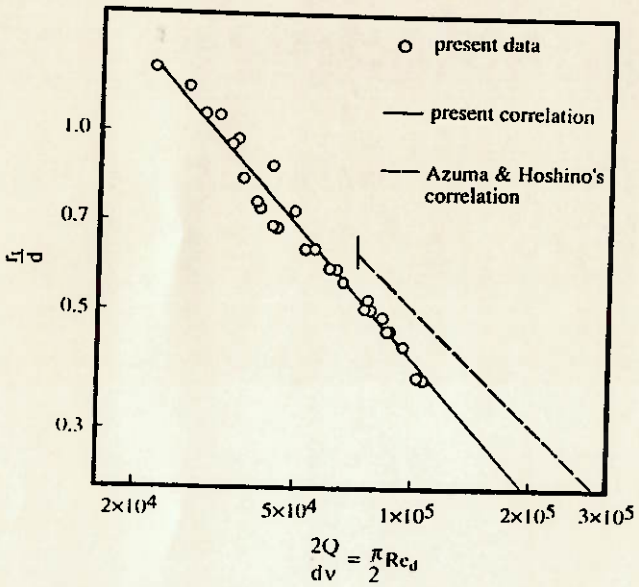

Fig. 8 Radii for transition from laminar to turbulent flow

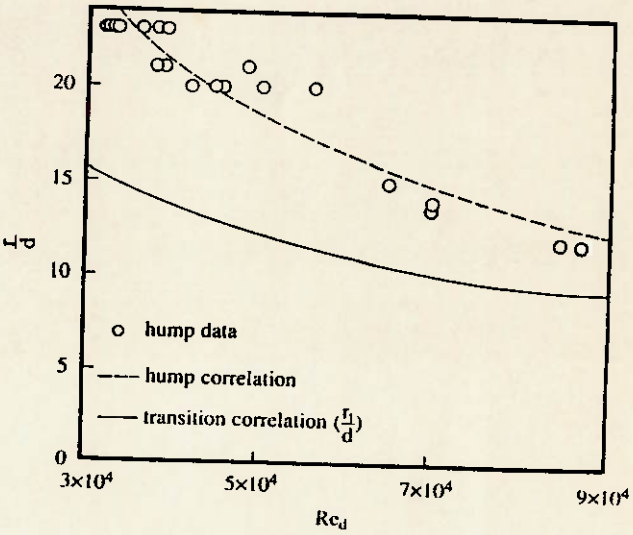

Fig. 10 Transition and hump radii

guishable at larger r/r_0. Thus, the initial temperature distribution has minimal influence on the Nusselt number in the region far from the center, and results based on the polynomial initial distribution are clearly satisfactory. Moreover, these tests show that the heat transfer in the stagnation zone and boundary layer regimes have little effect on the wall temperature at large radii.

Figure 5 compares heat transfer coefficients for uniform wall heat flux (UHF) to those for uniform wall temperature (UWT) from the differential equation solution. In our previous paper, we noted that, in the boundary layer region, the heat transfer coefficient for UHF was 25 percent higher than that for UWT. By contrast, in the similarity region, the difference between boundary conditions increases with increasing radius. Once the thermal boundary layer reaches the free surface, the energy from the wall is absorbed by the entire film, a situation comparable to fully developed duct flow. However, the UHF condition for the radial film differs markedly from the duct flow, in that the heat transfer surface increases linearly with radius. The UHF condition of the jet is akin to a duct flow with flux increasing linearly with axial position, and such a condition is known to produce a higher heat transfer coefficient. This conclusion is not altered by our definition of Nu_d in terms of incoming, rather than bulk, temperature.

The figure shows that, for small Prandtl numbers, the UWT Nusselt number decreases more rapidly than for large Prandtl number, since the driving temperature difference between wall and surface temperature dwindles much faster at low Pr. At $r/r_0 = 10$, the UWT Nusselt number for Pr = 2 is only 9 percent as large as that UHF, and that for Pr = 6 is only 40 percent.

Nusselt numbers from the integral and differential equations are compared in Figs. 6(*a*, *b*) for Pr > 1 and Pr < 1, respectively.[5] For Pr > 1, the maximum difference between the integral and differential solutions is about 10 percent. The integral solution is lower than the differential equation solution as a result of the assumed shape of the temperature distribution. The integral solution neglects the higher order terms in δ_t/δ, which should cause more error as Pr decreases toward unity, but the comparison shows better agreement with the differential equation solution at lower Pr. Apparently, the neglect of higher order terms compensates for the somewhat smoother profile of the integral procedure. For Pr < 1, Fig.

[5]The ordinate $Nu_r/Re_d^{2/3}$ follows naturally from the scaling of the differential equation, but does not carry the full dependence on Re_d.

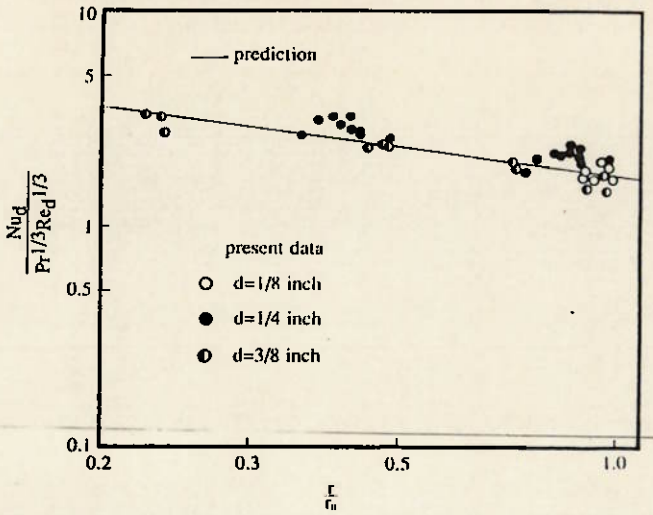

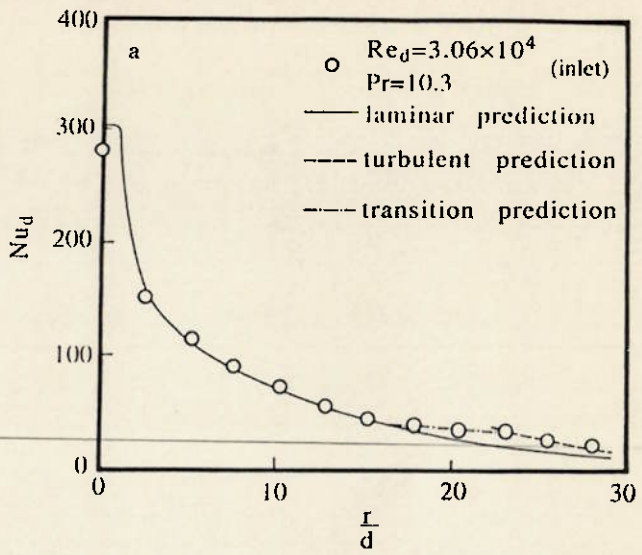

(a)

Fig. 11 Measured and predicted Nusselt number in region 2: data for several diameters of orifice

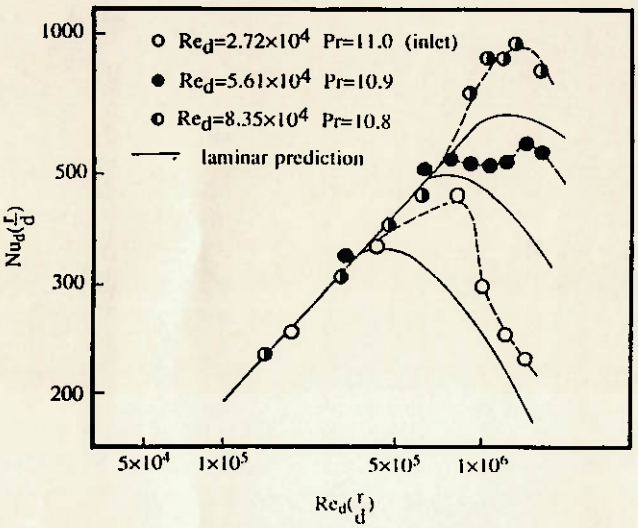

Fig. 12 Nu_r from data and laminar theory for regions 2 and 3 (———: faired curves)

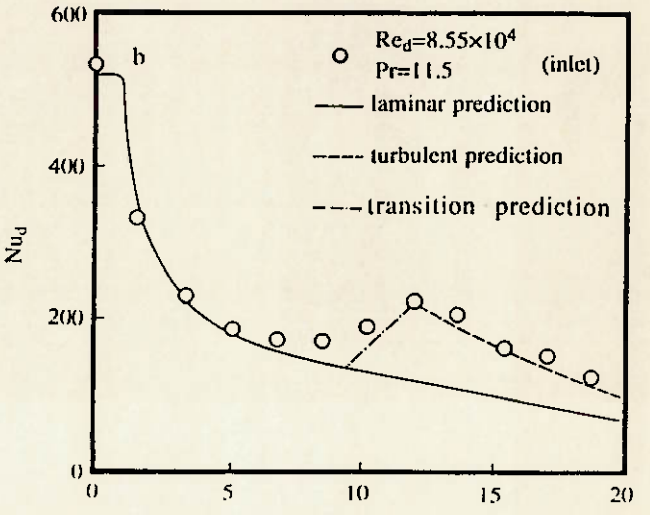

(b)

Fig. 13 Comparison of data to the laminar and turbulent predictions (predictions follow Table 1)

6(*b*) shows the simplified integral results, which neglect all terms in ϕ or Δ. In contrast to Pr > 1, for Pr < 1 the neglected terms are as large as the terms retained when Pr approaches unity. The comparison shows that for Pr = 0.1 the disagreement between the integral and differential equations is more than 20 percent. Fortunately, most liquid metals have Pr near 0.01, and for this case the simplified integral results agree with the differential results to better than 5 percent. For larger Prandtl numbers, the higher order terms should be retained when calculating Nu_d.

From the integral analysis, we previously found that the thermal boundary layer would not reach the free surface for Pr > 5.2. Therefore, for Pr > 5.2, the free surface temperature remains at T_f for all r according to the integral analysis. Of course, this is an approximation based on the assumption of a sharply defined boundary layer. Figure 7 shows the dimensionless free surface temperature from the differential equation solution as function of r/r_0 and illustrates the strong influence of the Prandtl number. For Pr = 2, the surface temperature is more than 11 times higher than for Pr = 10. For Pr > 5.2, the free surface temperature increases much more slowly. However, the surface temperature does rise above the inlet value for Pr > 5.2, and this is another cause of differences between integral and differential solutions for Nu_d.

For engineering purposes, it is convenient to construct a simplified version of the integral or differential predictions. First, we note that, in the Prandtl number range between 1 and 5.2 (for which region 4 is possible), the difference between the integral solutions for region 3 and region 4, if applied at the same Reynolds number and radius, amounts to less than 3 percent. Thus, the equation derived for region 3 can usually be applied as a good approximation in region 4 as well.

For futher simplification, we may consider $r/d \gg 0.322\,Re^{1/3}$ and neglect the terms in d/r and C_3 in the integral result for region 3 (equation (3)):

$$Nu_d = 0.172\,Re_d\,Pr^{1/3}\left(\frac{d}{r}\right)^2 \tag{34}$$

Correlation of the differential equation solutions (accurate to ±9 percent) leads to the following, similar result for $1 < Pr < 100$ and $2.5 < r/r_0 < 100$:

$$Nu_d = 0.195\,Re_d^{0.98}\,Pr^{0.38}\left(\frac{d}{r}\right)^{1.95} \tag{35}$$

For the range $2.5 < r/r_0 < 10$, a slightly better fit (to ±5 percent) is

$$\mathrm{Nu}_d = 0.15\,\mathrm{Re}_d^{0.93}\,\mathrm{Pr}^{0.38}\left(\frac{d}{r}\right)^{1.80} \tag{36}$$

Since a turbulent transition and a hydraulic jump usually occur downstream, the latter equation is more useful. However, neither correlation is reliably accurate in the range $1 \le r/r_0 \le 2.5$; this range is important in practice, and we recommend use of the theoretical prediction, equation (3), in region 3. The integral prediction for region 2 is equation (2). For laminar flow, equations (2) and (3) can be used to estimate the local Nusselt number. These predictions are compared with our experimental data below.

The preceding results do not mean that the identification of regions 3 and 4 is unimportant. In region 4, liquid surface temperature increases rapidly with radius, and evaporation can become very significant. Conversely, in region 3, evaporation can be less important for low initial liquid temperature. Thus, for lower Prandtl numbers, the surface temperature should always be estimated, and, if necessary, the adiabatic surface condition should be dropped in favor of an evaporating surface condition. Surface evaporation was carefully suppressed in the present experiments by cooling the incoming liquid and by limiting the heat flux, but in engineering applications, evaporation will almost always occur. Evaporation will tend to raise Nu_d (Liu and Lienhard, 1989), since it offers an additional heat sink, unless it leads to film dryout downstream, in which case Nu_d will drop disastrously.

The numerical solutions with constant Prandtl number suggest Nusselt number is proportional to Prandtl number to the 0.38 power over Prandtl number from 1 to 100. However, most liquids of high Prandtl number show a rapid decrease in Prandtl number with increasing temperature. Streamwise variations in Pr, as bulk temperature rises, are certainly important and probably outweigh any finer adjustments of the Prandtl number exponents. Best agreement with experimental data was obtained when the values of viscosity (i.e., Re_d) and Pr used in the equations were those corresponding to temperatures at the radial midpoint of the film.

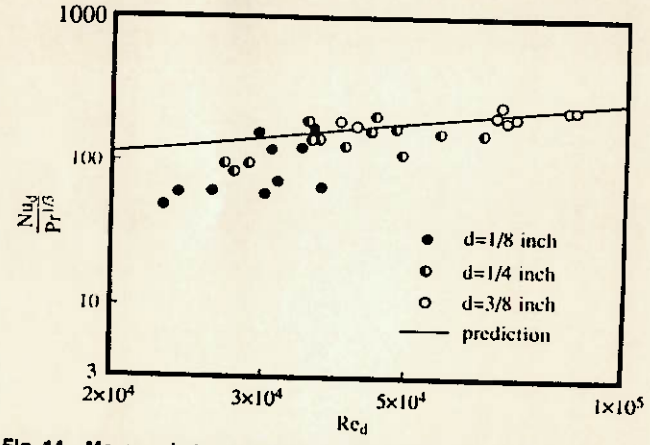

Fig. 14 Measured stagnation point Nusselt number compared to prediction for Pr > 3: data for several diameters of orifice

4.2 Turbulent Transition. The preceding analyses are based on laminar flow and consider neither surface waves nor turbulent transition. Plainly, it is important to know the location of transition from laminar to turbulent flow. If, in addition, turbulence significantly raises the Nusselt number above the laminar prediction, a separate analysis of the turbulent transport is necessary.

Figure 8 shows measurements of the turbulent transition radius in the present system. The transition point is easily identified, since the laminar liquid sheet is smooth and transparent, while the turbulent liquid sheet has a rough surface, which reflects light and appears bright. The associated surface waves are described by Azuma and Hoshino (1984a) as "lattice-shaped" waves. A curve fit of our data (Gabour, 1991) gives the transition radius as

$$\left(\frac{r_t}{d}\right)\mathrm{Re}_d^{0.422} = 1.2\times 10^3 \tag{37}$$

In their own system, Azuma and Hoshino measured

$$\left(\frac{r_t}{d}\right)\mathrm{Re}_d^{0.315} = 0.73\times 10^3 \tag{38}$$

which shows a slightly weaker dependence on Reynolds number, but turbulent transition points normally depend on the disturbances present in a specific system. Equation (37) suggests a coordinate of $(r/d)\,\mathrm{Re}_d^{0.422}$. Using this coordinate, some of the present heat transfer data are shown in Fig. 9. At the transition point, the figure shows a clear shift in the slope of the Nusselt number, which becomes more pronounced at higher Reynolds number. The Nusselt number increases above the laminar trend, as direct comparisons (below) illustrate. Note that the abscissa here is chosen to illustrate the turbulent transition, not the functional dependence of Nu_d on Re_d and Pr; thus, the curves do not collapse to a single line. Moreover, the streamwise changes in the Re_d and Pr dependencies make it impossible to present all of our data, for many different conditions, on a single graph. In this and following figures, we present enough data to illustrate the general behavior without attempting to be exhaustive.

The Nusselt numbers show a hump downstream of the turbulent transition point. This hump corresponds to the point at which the turbulence has become fully developed (see heat transfer predictions below). As the Reynolds number increases, the hump becomes more pronounced and occurs after shorter distance. The transition and hump radii are shown as a function of jet Reynolds number in Fig. 10. The data for the hump position can be correlated as

Table 1 Suggested formulae for local Nusselt number for Pr ≥ O(1)

Region	Range	Nu_d
Stagnation zone	$0 \le r/d < 0.787,\quad 0.15 \le \mathrm{Pr} \le 3$ $\mathrm{Pr} > 3$	$0.715\,\mathrm{Re}_d^{1/2}\mathrm{Pr}^{0.4}$ $0.797\,\mathrm{Re}_d^{1/2}\mathrm{Pr}^{1/3}$
Transition: stagn. to b.l.	$0.787 < r/d < 2.23$	$\left(\frac{2I}{\pi\rho}\mathrm{Re}_d\mathrm{Pr}\frac{r}{d}\right)^{1/3}$
b.l. region (2)	$2.23 < r/d < 0.1773\,\mathrm{Re}_d^{1/3}$	$0.632\,\mathrm{Re}_d^{1/2}\mathrm{Pr}^{1/3}\left(\frac{d}{r}\right)^{1/2}$
Similarity region (3 & 4)	$0.1773\,\mathrm{Re}_d^{1/3} < r/d < 1200\,\mathrm{Re}_d^{-0.422}$ $(r_0/d < r/d < r_t/d)$	$\frac{0.407\,\mathrm{Re}_d^{1/3}\mathrm{Pr}^{1/3}\left(\frac{d}{r}\right)^{2/3}}{\left[0.1713\left(\frac{d}{r}\right)^2+\frac{5.147\,r_0}{\mathrm{Re}_d d}\right]^{2/5}\left[\frac{1}{2}\left(\frac{r}{d}\right)^2+C_3\right]^{1/5}}$ $\left(C_3=\frac{0.267\,(d/r_0)^{1/2}}{\left[0.1713\left(\frac{d}{r_0}\right)^2+\frac{5.147\,r_0}{\mathrm{Re}_d d}\right]^2}-\frac{1}{2}\left(\frac{r_0}{d}\right)^2\right)$
Transition: laminar/turb	$1200\,\mathrm{Re}_d^{-0.422} < r/d < 2.86\times 10^4\,\mathrm{Re}_d^{-0.68}$	$\mathrm{Nu}_{lam}(r_t)+[\mathrm{Nu}_{turb}(r_h)-\mathrm{Nu}_{lam}(r_t)]\frac{(r-r_t)}{(r_h-r_t)}$
Turbulent region	$r/d > 2.86\times 10^4\,\mathrm{Re}_d^{-0.68}$	$\frac{8\,\mathrm{Re}_d\mathrm{Pr}\,f(C_f,\mathrm{Pr})}{49(h/r)(r/d)+28(r/d)^2 f(C_f,\mathrm{Pr})}$

$$\left(\frac{r_h}{d}\right)\mathrm{Re}_d^{0.68}=2.86\times10^4 \tag{39}$$

Recall that the border of region 2 is $r_0/d = 0.1773\mathrm{Re}_d^{1/3}$. This implies that if $\mathrm{Re}_d > 1.1 \times 10^5$, the transition will take place in region 2. For the present Reynolds number range, transition always occurs in the similarity region (region 3). Indeed, the stability analysis of Azuma and Hoshino (1984d) suggests that the flow will always be most unstable near the border of regions 2 and 3, with waves or turbulence commencing in the similarity region.

Figure 11 shows a comparison of the data to the integral solution (equation (2)) in region 2. The agreement is generally within the uncertainty of the data. This region is relatively small. In this region, small concentric ripples can be observed (called "disturbance" waves by Azuma and Hoshino). These waves do not develop significantly, and they appear to have no strong effect on the heat transfer.

In the similarity region, our heat transfer data show a clear transition from laminar to turbulent flow. Azuma and Hoshino (1984a) report a critical (transition) discharge Reynolds number, based on the jet diameter, of 4.8×10^4. From our data this critical discharge Reynolds number is much lower (less than 2×10^4). This discrepancy may be caused by the definition of the critical discharge Reynolds number adopted by Azuma and Hoshino. They regarded the flow to be turbulent when the so-called "sandpaperlike" waves are present over 50 percent of the azimuthal direction, and took that discharge Reynolds number as the critical value. That type of situation never occurs in the present experiments; here with increasing Reynolds number, waves and disturbances inside the liquid sheet intensify, but the transition circle stays essentially circular and symmetric at all Re_d.

The laminar analysis predicts that for a given Re_d, $\mathrm{Nu}_r = (r/d)\,\mathrm{Nu}_d$ reaches a peak value and then decreases. Figure 12, however, shows two features that differ from the prediction. The first is that the data break from the initially linear portion of the laminar prediction at a higher value of Nu_r than predicted. The other is a sharp peak in Nu_r downstream of the change in slope. The first feature suggests, from our observations and those of Azuma and Hoshino's (1984a, 1984d), that the disturbance waves have intensified in this portion of the film. They appear to increase the heat transfer coefficients by up to 20 percent in this short region, which is just ahead of the transition radius where sandpaperlike waves occur (see also Fig. 13*b*). The second feature, the peak, is simply the hump at full development of turbulence, as previously discussed.

The friction coefficient measurements and mass transfer data of Nakoryakov et al. show a very similar behavior. The primary difference is that turbulent transition, as deduced from their friction coefficient measurements, occurs in the boundary layer region (region 2). Their data show a single peak rather than the pair of features seen here. This suggests that the sheet has become turbulent before surface waves can contribute significantly to the heat transfer. They attribute the peak to waves rather than turbulent transition. However, for their Reynolds number range, the turbulent transition is a more likely explanation.

4.3 Prediction of Turbulent Heat Transfer. The Nusselt number turbulent flow may be calculated using the thermal law of the wall. The Stanton number is defined as

$$\mathrm{St}=\frac{q_w}{\rho c_p u_{\max}(T_w-T_{sf})} \tag{40}$$

and the law of the wall may be written in the standard internal-flow form

$$\mathrm{St}=\frac{C_f/2}{1.07+12.7(\mathrm{Pr}^{2/3}-1)\sqrt{C_f/2}}=f(C_f,\,\mathrm{Pr}) \tag{41}$$

The skin friction coefficient is calculated from the Blasius law

$$C_f=0.045\left(\frac{\nu}{u_{\max}h}\right)^{1/4}=0.073\mathrm{Re}_d^{-1/4}\left(\frac{r}{d}\right)^{1/4} \tag{42}$$

where the 1/7 power turbulent velocity distribution produces a maximum velocity

$$u_{\max}=\frac{1}{7}\frac{u_f d^2}{hr} \tag{43}$$

and a film thickness h of

$$h=d\left(\frac{0.02091}{\mathrm{Re}_d^{1/4}}\left(\frac{r}{d}\right)^{5/4}+C\frac{d}{r}\right) \tag{44}$$

with

$$C=0.1713+\frac{5.147r_t}{\mathrm{Re}_d\,d}-\frac{0.02091}{\mathrm{Re}_d^{1/4}}\left(\frac{r_t}{d}\right)^{1/4} \tag{45}$$

From the above, the Nusselt number for turbulent flow may be calculated:

$$\mathrm{Nu}_d=\frac{8\mathrm{Re}_d\mathrm{Pr}f(C_f,\,\mathrm{Pr})}{49\left(\frac{h}{r}\right)\left(\frac{r}{d}\right)+28\left(\frac{r}{d}\right)^2 f(C_f,\,\mathrm{Pr})} \tag{46}$$

When $\mathrm{Pr} \gg 1$, the equation simplifies to

$$\mathrm{Nu}_d=0.0052\mathrm{Re}_d^{3/4}\left(\frac{d}{h}\right)\left(\frac{d}{r}\right)^{3/4}\left(\frac{\mathrm{Pr}}{1.07+12.7(\mathrm{Pr}^{2/3}-1)\sqrt{C_f/2}}\right) \tag{47}$$

The turbulent Nusselt number is substantially higher than the laminar Nu_d.

Figures 13(*a*, *b*) show the laminar and turbulent predictions together with experimental data for two runs at different Reynolds numbers. In both cases, agreement is excellent. The increasing strength of turbulent augmentation with increasing Reynolds number is also quite apparent. The only significant disagreement observed is in the stagnation zone for lower Reynolds number. Data and predictions for the stagnation zone are discussed in the next section.

4.4 Stagnation Zone Heat Transfer. In the stagnation zone of a body passing through an infinite fluid medium, White (1974) finds

$$\mathrm{Nu}_d=G(\mathrm{Pr},\,3)\left(\frac{Bd^2}{\nu}\right)^{1/2} \tag{48}$$

where

$$G(\mathrm{Pr},\,3)=\begin{cases}0.53898\mathrm{Pr}^{0.4} & 0.15\le\mathrm{Pr}\le3.0\\ 0.6010\mathrm{Pr}^{1/3}-0.05085 & \mathrm{Pr}\ge3.0\end{cases}$$

The value of $B = 2\partial u/\partial r$ at the stagnation point of an inviscid impinging liquid jet was calculated approximately by Schach (1935)[6]

$$B=1.76\,\frac{u_f}{d} \tag{49}$$

This value should be applicable for reasonably large jet Reynolds numbers.

From these results

$$\mathrm{Nu}_d=\begin{cases}0.715\,\mathrm{Re}_d^{1/2}\mathrm{Pr}^{0.4} & 0.15\le\mathrm{Pr}\le3\\ 0.797\,\mathrm{Re}_d^{1/2}\mathrm{Pr}^{1/3} & \mathrm{Pr}>3\end{cases} \tag{50}$$

Figure 14 compares the data to the above equations, illustrating generally good agreement. The data appear to fall below the

[6]Schach's Figs. 9 and 10 are a bit garbled. This often-quoted value is obtained from his $\partial v/\partial z$ and continuity.

prediction at lower Reynolds numbers. This behavior may be related to a decrease in the stagnation zone velocity gradient owing to viscous effects, but further study is required.

Nakoryakov et al. (1978) measured the Nusselt number for mass transfer beneath an impinging jet at high Schmidt number with uniform wall concentration. They did not directly test a relation for the stagnation zone transport. Instead, they used a relation for Nu (equation (1)) to calculate their jet velocities. The relation they used seems to be quite close to that suggested above, although its origin remains obscure (it does not appear in the reference they cite). Nakoryakov et al. also measured wall shear stress in the stagnation zone, but the calibration of their stress probe was similarly based on an assumed value of $\partial u/\partial r$.

Stevens and Webb (1989) used a pipe-type nozzle producing turbulent incoming jets, and their measured Nusselt numbers are in the same general range, although a bit higher, than the present data. They represented their stagnation zone results by a correlation that accounts for the Reynolds number dependence of the stagnation velocity gradient with a dimensional correlating factor of u_f/d

$$\mathrm{Nu}_d = 2.67\mathrm{Re}_d^{0.57}\left(\frac{z}{d}\right)^{-1/30}\left(\frac{u_f}{d}\right)^{-1/4}\mathrm{Pr}^{0.4} \tag{51}$$

where z is the distance of their nozzle from the heater. This correlation shows a somewhat different dependence on jet diameter and velocity than is found for the present laminar jets. Stevens and Webb present a second correlation for the radial variation Nu_d, which does not represent the present data well at the large radii of interest to us, although it does represent their own data very well for r/d less than about 5.

The size of the stagnation zone may be estimated by calculating the radius at which the stagnation boundary layer and the region 2 boundary layer have the same thickness (i.e., $2.107\,d\,\mathrm{Re}_d^{1/2} = 2.679\,(rd/\mathrm{Re}_d)^{1/2}$; White, 1974; Sharan, 1984). The result is

$$\frac{r_m}{d} = 0.787 \tag{52}$$

Similarly, Stevens and Webb found the stagnation region beneath a turbulent jet to reach to roughly $r/d = 0.75$. Our crude estimate shows that the stagnation zone is very small. Its primary importance is that it possesses the maximum local heat transfer coefficient (lowest wall temperature) in the flow. It contributes little, however, to overall heat removal or downstream Nusselt numbers as may be seen from the full integral result for region 2 (Liu and Lienhard, 1989), which does not neglect the stagnation zone heat flow as does equation (2):

$$\mathrm{Nu}_d = \left(\frac{\frac{27}{80}\mathrm{Re}_d\mathrm{Pr}\frac{r}{\delta}}{\frac{1}{2}\left(\frac{r}{d}\right)^2 + C_2}\right)^{1/3} \tag{53}$$

with $\delta = 2.679\,(rd/\mathrm{Re}_d)^{1/2}$. At $r = r_m$, the Nusselt number should equal the stagnation zone Nusselt number; thus,

$$C_2 = -0.2535 \tag{54}$$

The error in Nu_d caused by neglecting the stagnation zone is less than 10 percent for $r/d > 2.23$.

4.5 Recommendations for Nusselt Number Estimation. Table 1 summarizes the suggested relations for estimating local Nusselt number for impinging, circular, free liquid jets. For most regions, deviations are less than 10 percent. For laminar convection in the similarity region, however, waves can enhance the heat transfer, and Nu_d may exceed the estimate by up to 20 percent; as the waves are damped, the heat transfer goes back down. The wavy region is relatively small, however, because it is limited by subsequent turbulent transition. In the region of transition from laminar to turbulent flow, between r_t and r_h, we tentatively recommend a line fit between the laminar predictions at r_t and the turbulent prediction at r_h. This fit is shown in Figs. 13 (*a*, *b*) and can be seen not to account properly for the wave effects that occur in that region at larger Reynolds number. With the exceptions of this line fit and the correlation for r_t/d, all equations in Table 1 are analytical predictions; each is substantiated by experiment.

4.6 Additional Studies Required. In jet impingement cooling applications, turbulent incoming jets are likely to be produced, since upstream disturbances are not usually damped and the jets often issue from pipes. While turbulence may enhance stagnation point heat transfer, it is damped sharply as the film spreads. We are currently conducting experimental studies of turbulent jet heat transfer.

Impinging jets will splatter if the jet surface is even slightly disturbed or the thin liquid sheet is disturbed beyond a certain magnitude. Disturbances to the incoming jet are often caused by irregularities in the orifice or by turbulence in the liquid supply. Roughness of the target surface can also disturb the liquid film. Splattering removes liquid from the liquid film, and thus lowers the Nusselt number; Liu and Lienhard (1989) estimated reductions of 20 percent or more. We are also investigating the role of splattering in jet impingement cooling.

Finally, the behavior of the stagnation zone at lower Reynolds number will be further investigated, owing to surface tension effects and a possible viscous decrease of the stagnation velocity gradient as Re_d becomes smaller.

Conclusions

Convective heat removal by liquid jet impingement has been investigated for uniform wall flux and circular, laminar jets. Both theoretical and experimental results are given.

- The radial distribution of Nusselt number is accurately predicted by the formulae in Table 1 for Prandtl numbers of order unity or greater.
- Laminar heat transfer in the film for $\mathrm{Pr} \geq O(1)$ may be calculated from equation (2) in the boundary layer region (region 2) and by equation (3) in the laminar portion of the similarity region (regions 3 and/or 4). These regions are described in Section 2.1.
- Laminar heat transfer predictions for $\mathrm{Pr} < 1$ are developed in Section 2.2.
- Comparison of the integral predictions to numerical solutions in the similarity region supports conclusions previously drawn from the integral approach for $\mathrm{Pr} > 1$ as well as the new results for $\mathrm{Pr} < 1$.
- Turbulent transition occurs at a radius given by equation (37). Turbulence becomes fully developed at a radius given by equation (39). Turbulent heat transfer in the film is given by equation (46).
- The stagnation point Nusselt number is reasonably well represented by equation (50).

Acknowledgments

The authors are grateful to Ms. Laurette A. Gabour for her measurements of the turbulent transition radius and to Mr. Vittal K. Vasista for construction of the flow loop. This project was supported by grants from the A. P. Sloan Foundation and the National Science Foundation (grant No. CBT-8858288).

References

Azuma, T., and Hoshino, T., 1984a, "The Radial Flow of a Thin Liquid Film, Part 1: Laminar-Turbulent Transition," *Trans. Japan Soc. Mech. Engrs.*, Vol. 50, p. 974.

Azuma, T., and Hoshino, T., 1984b, "The Radial Flow of a Thin Liquid Film, Part 2: Film Thickness," *Trans. Japan Soc. Mech. Engrs.*, Vol. 50, p. 902.

Azuma, T., and Hoshino, T., 1984c, "The Radial Flow of Thin Liquid Film, Part 3: Velocity Profile," *Trans. Japan Soc. Mech. Engrs.*, Vol. 50, p. 1126.

Azuma, T., and Hoshino, T., 1984d, "The Radial Flow of Thin Liquid Film, Part 4: Stability of Liquid Film and Wall Pressure Fluctuation," *Trans. Japan Soc. Mech. Engrs.*, Vol. 50, p. 1136.

Carper, H. J., 1989, "Impingement Cooling by Liquid Jet," presented at the ASME Winter Annual Meeting, San Francisco, CA.

Chaudhury, Z. H., 1964, "Heat Transfer in a Radial Liquid Jet," *J. Fluid Mech.*, Vol. 20, pp. 501–511.

Errico, M., 1986, "A Study of the Interaction of Liquid Jets With Solid Surfaces," Doctoral Thesis, University of California at San Diego.

Gabour, L. A., 1991, "Heat Transfer to Turbulent and Splattering Impinging Liquid Jets," S. B. Thesis in Mechanical Engineering, MIT, Cambridge, MA.

Ishigai, S., Nakanishi, S., Mizuno, M., and Imamura, T., 1977, "Heat Transfer of the Impinging Round Water in the Interference Zone of Film Flow Along the Wall," *Bulletin of the JSME*, Vol. 20, No. 139.

Liu, X., and Lienhard V, J. H., 1989, "Liquid Jet Impingement Heat Transfer on a Uniform Flux Surface," *Heat Transfer Phenomena in Radiation, Combustion, and Fires*, ASME HTD-Vol. 6, pp. 523–530.

Lombara, J. S., 1990, "An Experimental Investigation of Liquid Jet Impingement Heat Transfer Theories," S. B. Thesis in Mechanical Engineering, MIT, Cambridge, MA.

Nakoryakov, V. E., Pokusaev, B. G., and Troyan, E. N., 1978, "Impingement of an Axisymmetric Liquid Jet on a Barrier," *Int. J. Heat Mass Transfer*, Vol. 21, pp. 1175–1184.

Olsson, R. G., and Turkdogan, E. T., 1966, "Radial Spread of a Liquid Stream on a Horizontal Plate," *Nature*, Vol. 211, No. 5051, pp. 813–816.

Schach, W., 1935, "Umlenkung eines kreisförmigen Flussigkeitsstrahles an einer ebenen Platte senkrecht zur Strömungsrichtung," *Ing.-Arch.*, Vol. 6, pp. 51–59.

Schlichting, H., 1979, *Boundary-Layer Theory*, 7th ed., McGraw-Hill, New York.

Sharan, A., 1984, "Jet-Disc Boiling: Burnout Predictions and Application to Solar Receivers," Master's Thesis in Mechanical Engineering, University of Houston, TX.

Stevens, J., and Webb, B. W., 1989, "Local Heat Transfer Coefficients Under an Axisymmetric, Single-Phase Liquid Jet," *Heat Transfer in Electronics—1989*, ASME HTD-Vol. 111, pp. 113–119.

Vasista, V. K., 1989, "Experimental Study of the Hydrodynamics of an Impinging Liquid Jet," Bachelor's Thesis in Mechanical Engineering, MIT, Cambridge, MA.

Wang, X. S., Dagan, Z., and Jiji, L. M., 1989a, "Heat Transfer Between a Circular Free Impinging Jet and a Solid Surface With Nonuniform Wall Temperature or Wall Heat Flux—1. Solution for the Stagnation Region," *Int. J. Heat Mass Transfer*, Vol. 32, No. 7, pp. 1351–1360.

Wang, X. S., Dagan, Z., and Jiji, L. M., 1989b, "Heat Transfer Between a Circular Free Impinging Jet and a Solid Surface With Nonuniform Wall Temperature or Wall Heat Flux—2. Solution for the Boundary Layer Region," *Int. J. Heat Mass Transfer*, Vol. 32, No. 7, pp. 1361–1371.

Wang, X. S., Dagan, Z., and Jiji, L. M., 1989c, "Conjugate Heat Transfer Between a Laminar Impinging Liquid Jet and a Solid Disk," *Int. J. Heat Mass Transfer*, Vol. 32, No. 11, pp. 2189–2197.

Watson, E. J., 1964, "The Radial Spread of a Liquid Over a Horizontal Plane," *J. Fluid Mech.*, Vol. 20, pp. 481–499.

White, F. M., 1974, *Viscous Fluid Flow*, McGraw-Hill, New York.

Local Heat Transfer Coefficients Under an Axisymmetric, Single-Phase Liquid Jet

J. Stevens
Research Assistant.

B. W. Webb
Assistant Professor.
Mem. ASME

Department of Mechanical Engineering,
Brigham Young University,
Provo, UT 84602

The purpose of this investigation was to characterize local heat transfer coefficients for round, single-phase free liquid jets impinging normally against a flat uniform heat flux surface. The problem parameters investigated were jet Reynolds number Re, nozzle-to-plate spacing z, and jet diameter d. A region of near-constant Nusselt number was observed for the region bounded by $0 \le r/d \le 0.75$, where r is the radial distance from the impingement point. The local Nusselt number profiles exhibited a sharp drop for $r/d > 0.75$, followed by an inflection and a slower decrease thereafter. Increasing the nozzle-to-plate spacing generally decreased the heat transfer slightly. The local Nusselt number characteristics were found to be dependent on nozzle diameter. This was explained by the influence of the free-stream velocity gradient on local heat transfer, as predicted in the classical analysis of infinite jet stagnation flow and heat transfer. Correlations for local and average Nusselt numbers reveal an approximate Nusselt number dependence on $Re^{1/3}$.

Introduction

Impinging jets are widely used in industrial heat and mass transfer applications. Due to their high transfer coefficients, air jets have been widely used in the paper and textile industries for drying, while water jets have been used for controlled cooling in the glass and metal industries. Recently, there has also been interest in using the high heat transfer coefficients under impinging jets to deal with the escalating heat fluxes found in advanced technology VLSI circuits (Kiper, 1984; Yamamoto et al., 1987).

Impinging jets can be grouped according to several broad characteristics. In general, a jet is called a submerged jet if it is a gas jet issuing into a gas, or a liquid jet issuing into a liquid, and will be termed a free jet if it is a liquid jet issuing into a gas. In addition, impinging jets can be classified by their shape, their temperature relative to the surface against which they are impinging, whether the jet is oriented normally or obliquely with respect to the impingement surface, and whether the impingement surface is flat or curved.

The purpose of this investigation was to characterize local transfer coefficients for round, single-phase free liquid jets impinging normally against a flat, constant-heat-flux surface. The problem parameters investigated were jet Reynolds number, nozzle-to-plate spacing, and jet diameter.

A significant amount of research has been published on various forms of jet impingement heat transfer. Only a representative sample of studies involving single-phase impinging liquid jets issuing into gas surroundings will be cited here.

Theoretical studies include work by Watson (1964) who used boundary layer theory to examine the fluid mechanics of an impinging liquid jet, and Chaudhry (1964) who treated the heat transfer aspect of the same problem and presented solutions for an isothermal impingement surface. In addition, Miyazaki and Silberman (1972) provided an analytical solution to a planar laminar jet striking a flat plate. A theoretical and experimental treatment of local heat transfer coefficients under a planar laminar water jet was offered by Inada et al. (1981). More recently, Wang et al. (1989a, 1989b) provided a theoretical treatment of the heat transfer under a laminar, axisymmetric, free liquid jet with nonuniform temperature or heat flux thermal boundary conditions.

Experimental studies were carried out by Jiji and Dagan (1987) for single jets and arrays of jets using water and FC-77 coolant for various heat source configurations. Average heat transfer data were reported. McMurray et al. (1966) investigated local heat transfer characteristics of a planar liquid jet striking a uniform heat flux plate at various impingement angles. Local heat transfer data were gathered by moving the instrumented heater relative to the jet stagnation plane. Metzger et al. (1974) examined experimentally the effect of Prandtl number on heat transfer for axisymmetric liquid jets. Average

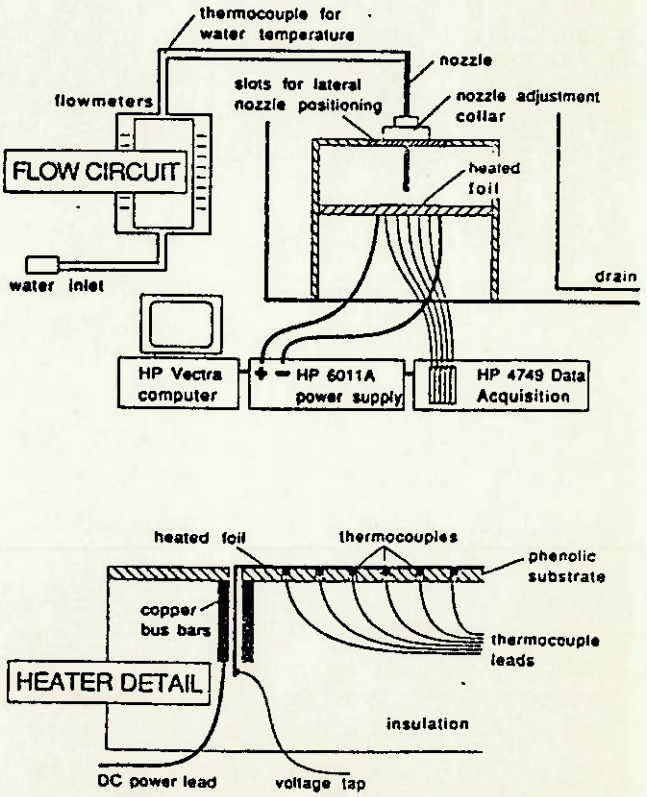

Fig. 1 Schematic of experimental apparatus

Contributed by the Heat Transfer Division and presented at the National Heat Transfer Conference, Philadelphia, Pennsylvania, August 6–9, 1989. Manuscript received by the Heat Transfer Division April 21, 1989; revision received May 14, 1990. Keywords: Electronics Equipment, Forced Convection, Jets.

heat transfer coefficient measurements were made for various heat source and nozzle diameter combinations using water and lubricating oil as the working fluids. The effects of Reynolds number, fluid Prandtl number, and ratio of heat source target to jet nozzle diameters on average heat transfer were correlated using the equation

$$\overline{Nu} = 2.74 Re^{0.348} Pr^{0.487} (2r/d)^{-0.774} (\mu_o/\mu_{aw})^{-0.37} \quad (1)$$

where μ_o and μ_{aw} are the fluid dynamic viscosities at the wall and free stream, respectively. Recently, the heat transfer characteristics of a single-phase, planar impinging jet were studied (Vader, 1988; Vader et al., 1990). Local heat transfer correlations were presented for various jet Reynolds numbers for a single nozzle size. Ma and Bergles (1988) examined experimentally the local heat transfer under a circular, submerged jet of R-113. Some measurements of free jet impingement were included for comparison with the submerged jet data.

The brief literature survey presented in the foregoing reveals no studies documenting the local heat transfer behavior of impinging, axisymmetric liquid jets. This paper reports on experimental work whose objective was to fill this critical gap in the jet impingement heat transfer data base. Local heat transfer coefficients under axisymmetric, single-phase liquid jets have been measured for a broad range of experimental parameters.

Experiments

An instrumented heated foil and metered flow delivery system were designed and constructed to permit determination of local heat transfer coefficients under a single-phase impinging water jet. The local heat transfer coefficient was calculated from measurements of the local electrical power dissipated at the heating element, and local heated surface and free-stream liquid temperature measurements. The apparatus and experimental method used in the study are described in more detail in sections to follow.

Experimental Apparatus. Figure 1 illustrates schematically the experimental apparatus used in this research. Water from a laboratory outlet passed through two flow meters, which provided a combined measurement range of 0.0063 to 0.76 L/s with accuracy of ±0.0006 L/s. A thermocouple in the pipe immediately downstream from the flow meters was used to measure the water temperature. The water was then directed into a glass tube, which served as a nozzle. The exit of the tube was carefully ground so as to be perpendicular to the tube axis. Glass tubes of inside diameter 2.2, 4.1, 5.8, and 8.9 mm were used as nozzles. All tubes were 38 cm long. This length was chosen in order to insure fully developed flow at the nozzle outlet (over 50 diameters for three of the nozzles, and 43 diameters for the other) since previous studies with air have indicated that the velocity profile at the jet exit may have a significant effect on the heat transfer results (Hrycak, 1984; Gardon and Akfirat, 1965). Test Reynolds numbers were chosen such that turbulent flow prevailed in all tests. The nozzle was secured in an aluminum collar mounted on a Lexan and steel frame (see Fig. 1). This insured that the jet impinged normally aginst the heated surface and permitted adjustment of the nozzle-to-plate spacing. The collar was attached to the top plate with screws, which passed through slots milled in the Lexan. This arrangement allowed the jet to be moved in a horizontal plane parallel to the heater. However, the horizontal movement was only intended for rough jet positioning. Hence, local heat transfer measurements were determined only from the thermocouple array mounted to the underside of the foil without utilizing the coarse movement capability of the nozzle to increase temperature measurement resolution. The second level of the frame held the heating plate.

A schematic cross section of the instrumented heating plate is illustrated in Fig. 1. The heating element consisted of a rectangular section of 0.0508-mm-thick stainless steel (type 302) shim stock. The shim stock was 1.5 cm wide, with 8.0 cm of length exposed to the jet. It was secured to a 20.3 × 20.3 cm piece of 1.59-mm-thick phenolic (printed circuit board material) using Dow Corning silicone rubber sealant. The silicone rubber was used in order to provide flexible adhesion in case of thermal expansion of the heating foil. The phenolic backing was prepared by using a numerically controlled mill to cut two slots, exactly 8.0 cm apart, through which the shim stock was passed. Twenty-eight holes, 1.5 mm in diameter on 2.5 mm centers, were drilled in the phenolic substrate for thermocouple placement. The mill was used in order to allow precise positioning of the thermocouple holes. After the shim stock was cemented in place, thermocouples (fabricated from 0.127-mm-dia Cu-Co wire) were inserted through the holes in the phenolic sheet and were attached directly to the shim stock with Loctite QM-50 epoxy. Intimate thermal contact between thermocouple beads and the heater strip was guaranteed by insuring electrical continuity between the heated foil and the thermocouple leads.

Possible electrical interaction between the d-c power employed in the Ohmic heating and the thermocouple beads affixed directly to the foil was considered in the apparatus checkout. Tests were conducted in a typical experimenal flow situation to insure that the d-c voltage gradient in the foil did not influence the thermocouple measurements. It was found that reversing the clarity of the d-c power supply (thus, reversing the direction of voltage gradient) resulted in less than 3 percent change in local Nusselt number near the stagnation point, with approximately 5 percent elsewhere. The variation is attributed to slightly different conduction losses in the bus bars due to transient heatup of the apparatus. In spite of the expected high heat transfer coefficients, the shim stock was characterized by a low local Biot number (typically 0.017–0.1) making it reasonable to assume that the temperature of the back surface of the shim stock was identical to the surface exposed to the fluid.

The water jet impinged against the center of the heating element and flowed radially off the sides of the lower Lexan plate where it was collected and directed to a drain. The heated foil was clamped firmly between 2.5 × 10 cm copper bus bars, which were connected with heavy copper wire leads to a 20-V, 120-A d-c power supply. Voltage and current measurements

Nomenclature

d = jet diameter
h = local heat transfer coefficient $= q_w/(T_s - T_\infty)$
k = thermal conductivity
Nu = local Nusselt number based on jet diameter $= hd/k$
Nu_o = stagnation point Nusselt number $= h_o d/k$
$\overline{Nu}$ = average Nusselt number from stagnation point to radial distance $r = q_w d/k\Delta T$
Pr = fluid Prandtl number $= \nu/\alpha$
q_w = wall heat flux imposed at the heating plate
Q = volume heat rate
r = radial distance from stagnation point
r_{hj} = radial distance to location of hydraulic jump
Re = Reynolds number based on jet diameter $= 4Q/\pi d\nu$
T_s = local surface temperature of the plate
T_∞ = jet exit temperature
U = infinite jet free-stream velocity, equation (4)
v = mean jet velocity at nozzle exit
z = nozzle-to-plate spacing
ν = kinematic viscosity

were made with remote sensing leads soldered to heating foil tabs extending through the bus bars, and were accurate to ±0.1 V and ±0.1 A. All thermal components were read with an HP model 3497A data acquisition system with thermocouple compensation. The accuracy in temperature differences was estimated to be ±0.25°C.

Experimental Method. In determining appropriate power supply settings, it was found that 5 V produced approximately 50 A, and that this power rate provided temperature differences large enough to be accurately resolvable (minimum temperature differences typically greater than 4°C) without overheating the plate for most flow rates. The data acquisition system ran continuously during the test and recorded temperature scans at 15-s intervals. These continuous data sets provided a means for determining when a steady-state condition was reached after a change in operating conditions. At the beginning of each test run, the jet was centered over one thermocouple by moving the jet collar manually in the upper Lexan sheet until the temperatures were radially symmetric on both sides of a single thermocouple.

The data acquisition system collected temperature measurements continuously in time, so for each configuration, the beginning and ending scan numbers were recorded along with the water flow rate (read from the rotameters), nozzle-to-plate spacing (measured with a scale), power supply readings, and nozzle size (measured with precision calipers). After the test run was completed, the extraneous output gathered by the data acquisition system was eliminated so as to include only the scans between each starting and ending scan number. As stated previously, the system was allowed to reach steady state before each set of scans was begun. Hence, each set of multiple scans included only steady-state data. Temporally averaged temperature differences, jet Reynolds numbers, local heat transfer coefficients, local Nusselt numbers, and local average Nusselt numbers were then calculated from the experimental heat flux and local heated surface temperature data.

The temporally averaged temperature difference used in the determination of heat transfer coefficients was calculated by computing the mean difference between water temperature and local plate temperature for the set of scans corresponding to each test configuration. All water properties were evaluated at the jet inlet temperature. This approximation was valid near the stagnation point where temperature differences were small (of order 5°C), and less valid in the jet wings where temperature differences were as high as 30°C. It will be shown that the correlations presented here present only a lower bound for the local heat transfer in the jet wings. A temperature measurement was taken on the back of the phenolic plate in order to assess the heat loss through the plate. That loss was determined to be insignificant (less than 0.5 percent) and no correction was used. Thermocouple leads were drawn from the test apparatus along expected isotherms to minimize conduction losses there. Heat transfer coefficients were so high that conduction losses in the electrical bus bars were minimal.

When an axisymmetric free liquid jet impinges against a flat plate, a hydraulic jump forms in the liquid layer as it spreads over the plate. This is due to the deceleration of the fluid as it expands radially in an ever-thinning liquid layer. This hydraulic jump phenomenon was observed in this study, and with it a substantial decrease in local heat transfer coefficient (Stevens, 1988). However, all heat transfer data reported here were collected with the hydraulic jump located well beyond the edge of the heated plate. Because the hydraulic jump is an important issue in liquid jet impingement heat transfer, the location of the hydraulic jump was correlated and is characterized in a section to follow.

The maximum uncertainty in the local Nusselt numbers was determined to be approximately 8 percent using the method of Kline and McClintock (1953). A similar uncertainty should be applied to the local average data since they were derived by integrating the local data. The maximum uncertainty for Reynolds number values was calculated to be 6.8 percent. In light of these uncertainties, variations in Nu or $\overline{Nu}$ of less than 8 percent, and variations dependent on changes in Re of less than 7 percent, are not meaningful. The maximum uncertainty in radial position of the local temperature measurements was estimated to range from 4 percent of the nozzle diameter for the $d = 8.9$ mm nozzle, to 17 percent of the nozzle diameter for the $d = 2.2$ mm nozzle.

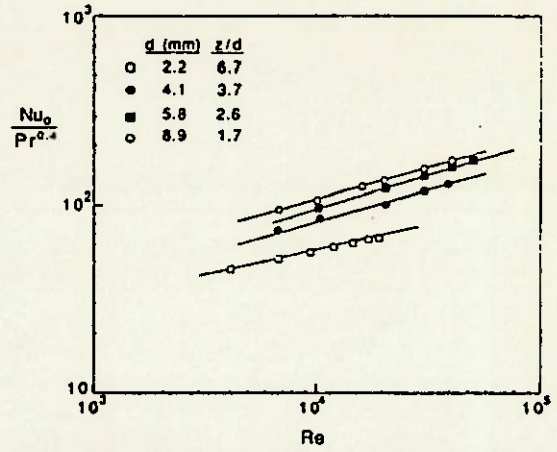

Fig. 2 Dependence of stagnation Nusselt number on Reynolds number for the four nozzle diameters studied

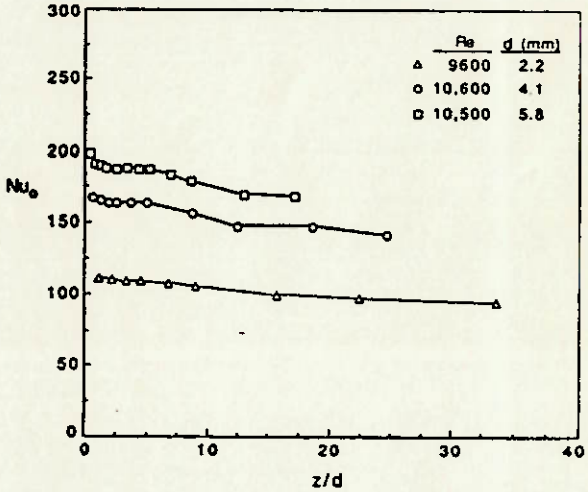

Fig. 3 Dependence of stagnation Nusselt number on nozzle-to-plate spacing, *z/d*

Results and Discussion

Local temperature data were collected using the experimental apparatus and reduced as described in the foregoing for nozzle sizes ranging from 2.2 to 8.9 mm and nominal jet Reynolds numbers ranging from 4000 to 52,000. Experimental results are presented in the sections that follow.

Stagnation Point Nusselt Number. Stagnation point Nusselt number data were collected and correlated over the full range of jet diameter, nozzle-to-plate spacing, and Reynolds number investigated. For the set of experimental data corresponding to each nozzle diameter, it was found that the Nu_o data correlated well with an equation of the form

$$Nu_o = A Re^q (z/d)^s Pr^{0.4} \quad (2)$$

where a multivariate least-squares curve fit was performed to determine the parameters A, q, and s. The Prandtl number

ible 1 Correlation coefficients for stagnation Nusselt number, equation (2)

Nozzle size (mm)		2.2	4.1	5.8	8.9
A		5.36	3.75	3.62	5.08
q		0.27	0.33	0.35	0.33
s		−0.052	−0.035	−0.032	−0.023

pendence for liquid jet impingement has been characterized ith exponents ranging from 0.33 to 0.487 (Jiji and Dagan, 87; Ma and Bergles, 1983; Metzger et al., 1974; Vader et ., 1990). A value of 0.4 was chosen for this study. Table 1 ows the values of the coefficients A, q, and s in equation) for the four nozzle diameters investigated.

Figure 2 shows a sample of the stagnation point Nusselt mber dependence on Reynolds number for several data sets, ong with the correlation for each given by equation (2). As served by the exponent q in Table 1, the stagnation Nusselt mber is described quite well by a power-law dependence on eynolds number, $Re^{1/3}$. This compares favorably with the $^{0.348}$ relationship observed by Metzger et al. (1974). Although e Metzger correlation is for average Nusselt number, the eynolds number dependence comparison for Nu_o as defined re is valid inasmuch as average Nusselt number scales directly ith stagnation Nusselt number. While previous investigations liquid jet impingement generally correlate as $Nu_o \propto Re^{1/2}$ Wang et al., 1989a, 1989b; Ma and Bergles, 1988; Miyazaki d Silberman, 1972; Sitharamayya and Raju, 1969; Mcurray et al., 1966), only the study by Metzger, et al., uses und, free liquid jets for the basis of the correlation, and ne have investigated such a broad range in nozzle diameters used in this study.

As reflected by the small exponent of z/d in Table 1, the fect of the nozzle-to-plate spacing on Nusselt number is slight. igure 3 shows Nu_o plotted as a function of z/d for three ozzle sizes at a nominal Reynolds number of 10,000. The neral trend is that of a slight decrease in Nu_o with increasing ozzle-to-plate spacing, z/d. This agrees qualitatively with the ee jet Nu_o dependence on z/d of Ma and Bergles (1988), hich is significantly less than for a submerged jet. There is o distinctive peak in the Nu_o versus z/d curves as reported r circular air jets by Hrycak (1983), and for plane air jets y Gardon and Akfirat (1966) and others. This can be explained y noting that those peaks were attributed to the formation f a potential core due to the effect of entrainment on the ubmerged jets. Such shear layer interaction and entrainment ould be much less important for a free liquid jet. The z/d ependence may be characterized generally for all nozzle diameters using an exponent of $s = -0.0336$ with little loss of rrelation accuracy.

Noting the small exponent on z/d in Table 1, and examining ne data of Figs. 2 and 3, one observes a distinct dependence f heat transfer on nozzle size. The Nusselt numbers rise consistently with nozzle diameter. The use of dimensionless parameters (Nu, Re, r/d, z/d) based on nozzle diameter does not liminate dependence on d in the results. Previous work (Vader t al., 1990; Donaldson, 1971) indicates that the velocity gradient exercises a significant influence on the local heat transfer. his is further justified by the analytical solution for rotationally symmetric, laminar stagnation flow from an infinite t (Burmeister, 1983). Theory reveals that the heat transfer oefficient is independent of r, and is given by

$$h = 1.013k(3C/\nu)^{1/2} \tag{3}$$

here the constant 1.013 is for $Pr = 10$ fluids, and the freestream velocity distribution is assumed to be given $U = Cr$. The alue of the velocity gradient is then given by

$$C = dU/dr \tag{4}$$

lthough equation (3) is derived for the case of a constant-

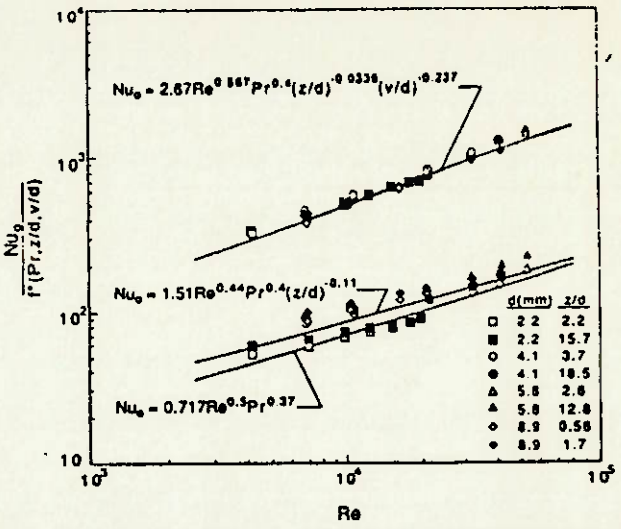

Fig. 4 Correlation of stagnation Nusselt number data using equations (6) and (7), and comparison with the laminar flow analysis of Wang et al. (1989a), equation (8)

temperature surface with impingement by a normally impinging, laminar flow of infinite extent, it does demonstrate that the velocity gradient is an important parameter in stagnation flow. It may be postulated that the stagnation velocity gradient would still be important for the case of a turbulent, finite, free liquid jet under consideration here. Hence, it is not surprising that the stagnation heat transfer characteristics for the four nozzle sizes studied here differ, since the velocity gradient at the stagnation point is nozzle diameter dependence. Such a pronounced nozzle size dependence on the stagnation Nusselt number has not previously been reported in the literature. However, as explained previously, no other work has investigated *local* heat transfer over such a broad diameter range of free, turbulent liquid jets.

The constant C is shown to represent the velocity gradient by White (1974), and is evaluated for a circular liquid jet as 0.88 (v/d) by Wang et al. (1989a) and Nakoryakov et al. (1978) using a laminar flow field. Substitution of this expression into equation (3) yields the result that Nu is proportional to $Re^{1/2}$. This is also Wang's finding (1989a), and is identical to Sibulkin's solution (1952) in the stagnation region for constant heat flux or constant temperature thermal boundary conditions

$$Nu_o = 0.938Re^{1/2}\int_0^\infty \exp\left[-2Pr\int_0^\eta \phi d\eta\right]d\eta \tag{5}$$

where ϕ is the similarity function describing the flow field. While the Reynolds number dependence may differ, it seems reasonable to assume that the parameter v/d would also describe functionally the stagnation velocity gradient in a turbulent, finite jet. It is recognized that the influence of turbulence may result in a nonlinear dependence of the velocity gradient, dU/dr, on the term v/d. In addition, a consideration of mass and momentum near the stagnation point supports the use of v/d as a velocity gradient scaling parameter. The disadvantage is that v/d is a dimensional quantity of units s^{-1} and there is no obvious reference time scale for use in its normalization.

Inclusion of the velocity gradient as an important parameter leads to $(dU/dr)(d/v)$ as the obvious nondimensional velocity gradient. Unfortunately, no independent method for measuring dU/dr was available in this investigation, leaving only the dimensional term v/d to estimate dU/dr as discussed above. Inasmuch as the proposed velocity gradient effect was originally manifest as a nozzle diameter dependence, and since both turbulence and the finite nature of the jet are presumed to be important, an alternative approach would be to use a dimensionless turbulence characterization parameter of the form $d/$

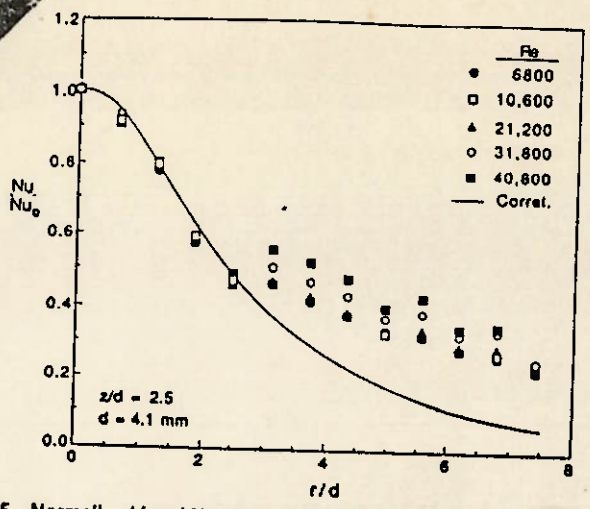

Fig. 5 Normalized local Nusselt number profiles and correlation equation (10) for all Reynolds numbers studied, $z/d = 2.5$, $d = 4.1$ mm

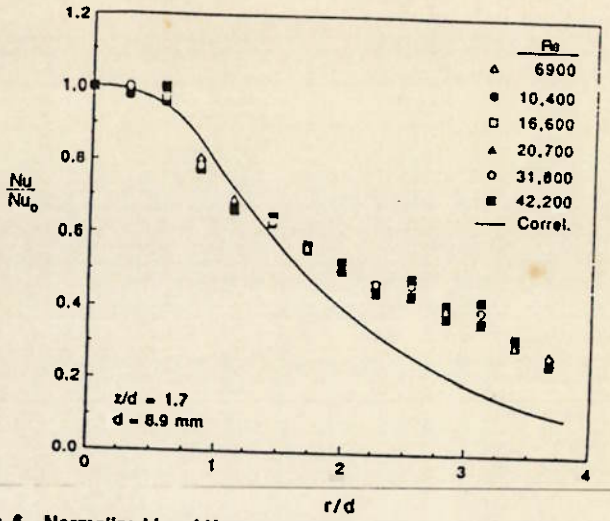

Fig. 6 Normalized local Nusselt number profiles and correlation equation (10) for all Reynolds numbers studied, $z/d = 1.7$, $d = 8.9$ mm

l, where l is the turbulent length scale of the flow. Unfortunately, this approach breaks down since l is proportional to d for fully developed pipe flow (Schlichting, 1968). However, if v is employed as a correlating parameter, the dependence of Nu_o on nozzle diameter vanishes and the four correlations of equation (2) and Table 1 collapse to a single expression

$$Nu_o = 2.67Re^{0.567}Pr^{0.4}(z/d)^{-0.0336}(v/d)^{-0.237} \quad (6)$$

where v is expressed in m/s and d in m. Experimental data representing the full range of z/d studied are plotted in Fig. 4 along with equation (6) in the form $Nu_o/f^*(Pr, z/d, v/d)$ where $f^*(Pr, z/d, v/d)$ is the relationship describing the functional dependence on Pr, z/d, and v/d appropriate to the correlation. Also included in Fig. 4 are the same set of experimental stagnation Nusselt number data and the corresponding correlation of all data *without* employing v/d as a correlating parameter. That empirical relation is given by

$$Nu_o = 1.51Re^{0.44}Pr^{0.4}(z/d)^{-0.11} \quad (7)$$

Equation (6) predicts the experimental data with an average and maximum error of 5 and 14 percent, respectively, for all nozzle sizes, jet-plate spacings, and jet Reynolds numbers investigated, a total of 228 tests representing different nozzle diameters and geometric and flow conditions. By contrast, the average and maximum error in equation (7) are 15 and 60 percent, respectively. Also shown in Fig. 4 is Wang's laminar flow solution (1989a) to equation (5), which has been solved over the range of Prandtl number $0.5 \le Pr \le 50$, and which is correlated very well by the equation

$$Nu_o = 0.717Re^{0.5}Pr^{0.37} \quad (8)$$

The significantly better accuracy of correlating equation (6) lends support to the idea that the (stagnation) heat transfer is dependent on the local velocity gradient, and hence, will be strongly affected by the nozzle diameter. As is expected, the experimental data generally exhibit higher heat transfer than the laminar analysis, equation (8), due to the influence of jet turbulence on the heat transfer.

Local Nusselt Number. Figures 5 and 6 show plots of the local Nusselt number normalized by Nu_o for the $d = 4.1$ and 8.9-mm-dia nozzles, respectively. Correlations for Nu/Nu_o to be developed in subsequent sections are also included in the figures. Since the data were symmetric about the stagnation point to within 5 percent, only half-profiles were plotted. Examination of local Nusselt number plots yielded several interesting observations.

First, in the region corresponding approximately to $r/d < 2$–3, it is seen that Nu/Nu_o is nearly independent of Reynolds number, with all curves collapsing to a single profile. Since the dependence on z/d is slight, Nu/Nu_o can be considered to be a function only of r/d in this region. At points far from the stagnation point, a Reynolds number dependence appears in the Nu/Nu_o profiles and the curves diverge. This Re dependence is believed due to a transition to turbulent flow and heat transfer in the flow along the plate, and is discussed in more detail in a section to follow.

Second, the local heat transfer profiles exhibit a region of constant Nu from the stagnation point out to a distance of approximately $r/d = 0.75$, seen most clearly for the largest nozzle (Fig. 6). This is consistent with the classical analytical result for rotationally symmetric stagnation flow of an infinite jet referred to in the foregoing, where the heat transfer coefficient is predicted to be independent of radial position (Burmeister, 1983). Since the flow of a finite liquid jet such as those used in this study would approximate an infinite jet flow very near the stagnation point, one would expect that the Nusselt number would be constant in that region. The near-constant Nu profile observed near the stagnation point for the largest nozzle is evidence of this effect. The absence of such a constant-Nu region for the smaller nozzles can be explained by noting that the thermocouples were located at fixed radial positions, so for the smaller nozzles the spatial resolution of heated surface temperature measurements was insufficient to show the constant-Nu region. Presumably, more finely resolved measurements on the smallest nozzle would show a flat region around the stagnation point similar to the profiles for the largest nozzle.

Third, a sharp knee appears in all local data profiles beyond which the Nu/Nu_o profiles separate and a dependence on Reynolds number surfaces. This knee was located at approximately $r/d = 5.0$, 2.5, 1.75, and 0.9 in the 2.2, 4.1, 5.8, and 8.9-mm-dia nozzle data, respectively (Stevens, 1988). In all cases, Nu/Nu_o drops off rapidly until it reaches the knee, then either flattens out and decreases more slowly thereafter, or rises briefly to a secondary maximum in the profile. These secondary peaks were found to appear at higher Re for the two smaller nozzles. When such a peak occurs, its beginning always coincides with the knee discussed above, and it becomes more pronounced with increasing Re. For the smallest nozzle the peak occurred at $r/d = 5.5$ and was evident for $Re > 12{,}400$ in all but the smallest nozzle-to-plate spacing. For the $d = 4.1$ mm nozzle, the secondary peak appears at $r/d = 3$ and occurs for $Re > 21{,}000$ (see Fig. 5). The secondary peaks were less prominent in the two largest nozzles. Examination of the profiles for the $d = 4.1$ mm diameter nozzle (Fig. 5) shows that the

Table 2 Correlation coefficients for local Nusselt number, equations (9) and (10)

Nozzle size (mm)		2.2	4.1	5.8	8.9
a		1.15	1.34	1.48	1.57
b		−0.23	−0.41	−0.56	−0.70

knee discussed above becomes more pronounced with increasing Re until, first, a region of constant Nu develops, then a secondary peak appears for the highest Reynolds numbers. This suggests that flat regions in the profiles with higher Re for the larger nozzles might be precursors to secondary peaks, which could have been observed had even higher Re been measured.

Similar secondary peaks were observed for circular air jets by Hrycak (1983) for $z/d>6$, and in slot air jets for very small nozzle-to-plate spacings by Korger and Krizek (1966), and Gardon and Akfirat (1966), and were attributed to the transition from a laminar to turbulent boundary layer. In addition, similar peaks were observed in plane water jets (Inada et al., 1981; Vader et al., 1990). In this study, both the knee and the secondary peak in the profiles are attributed to the transition from a laminar to turbulent boundary layer in the parallel flow region along the plate.

Correlation of Local Nusselt Number. The development of an empirical correlation for the local Nusselt number behavior was influenced by two observations. First, as discussed in the foregoing, upstream of the transition point, Nu/Nu_o is a function only of r/d. Second, the presence of the near-constant-Nu section in the profile at small r/d suggested the use of two asymptotes: a constant heat transfer coefficient asymptote for $r/d<0.75$ (motivated by the constant Nu result of the analytical solution for an infinite jet), and an exponential asymptote between $r/d=0.75$ and the transition point. In all cases, the knee in the profile was taken to be the location of the transition point.

In consideration of the first point, it was decided to formulate correlations for the local Nusselt number profiles based on the normalized curves (Nu/Nu_o), with independent correlations for Nu_o as outlined in equation (6).

From the general shape of the normalized curves, a correlation was chosen of the form

$$f(r/d)=ae^{b(r/d)} \tag{9}$$

(where a and b are constants determined for each nozzle) for the region between $r/d=0.75$ and the transition point. In order to make an appropriate transition between the constant-Nu ($r/d<0.75$) and exponential-Nu ($r/d>0.75$) regimes, a procedure suggested by Churchill and Usagi (1972) was used. This consists of using a correlation equation of the form:

$$Nu/Nu_o=[C^{-P}+f(r/d)^{-P}]^{-1/P} \tag{10}$$

where C is the small r/d asymptote, $f(r/d)$ [from equation (9)] is the exponential asymptote, and P is an exponent to be determined. The local Nusselt numbers were normalized by the stagnation Nusselt number, $C=1$. For each nozzle, the normalized data between $r/d=0.75$ and the transition point were fit with least-squares regression to determine the coefficients for the exponential function. Then, the parameter P from equation (10) was determined by using a least-squares fit of all of the normalized data, and was found to be relatively insensitive to nozzle diameter. A value of $P=9.0$ may be used with good accuracy in the correlation equation (10). Table 2 shows the other correlation coefficients used.

Figures 5 and 6 include samples of the local Nusselt number correlation given by equations (9) and (10). This correlation applies only to the region before transition occurs at approximate r/d locations of 5.0, 2.5, 1.5, and 1.0 for the 2.2, 4.1, 5.8, and 8.9 mm diameter nozzles, respectively. Beyond that

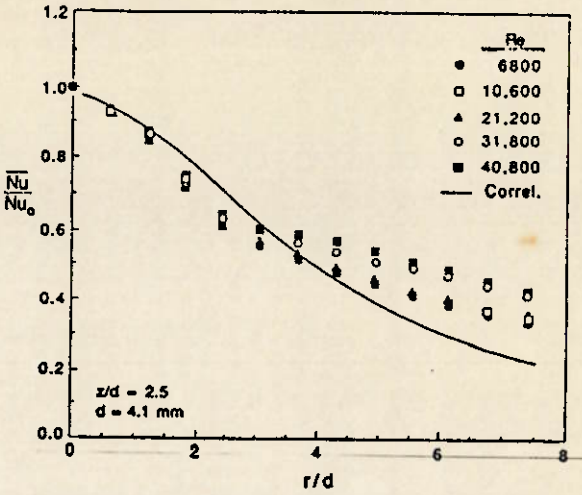

Fig. 7 Normalized local average Nusselt number profiles and correlation equation (13) for all Reynolds numbers studies, $z/d=2.5$, $d=4.1$ mm

point, the correlation serves as a lower bound on the local heat transfer, but does not accurately predict the Nu/Nu_o data. In the spatial region prior to transition to turbulent flow, equation (10) represents 87 percent of the data within ±15 percent, and 96 percent of the data within ± 20 percent.

Average Nusselt Number. The local average Nusselt number was calculated by integrating the experimental local Nusselt number data using the usual definition for isoflux heating

$$\overline{Nu}/Nu_o=(r/d)^2/2\int_0^{r/d}\frac{(r'/d)d(r'/d)}{(Nu/Nu_o)} \tag{11}$$

where $\overline{Nu}$ is the average Nusselt number over the circular region from the stagnation point to r/d. The definition of equation (11) indicates that the average Nusselt number is based on the average temperature difference, $\overline{Nu}=q_w d/k\Delta\overline{T}$. Hence, for a given and spatially constant heat flux, the average temperature difference may be determined with a correlation for $\overline{Nu}$. In practice, the integration for the local Nusselt number in equation (11) was performed using the trapezoidal rule. Figure 7 is a plot of the normalized local average Nusselt number, $\overline{Nu}/Nu_o$, calculated according to equation (11) for the experimental data of Fig. 5. The local average Nusselt number profiles show Re and r/d dependence similar to the local results discussed above, except that the averaging tends to smooth the curves. Consequently, the secondary maxima observed in Fig. 5, attributed to transition from a laminar to a turbulent boundary layer, are not evident in the average heat transfer data of Fig. 7.

Since the local average Nusselt numbers were derived by numerically integrating the local Nusselt number data, the correlation for $\overline{Nu}/Nu_o$ may, in theory, be determined by substituting the expansion for Nu/Nu_o from equation (10) into equation (11), and performing the integration. The integration, however, is intractable. A new correlation for $\overline{Nu}/Nu_o$ was developed by integrating equation (9) with respect to r/d, yielding

$$g(r/d)=\frac{2}{(r/d)^2}\left\{\frac{f(r/d)}{b}\left[r/d-\frac{1}{b}\right]+\frac{a}{b^2}\right\} \tag{12}$$

The correlating procedure of Churchill and Usagi was used again with the new function $g(r/d)$ used as the high-r/d asymptote. The final form of the $\overline{Nu}/Nu_o$ correlation is

$$\overline{Nu}/Nu_o=[1+g(r/d)^{-P'}]^{-1/P'} \tag{13}$$

The values for P' were determined by a new least-squares curve fit. As with the correlating parameter P in equation (10), the parameter P' of equation (13) was found to be relatively in-

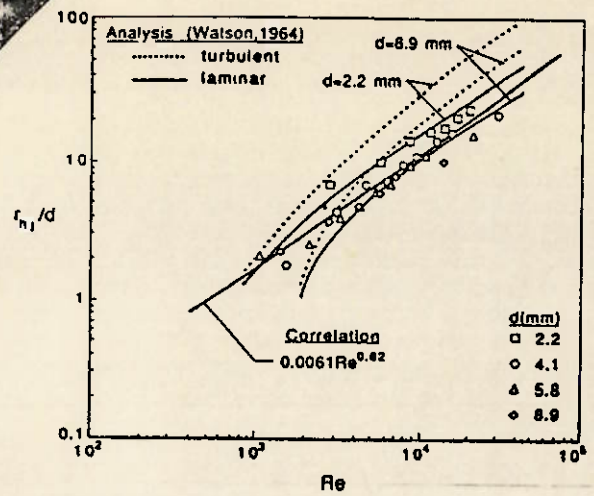

Fig. 8 Correlated location of the hydraulic jump as a function of jet Reynolds number

sensitive to nozzle diameter; a value of $P'=7.0$ predicts the $\overline{Nu}/Nu_o$ data quite well. Again, considering only the spatial region prior to the transition to turbulent flow, equation (13) represents 89 percent of the data within ±10 percent and 99.7 percent of the data within ±15 percent. The correlation of the average Nusselt number is compared to the experimental data in Fig. 7.

Hydraulic Jump. As mentioned in the foregoing, an interesting effect that occurs when a liquid jet impinges vertically against a flat plate is the formation of a hydraulic jump as the fluid decelerates and spreads in a thin layer over the plate (Watson, 1964). As would be expected, a sharp decrease in the local heat transfer coefficient associated with the hydraulic jump was observed experimentally (Stevens, 1988).

Some coarse measurements of the dependence of the radial location of the hydraulic jump on Reynolds number were carried out. It should be noted that the location of the hydraulic jump oscillated in an unsteady manner, and could only be measured with an estimated accuracy of ±0.5 cm. Hence, the r_{hj}/d data exhibit considerable scatter. The jump location was correlated with Reynolds number using an equation of the form

$$r_{hj}/d = m\mathrm{Re}^n \qquad (14)$$

Figure 9 illustrates the measured r_{hj}/d data along with the correlation. The correlation parameters $m=0.0061$ and $n=0.82$ predict the r_{hj}/d location with an average error of 15 percent. Watson's theoretical prediction (1964) for the location of the hydraulic jump for the two nozzle diameter extremes studied experimentally is also shown. The Reynolds number dependence for both laminar and turbulent flow is illustrated. The analysis requires knowledge of the liquid layer thickness downstream of the hydraulic jump, and a value of 3 mm was used based on crude measurements. Although the analysis shows rather poor quantitative agreement with the experimental data, the correct trends are predicted. For a given Reynolds number the diameter-normalized hydraulic jump location is smaller for the larger nozzles. Additionally, the analysis shows relatively good agreement in slope of the r_{hj}–Re relationship for $\mathrm{Re}>4000$. Although the nozzle diameter clearly influences the location of the hydraulic jump in the experimental data, no attempt was made to quantify the relationship due to the obvious uncertainty in the data.

Conclusions

This investigation characterized local heat transfer coefficients for an axisymmetric water jet impinging normally against a flat, constant heat flux plate. It was found that Nusselt number varied with $\mathrm{Re}^{1/3}$ for a given jet diameter. A region of constant local heat transfer coefficient was discovered to prevail in the region bounded by $0\le r/d\le 0.75$. Beyond there, local Nusselt number profiles exhibited a sharp drop, a bend in the profile, and a slower decrease thereafter. In some cases, a secondary peak occurred after the initial decrease. Where it appeared, this secondary peak was more pronounced with increasing Re. These secondary maxima were attributed to transition to a turbulent boundary layer. Nozzle-to-plate spacing was found to have only a minor effect on the magnitude of the local heat transfer. It was determined that the local heat transfer coefficient was clearly influenced by nozzle size, and this was explained in terms of the dependence on the free-stream velocity gradient. When this dependence was accounted for by including the velocity gradient scaling parameter v/d in the correlation, the nozzle size dependence vanished. A brief consideration of the hydraulic jump quantified its location as a function of jet Reynolds number.

Acknolwedgments

This work was supported by the National Science Foundation under Grant No. CBT-8552493.

References

Burmeister, L. C., 1983, *Convective Heat Transfer*, Wiley, New York.

Chaudhry, Z. H., 1964, "Heat Transfer in a Radial Liquid Jet," *Journal of Fluid Mechanics*, Vol. 20, pp. 501–511.

Churchill, S. W., and Usagi, R., 1972, "A General Expression for the Correlation of Rates of Transfer and Other Phenomenon," *AIChE Journal*, Vol. 18, No. 6, pp. 1121–1128.

Donaldson, C. D., Snedeker, R. S., and Margolis, D. P., 1971, "A Study of Free Jet Impingement, Part 2: Free Jet Turbulent Structure and Impingement Heat Transfer, *Journal of Fluid Mechanics*, Vol. 45, pp. 477–512.

Gardon, R., and Akfirat, J. C., 1965, "The Role of Turbulence in Determining the Heat Transfer Characteristics of Impinging Jets," *International Journal of Heat and Mass Transfer*, Vol. 8, pp. 1261–1272.

Gardon, R., and Akfirat, J. C., 1966, "Heat Transfer Characteristics of Impinging Two-Dimensional Air Jets," ASME JOURNAL OF HEAT TRANSFER, Vol. 88, pp. 101–108.

Hrycak, P., 1983, "Heat Transfer From Impinging Jets to a Flat Plate," *International Journal of Heat and Mass Transfer*, Vol. 26, pp. 1857–1865.

Hrycak, P., 1984, "Heat Transfer From Impinging Jets to a Flat Plate With Conical and Ring Protuberances," *International Journal of Heat and Mass Transfer*, Vol. 27, pp. 2145–2154.

Inada, S., Miyasaka, Y., and Izumi, R., 1981, "A Study on the Laminar-Flow Heat Transfer Between a Two-Dimensional Water Jet and a Flat Surface," *Bulletin of the JSME*, Vol. 24, pp. 1803–1810.

Jiji, L. M., and Dagan, Z., 1987, "Experimental Investigation of Single Phase Multi-Jet Impingement Cooling of an Array of Microelectronic Heat Sources," *Proceedings of the International Symposium on Cooling Technology for Electronic Equipment*, Pacific Institute for Thermal Engineering, HI, pp. 265–283.

Kiper, A. M., 1984, "Impinging Water Jet Cooling of VLSI Circuits," *International Communications in Heat and Mass Transfer*, Vol. 11, pp. 517–526.

Kline, S. J., and McClintock, F. A., 1953, "Describing Uncertainties in Single-Sample Experiments," *Mechanical Engineering*, Jan., pp. 3–12.

Korger, M., and Krizek, F., 1966, "Mass-Transfer Coefficient in Impingement Flow From Slotted Nozzles," *International Journal of Heat and Mass Transfer*, Vol. 9, pp. 337–344.

Ma, C. F., and Bergles, A. E., 1983, "Boiling Jet Impingement Cooling of Simulated Microelectronic Chips," in: *Heat Transfer in Electronic Equipment*, S. Oktay and A. Bar-Cohen, eds., ASME, New York, pp. 5–12.

Ma, C. F., and Bergles, A. E., 1988, "Convective Heat Transfer on a Small Vertical Heated Surface in an Impinging Circular Liquid Jet," *The Second International Symposium on Heat Transfer*, Vol. I, Beijing, China, pp. 248–255.

McMurray, D. C., Myers, P. S., and Uyehara, O. A., 1966, "Influence of Impinging Jet Variables on Local Heat Transfer Coefficients Along a Flat Surface With Constant Heat Flux," *Proceedings of the 3rd International Heat Transfer Conference*, Vol. 2, pp. 292–299.

Metzger, D. E., Cummings, K. N., and Ruby, W. A., 1974, "Effects of Prandtl Number on Heat Transfer Characteristics of Impinging Liquid Jets," *Proceedings of the 5th International Heat Transfer Conference*, Vol. II, pp. 20–24.

Miyazaki, H., and Silberman, E., 1972, "Flow and Heat Transfer on a Flat Plate Normal to a Two-Dimensional Laminar Jet Issuing From a Nozzle of Finite Height," *International Journal of Heat and Mass Transfer*, Vol. 15, pp. 2097–2107.

Nakoryakov, V. W., Pokusaev, B. G., and Troyan, E. N., 1978, "Impingement of an Axisymmetric Liquid Jet on a Barrier," *International Journal of Heat and Mass Transfer*, Vol. 21, pp. 1175–1184.

Schlichting, H., 1968, *Boundary Layer Theory*, McGraw-Hill, New York.

Sibulkin, M., 1952, "Heat Transfer Near the Forward Stagnation Point of a Body of Revolution, *Journal of Aeronautical Sciences*, Vol. 19, pp. 570–571.

Sitharamayya, S., and Raju, K. S., 1969, "Heat Transfer Between an Axisymmetric Jet and a Plate Held Normal to the Flow," *The Canadian Journal of Chemical Engineering*, Vol. 47, pp. 365–368.

Stevens, J. W., 1988, "Measurements of Local Heat Transfer Coefficients: Results for an Axisymmetric, Single-Phase Water Jet Impinging Normally on a Flat Plate With Uniform Heat Flux," M.S. Thesis, Brigham Young University, Provo, UT.

Vader, D. T., 1988, "Convective and Boiling Heat Transfer From a Heated Surface to an Impinging, Planar Jet of Water," Ph.D. Thesis, Purdue University, West Lafayette, IN.

Vader, D. T., Incropera, F. P., and Viskanta, R., 1990, "Local Convective Heat Transfer From a Heated Surface to an Impinging Planar Jet of Water," *International Journal of Heat and Mass Transfer*, in press.

Wang, X. S., Dagan, Z., and Jiji, L. M., 1989a, "Heat Transfer Between a Circular Free Impinging Jet and a Solid Surface With Nonuniform Wall Temperature or Heat Flux—1. Solution for the Stagnation Region," *International Journal of Heat and Mass Transfer*, Vol. 32, pp. 1351–1360.

Wang, X. S., Dagan, Z., and Jiji, L. M., 1989b, "Heat Transfer Between a Circular Free Impinging Jet and a Solid Surface With Nonuniform Wall Temperature or Heat Flux—2. Solution for the Boundary Layer Region," *International Journal of Heat and Mass Transfer*, Vol. 32, pp. 1361–1371.

Watson, E. J., 1964, "The Radial Spread of a Liquid Jet Over a Horizontal Plane," *Journal of Fluid Mechanics*, Vol. 20, pp. 481–499.

White, F. M., 1974, *Viscous Fluid Flow*, McGraw-Hill, New York.

Yamamoto, H., Udagawa, Y., and Suzuki, M., 1987, "Cooling System for FACOM M-780 Large-Scale Computer," *Proceedings of the International Symposium on Cooling Technology for Electronic Equipment*, Pacific Institute for Thermal Engineering, Honolulu, HI, pp. 96–109.

HEAT TRANSFER AND FLOW CHARACTERISTICS OF JETS IMPINGING ON A CONCAVE HEMISPHERICAL PLATE

Peter Hrycak

New Jersey Institute of Technology
Newark, New Jersey 07102 USA

ABSTRACT

Measurements of velocity profiles and static pressure distribution have been carried out on jets impinging on a concave hemispherical plate (CHP). In comparison with the flat plate (FP), the boundary layer at the stagnation point appears to be unchanged, but the potential core length is slightly shorter, while in the wall-jet region the inner boundary layer is thinner, and the velocity profile is somewhat steeper farther away from the plate. A formula has been derived for the maximum wall-jet velocity decay that agrees well with the experimental data. Heat transfer at the stagnation point is on CHP adversely affected by the presence of curvature, which also tends to make flow there more turbulent, as observed for the smaller diameter jets. The average heat transfer is independent of the nozzle-to-target spacing, in both the measured and the calculated version. The total heat transfer on a CHP is higher, caeteris paribus, than that corresponding to a FP, because of a larger surface area for the same diameter, for close target to nozzle spacings. It appears that the use of CHP of relatively small diameter as a target plate would enhance heat transfer from impinging jets.

1. INTRODUCTION

The results of experimental investigation of the flow characteristics and heat transfer from turbulent air jets impinging normally on a CHP are described below. Also, various phenomena directly related to fluid flow/heat transfer from impinging jets, are compared with our earlier work on free jets/jets impinging on a FP [1-3]. Jets impinging on a CHP (Fig. 1) have not been studied very extensively by previous investigators. Therefore, the experimental results here on hand describe phenomena which, in many instances, have never been observed before. The basic properties studied were pressure and velocity distributions in the free jet zone (but still within the hemispherical cavity), and pressure, velocity, and heat transfer along the CHP. In order to measure the total and static pressure within the CHP, suitable curved probes had to be developed, and a specialized traversing carriage had to be built. Heat transfer measurements were carried out in the steady state with 1/4 calorimeters mounted on an instrumented concave hemispherical target plate; the Reynolds number was varied from 12 000 to 88 000. It was based on the nozzle diameter and the air properties at the nozzle.

Heat transfer from impinging jets to curved surfaces is of a considerable theoretical and practical interest, because, as originally described by Thomann [4], heat transfer is increased in the turbulent boundary layer on the concave side, and decreased in the boundary layer on the convex side, in comparison with that on the flat plate, all due to the effects of curvature alone. Dyban and Mazur [5] found out that a two-dimensional jet impinging into a narrow cavity showed a mean heat transfer level 30 to 40% higher than a jet impinging on a FP. They attributed this to the hydrodynamic effects of curvature and the generally constricted flow geometry between the walls of the cavity and the nozzle itself.

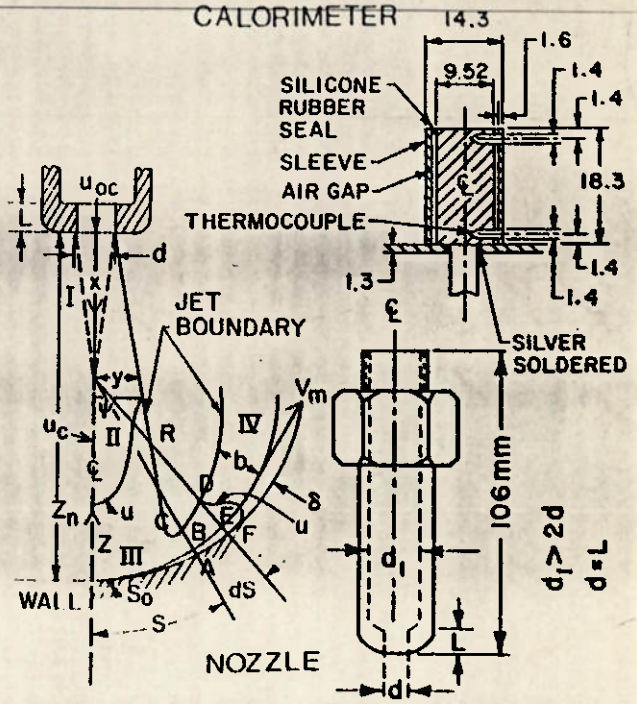

Note: $Re_d = u_{oc}d/\nu$; $Nu_d = \alpha d/\lambda$; $Nu_o = \alpha_o d/\lambda$

Figure 1 Geometry of Jet Impinging on Concave Hemispherical Plate; Zones: I Potential Core, II Free Jet, III Deflection, IV Wall Jet

It appeared, therefore, worthwhile to undertake a study of flow patterns and heat transfer of jets impinging on surfaces with double curvature, like a concave hemispherical cavity, since the results obtained with a single curvature looked so promising [5]. The first phase of this research involved a detailed study of flow patterns particularly relevant to heat transfer, like the

effects of curvature on the potential core of jet and on the free jet spreading, the boundary-layers at the stagnation point and in the wall-jet zone, and the study of the velocity profiles and of the maximum velocity decay there. Some of this work has also been done under this author's supervision by Jachna [6]. Simultaneously, local heat transfer measurements were carried out, in the hope that eventually, a better understanding of these findings will be possible through the proper interpretation of the relevant fluid flow measurements.

2. EXPERIMENTAL APPARATUS

The sketch of the piping system is shown in Fig.2. The compressed air was supplied by a reciprocating compressor, through a large storage tank to provide a steady flow. The air mass flow rate was measured with a pair of rotameters with a calibrated accuracy better than 1%. The inlet pressure at the rotameter was carefully monitored. The air went then through a 38 mm dia. pipe to a plenum chamber. The air temperature was measured before air entered the plenum chamber, 63.5 mm in dia. and 889 mm long, to which an end plate was welded on, where three different nozzles of 3.18, 6.35, and 9.52 mm dia. could be screwed on tightly. The plenum chamber was aligned vertically by adjusting three guide wires (cf. nozzle in Fig. 1).

Several large vertical column manometers, with mercury and water as a fluid, and, for low pressure measurement, a micromanometer, were available. A concave hemispherical brass plate with inside radius of 93.7 mm, shown in Fig.1, provided with twenty-nine 0.391 mm dia. holes for pressure taps to measure the local pressure distribution, was supported by three adjustable legs. The pressure probes were mounted on a stage whose position could be determined within 0.10 mm, with six degrees of freedom. Further experimental set-up details may be found in [6]. The nozzle was always kept vertical and the adjusted impingement surface horizontal, and the normal distance between the nozzle exit and the plate center could be changed from z_n/d= 3 to 20. The coordinate system is shown in Fig.1.

For heat transfer measurements, the hemispherical impingement plate in Fig.2 had to be replaced by a smooth ebonite hemisphere, of 155 mm internal diameter, and 18.3 mm thick, with holes drilled to accommodate fourteen 9.52 x 18.3 mm calorimeters, mounted flush with the surface. The calorimeters were made of 304 stainless steel whose conductivity as determined by the National Bureau of Standards [7]. They were located at the center of the plate, and, symmetrically at ψ= 11.5° and 22° (2 calorimeters at each angle, in one row), and at ψ= 35°, 56°, and 80.5° (3 calorimeters at each angle, arranged in rows 120° apart). The calorimeters were equipped with two 1.4 mm thermocouple holes at top and bottom, and were attached at the bottom by means of a soldered-on stud to a 1.3 mm thick hemispherical brass support plate. The support plate was heated on the convex side by steam condensing at atmospheric pressure, that was generated electrically in a boiler attached to the support plate. Each calorimeter hole was provided with a stainless steel sleeve; there was a 0.83 mm gap between sleeve and the calorimeter, sealed on top with silicone rubber, to act as a side wall insulator, Fig.1.

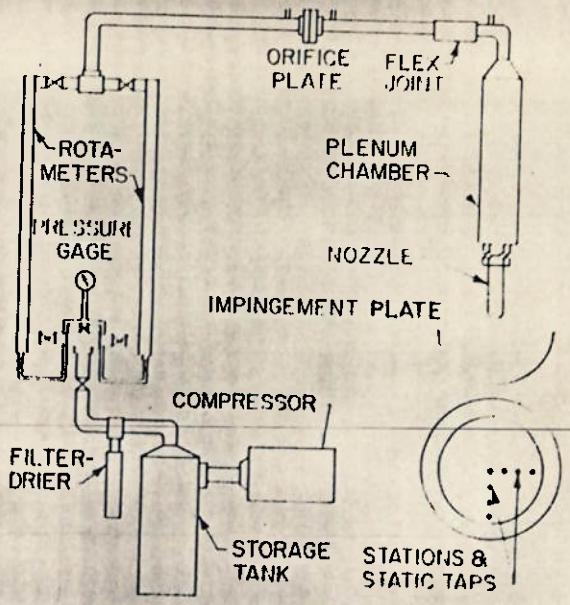

Figure 2 Experimental Test Set Up

3. EXPERIMENTAL FLUID FLOW RESULTS

Figure 3 shows the velocity decay along the jet centerline, with the normal distance between the nozzle exit and the center of CHP varied from four to twenty nozzle diameters, i.e., $4 < z_n/d < 20$. The Reynolds number was varied from 14 000 to 54 000; from inspection of the figure, it is seen

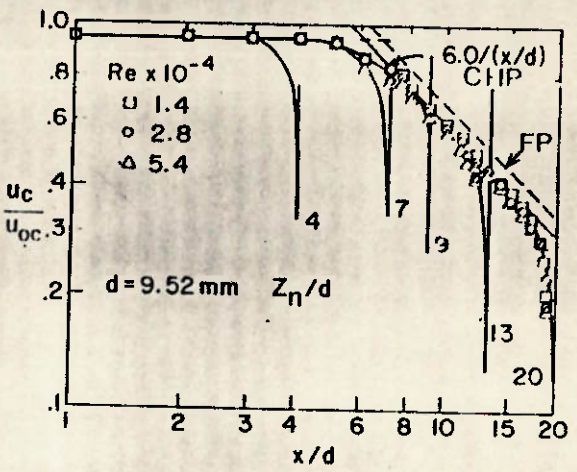

Figure 3 Decay of Centerline Velocity u_{oc} vs. x/d

that the nominal potential core length here is 2 ½ diameters shorter than in the case of a FP [1]. A similar observation has been also made by Jachna [6]. Otherwise, the velocity decay curves are similar to those observed on FP: the velocity is gradually decreased within one to three diameters away from the target plate, when flow nears the stagnation point. The data may be correlated by the formula

$$u_c/u_{oc} = 6.0/(x/d) \qquad (1)$$

The data for the spreading of the coordinate corresponding to one-half of the local velocity,

indicated $y_{\frac{1}{2}}/d = 0.0920(x-x_o)/d$, which is a spreading rate slightly lower than that for the free jet. There are also two spreading rates, one observed in the transition region, the other in the fully developed region (Zones I and II, respectively, Fig. 1). The mean velocity profile development in Zones I and II is similar to that of a free jet shown in [1], and which, for turbulent flow, is independent of the Reynolds number [6]. The sequence of the velocity profiles variation shows that as x/d increases, the velocity profiles outside of the potential core region become wider and flatter.

In the wall-jet region (Zone IV), the velocity profile in the outer layer, $z > \delta$, can be represented well by the equation (cf. [8])

$$u = V_m[1 - |(z-\delta)/\ell|^{3/2}]^2 \qquad (2)$$

for both the FP and CHP, except for $z/z_{\frac{1}{2}} > 1.2$, where the measured velocity profile for CHP has a steeper slope [6,9]. In the inner layer of the wall jet, $z < \delta$, the velocity profile follows the empirical equation

$$u = V_m(z/\delta)^{1/n} \qquad (3)$$

with $7.5 < n < 15$. This high n-value has been observed independently by several investigators [1,2, 11] as characteristic of wall jets.

Static pressure along the jet centerline generally varies slightly with z_n/d and the Reynolds number Re_d. It becomes eventually negative and reaches a minimum at $z_n/d \approx 7$, its variation being similar to that of a free jet [1,6]. In the neighborhood of the target plate, static pressure is then suddenly increased. Negative static pressure in the jet mixing zone is explained by existence of pressure gradients necessary to entrain the ambient air in the process of mixing. There is no observable effect of Re_d on static pressure distribution on the target plate itself, which is similar to that of the FP. When s/d gets larger, the static pressure on the wall of the CHP becomes eventually lower than the ambient pressure, which is known as the Coanda effect.

The boundary layer, δ, for the CHP is shown in Fig. 4. The boundary-layer thickness near the stagnation point, calculated with the theoretical formula $\delta/d = 1.98(n^*Re_d)^{-0.5}$ (cf. Schlichting, [11], p. 109), and the empirical expression $\delta^*/(z_n/d)^{1.25}$ [9], obtained from FP measurements, agree reasonably well with the CHP data shown in Fig. 4. Also, in the immediate neighborhood of the stagnation point, δ/d stays constant, and there is no evidence of thinning out at some point slightly away from there. The inner boundary layer development of the wall jet (Zone IV) may be also deduced from Fig. 4 as:

$$\delta/d = 0.0120(R/d)(\psi - \psi_o) \qquad (4)$$

which is compared with the expression

$$\delta/d = 0.0179\,(r/d)^{0.95} \qquad (5)$$

found for the FP. It is roughly equal to 1/10 of ℓ, the width of the outer layer of the wall jet that according to Jachna [6] is

$$\ell/d = 0.226(R/d)(\psi - \psi_o) \qquad (6)$$

The growth of the half-valued velocity thickness along the CHP is: $z_{\frac{1}{2}}/d = 0.068[1+0.014(z_n/d-4)]$.

$(R/d)(\psi - \psi_o)$ is similar to the corresponding FP expression, which also depends on z_n/d slightly and is proportional to $(r/d)^{0.95}$.

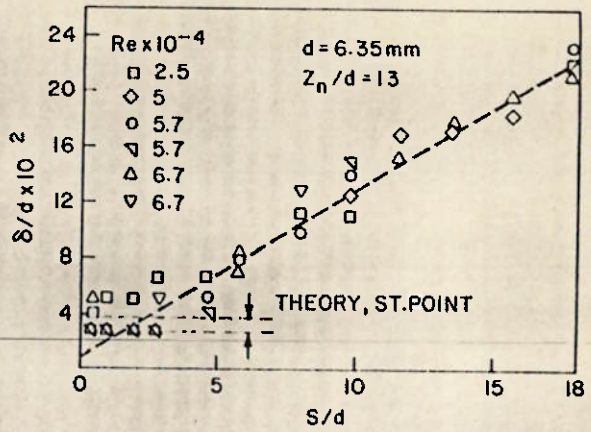

Figure 4 Inner Boundary Layer Development

Figure 5 shows the maximum velocity decay along the target plate for several z_n/d values, as observed by Jachna [6]. The maximum wall-jet velocity, V_m, increases at first to a maximum, located at $1 < s/d < 3$. The velocity profiles in the deflection region (for, approximately, $s/d < 4$) are similar to those of a FP, but have a slightly steeper slope. The slope of the maximum velocity decay curve becomes nearly horizontal near the rim of the CHP, while V_m is slightly dependent on z_n/d. This result is different from that for a FP, where V_m is inversely proportional to $(r/d)^{-1.12}$, and the z_n/d dependence exists only for very small r/d values. V_m, normalized with respect to V_m at $\psi = 10.9°$, can be represented by the empirical equation [6]

$$V_m/V_{10.9} = [5.29\psi\cos(\psi/2)]^{-1} \qquad (7)$$

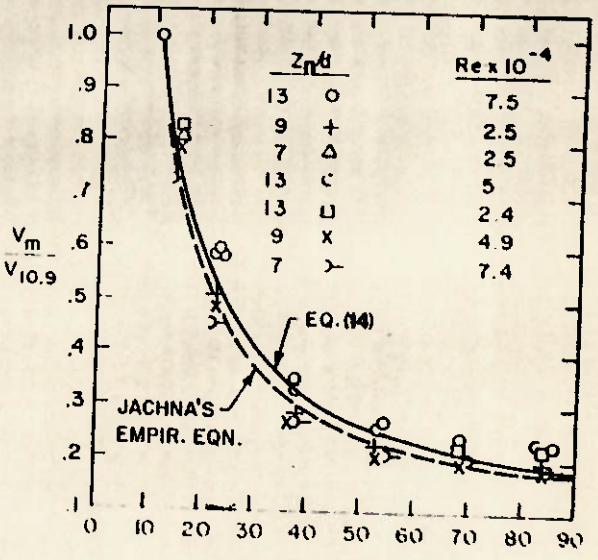

Figure 5 Maximum Velocity Decay in Wall Jet

Discussion of experimental results. The incompressible, turbulent jets impinging on a CHP in many respects are similar to the jets impinging on a FP. The observed differences are due to effects

of curvature and to a slightly higher turbulence (Tu) level inside of the CHP. They show up in a different maximum velocity decay pattern, in portions of wall jet velocity profiles, and a smaller inner boundary-layer and half-valued wall jet spreading thickness. The observed decrease of C in eq.(1) with respect to that of a FP may be explained using Schlichting's equation for the centerline velocity of a developed jet ([11], p. 748); with $u_o = k\, u_{oc}$, and the virtual kinematic viscosity ϵ_o,

$$u_c/u_{oc} = k^2\,(3d/32x)\,Re_d\,(\nu/\epsilon_o) \qquad (8)$$

If we let $\epsilon_o/\nu = m\,Re_d$ (m = const), there results

$$u_c/u_{oc} = k^2\,(1/32m)/(x/d) = C/(x/d) \qquad (9)$$

C in eq.(9) is independent of Re_d, as m may be expected to stay constant with a constant Tu and Re_d. Here, the increase in Tu within the hemispherical cavity brought about a 10% reduction in the magnitude of the nominal potential core of jet impinging on CHP. This is in line with observed substantial reductions in C of the artificially turbulized jets (C disappeared at Tu =28%, cf. Dyban and Mazur [12]); thus, as Tu and m go up, C goes down, for a constant Re_d.

Derivation of maximum velocity decay formula. It is of some theoretical and practical interest to show that the maximum velocity decay expression in Fig.5 may be derived in a way that well illustrates the closely interrelated features of several kinds of wall jets, by treating them in a unified fashion. Using the modified Pohlhausen-von Karman approach, we have according to Fig.1, for the mass dm entering the control volume ABEF·R $\sin\psi\, d\varphi$ (with the negative sign due to the effects of curvature)

$$dm = -\frac{dR}{ds}\int_o^{\delta} u\,\sin\psi\, dz\, d\varphi ds \qquad (10)$$

Then, using eq.(10), we get the momentum change expression for the volume BCDE·R $\sin\psi\, d\varphi$

$$\frac{d}{ds}\left[R\int_o^{\delta+b} u^2(1 - z/R)\sin\psi\, dz\, d\varphi\right] ds$$

$$- V_m \frac{d}{ds}\left[R\int_o^{\delta} u(1 - z/R)\sin\psi\, dz\, d\varphi\right] ds = \tau_\delta \qquad (11)$$

If $\tau \propto \partial u/\partial z$, $\tau_\delta = 0$ at $z = \delta$ in eq.(11) in accordance with the older Prandtl hypothesis [11]. Physical results below and in [1,2] indicate that this assumption in eq.(11) is justified..

Equation (11) has been found useful for other geometries. Thus, on letting $\sin\psi \equiv 1$, $ds \to dr$, $R \to r$, and changing the sign of the second term, eq.(11) describes behavior of an axisymmetric jet (Hrycak et al., [1,2]). If, additionally, $d\varphi \equiv 1$, and $ds \to dx$, and R is deleted, an expression for a two-dimensional jet is obtained (cf. Abramovich [8]). We may now write eq.(11) in the form $I_1 - I_2 = 0$. Using u from eq.(3), with n = 14, for $z < \delta$, and u from eq.(2) for $\delta < z < b$, $b < R/3$ (cf. Fig. 1), and $\delta \approx b/13$ (according to [6] and Fig. 4), and substituting $\bar V_m = V_m/u_{oc}$, $\bar\delta = \delta/R$, $\bar b = b/R$, and $dx = d(R\psi)$, we finally get

$$I_1 = \left[\bar V_m \frac{dR}{d\psi}\left[\bar\delta\,\bar V_m \sin\psi\right]\frac{n\, d\varphi}{(n+1)}\right] u_{oc}^2\, d\psi \qquad (12)$$

with an error of 1%. Similarly, letting $(z-\delta)/b = \xi$, and also noting that, for $\delta < z < b$, $d[(R-\delta)\psi] = ds$, and

$$\int_o^1 u^2\, d\xi = 0.31559, \quad \int_o^1 u^2 \xi\, d\xi = 0.0668,$$

$$I_2 = \left[0.31559\,\frac{dR}{d\psi}\left[\bar b\,\bar V_m \sin\psi\right]d\varphi\right] u_{oc}^2\, d\psi \qquad (13)$$

with an error < 4%. After some simple transformations, with $\beta = 0.31559(n+1)\bar b/(n\bar\delta) = 6.0864$, $I_1 - I_2$ integration, with C' = const. of integration, leads to

$$V_m = C'(\bar b\,\sin\psi)^{(1-\beta)/(\beta-1)} = C\,(\psi \sin\psi)^{-0.4552} \qquad (14)$$

Equation (14) is shown in Fig. 5, in a normalized form, to follow the mean of experimental results for all z_n/d values rather closely. Using eq.(6) for b, and the experimental measurements of δ (both our own and from [6]), $\psi \approx 77.5°$ corresponding to that of the heat transfer surface, and d= 6.35 mm, the C in eq.(14) is evaluated as $0.2967\,(R/d)^{-0.4552}$. A $\psi = \pi$ in eq.(14) (for the theoretical case of no friction), $V_m = 7_{max}$, a boundary reference velocity that also follows the data in [6]. V_m from eq.(14) will be used later in heat transfer calculations.

4. EXPERIMENTAL HEAT TRANSFER RESULTS

Heat transfer measurements were carried out with the experimental set-up shown in Fig.2, with the hemispherical impingement plate for fluid flow measurements having been replaced by the hemispherical instrumented heat transfer plate with 14 calorimeters and with an attached steam generator, as described above in the "Experimental Apparatus" section. The measurements had been carried out (with some inevitable reruns) for more than 200 test points. The heat transfer coefficients were then calculated from the relations

$$\alpha = -(\lambda/N)(\theta_t - \theta_b)/(\theta_s - \theta_{air}) \qquad (15)$$

where surface temperature θ_s was obtained from

$$\theta_s = \theta_t + (\theta_t - \theta_b)(M/N - 1) \qquad (16)$$

where subscript b refers to the bottom thermocouple on the calorimeter, t to the top thermocouple, and M,N = distance between locations where θ_s and θ_b, and θ_t and θ_b, respectively, had been measured. Proper insulation on the sidewall of the calorimeter, a good thermal contact with the base plate, and the elimination of the thermocouple conduction error were essential for the accurate determination of α, while a relatively small calorimeter diameter was helpful in getting better local measurements, according to the equation

$$Nu = K\,Re^a\,Pr^b\,(z_n/d)^c(d/d_c)^d(d_p/d)^e(z/d)^f \qquad (17)$$

based on the dimensional analysis of the problem on hand. Here, a = 0.5 and b = 0.4 could be expected for the stagnation point data in line with the theoretical solution by Sibulkin [13], while for the average Nusselt number, $0.6 < a < 0.7$, and b = 0.33 appeared appropriate.

The experimental results for the stagnation point are shown in Figures 6 and 7. It is interesting to see that for the 3.18 mm dia. nozzle, the Nu-dependence on the nozzle-to-target spacing, z_n/d, is different from that for the two larger nozzles used, and the power of the Reynolds number suggests that flow is already highly turbulent:

$$Nu_o = 0.795\ Re_d^{0.604}\ Pr^{0.4}(z_n/d)^{-0.22} \qquad (18)$$

as shown in Fig. 6, while for d = 6.35 and 9.52 mm, the stagnation flow has still essentially laminar characteristics (all applicable for $3 < z_n/d < 7$)

$$Nu_o = 0.666\ Re_d^{0.5}\ Pr^{0.4}\ (z_n/d)^{0.17}(d/d_c)^{0.07} \qquad (19)$$

Here, Re_d to one-half power occurs (as it does in Sibulkin's solution [13]); the $(z_n/d)^{0.17}$ term is virtually identical with the corresponding FP expression described in [9]. Evidently, the differences between equations (18) and (19) are due to the lack of complete geometrical similarity here; since the plate diameter d_c is kept constant, for the same z_n/d values, the 9.52 mm nozzle is three times, and the 6.52 mm nozzle, two times as far away physically from the target plate as the 3.18mm dia. nozzle, for the same z_n/d value. Thus, the influence of the curvature of walls (with its increased turbulence) overrides here the effects of the developing jet core, with the associated high turbulence for $6 < z_n/d < 7$, and an otherwise increasing turbulence as we proceed away from the nozzle within $z_n/d < 7$. This "potential core" effect was first identified and explained by Gardon and associates [14,15], while the "curved wall" effect with $(z_n/d)^{-0.22}$ term has occurred already in expressions describing a row of round jets impinging on a semi-cylindrical surface (cf. [16] and [3]).

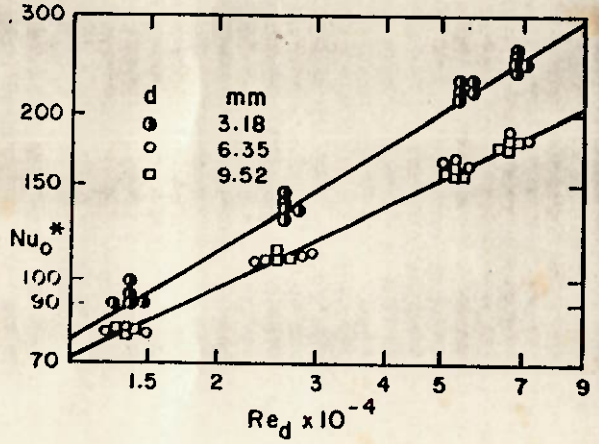

Figure 6 Stagnation Point Heat Transfer, Hem. Data

$$Nu_o^* = Nu_o/\left[Pr^{0.4}\ (z_n/d)^{-0.22}\right],\quad d = 3.18\ mm$$

$$Nu_o^* = Nu_o/\left[Pr^{0.4}(z_n/d)^{0.17}(d/d_c)^{0.07}\right],\quad d = \begin{cases}6.35\\9.52\end{cases}\ mm$$

To test further the effect of curvature on stagnation point heat transfer, an experiment has been carried out where a smaller diameter (d = 3.18 mm), high resolution calorimeter was tested on a FP with and without curvature, under otherwise nearly identical conditions. The curvature was provided by a nearly hemispherical plastic surface of 127 mm dia., in which a smoothly contoured opening of 0.76 mm dia. was cut out at the center, so that it would keep just the calorimeter exposed to the jet. Results are shown in Fig.7: for the 9.52 mm nozzle, only the heat flux intensity changes, registering a decrease of 21% at Re_d = 16 000 and of 14% at Re_d = 63 000. The changes for the 6.35 mm nozzle were even more pronounced: in addition to a lowering of heat flux intensity, the slope also increased from 0.5 to 0.66. In view of the discussion by Gardon and Akfirat [15] about significance of turbulence on the stagnation point heat transfer and the experiments of Dyban and Mazur with turbulized jets [12] it becomes obvious, that the curvature has here the destabilizing, turbulence increasing effect predicted by Thomann [4] that leads to a decreased local heat transfer at the stagnation point in the case at hand. Additionally, in the situation like the one shown in Fig.7, the circulation of the fluid is impeded by the built-on curvature.

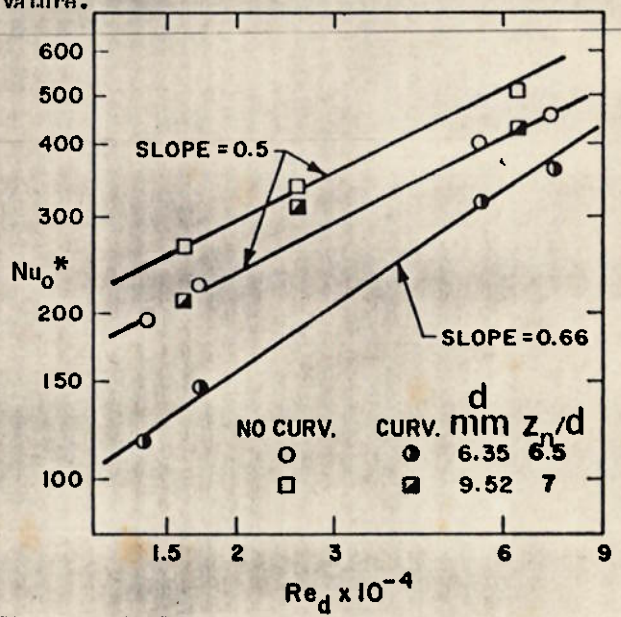

Figure 7 Influence of Curvature on Stagnation Point Heat Transfer

The average heat transfer for the HP is shown in Fig. 8. For $3 < z_n/d < 7$ it may be correlated by the expression below (with d_p = 2R)

$$\overline{Nu}_d = 2.51\ Re_d^{0.604}\ Pr^{0.33}\ (d/d_p)^{1.07} \qquad (20)$$

essentially independent of z_n/d for $z_n/d < 7$. Equation (20) shows some similarity to the average FP results mentioned in [9] and [16], according to which $\overline{Nu}_d$ = 164 vs. 98.2 by eq.(20) for Re_d = 67 000, d = 9.52, and d_p = 155 mm, for example. Because a hemisphere has an area larger than the inscribed circle, the total heat flux would have been here still higher for $\overline{Nu}_d$ from eq.(20). A substantial portion of the present heat transfer data have been analyzed by Livingood and Gauntner [17]. They lumped together the stagnation point results for all three nozzles, getting in their correlation a negligible dependence on z_n/d, but their $\overline{Nu}_d$ expression is similar to our eq.(20).

5. HEAT TRANSFER CALCULATIONS FOR CONCAVE HEMISPHERICAL PLATE

In view of the Fig. 4 data, one could expect here heat transfer at stagnation point to be physically similar to that given by Sibulkin's solu-

tion [13]; it gives results compatible with eq.(19) for moderate z_n/d values. The present data are complete enough to calculate also the average Nusselt value from the relation $C_f/2 = St\ Pr^{2/3}$, where

$$C_f/2 = 0.123\ (V_m \delta_2/\nu)^{-0.268} \cdot 10^{-0.678\delta_1/\delta_2} \qquad (21)$$

is a two-parameter formula due to Ludwieg and Tillmann ([11], p. 699), good for three-dimensional flow with pressure gradients. δ_1 and δ_2 are displacement and momentum thickness, defined by

$$\delta_{1,2} = \int_0^\delta (u/V_m)^1 (1 - u/V_m)\ \sin\psi\ dz, \quad l = 0,1 \qquad (22)$$

in view of the geometry of the problem, $\delta_1/\delta_2 = 7/7$ and $\delta_2 = 7\delta\ \sin\psi/120$, on choosing $n = 14$ in eq.(3). After b, V_m, δ_1 and δ_2 (from eqs.(6),(14),and (22)) are substituted in the $Cf/2 = St\ Pr^{2/3}$ relation,

$$Nu_d = 0.0591\ Re_d^{0.732} Pr^{0.333} (R\psi \sin\psi/d)^{-0.6012}$$

is obtained, which, integrated over the entire hemisphere, yields

$$\overline{Nu}_d = 0.151\ Re_d^{0.732}\ Pr^{0.333}\ (d/d_p)^{0.6012} \qquad (23)$$

Except for the numerical constant and the powers of d/d_p and Re_d that were generated in the process of calculation with the L-T formula, eqs.(23) and (20) are of the same structure, and produce reasonably similar Nusselt numbers. Thus, for $Re_d = 6.7 \times 10^4$, they are 88.2, 69.1 and 45.3 vs. 94.1, 61.1 and 29.1, for d=9.52, 6.35 and 3.18 mm, respectively. For $Re_d = 1.4 \times 10^4$, these figures are 28, 22 and 14.5 vs. 36.6, 23.7 and 11.3. It is understood, the use of the L-T formula represents an application for which it was not originally intended. The encouraging physical results justify its use here, however, until a better formula becomes available.

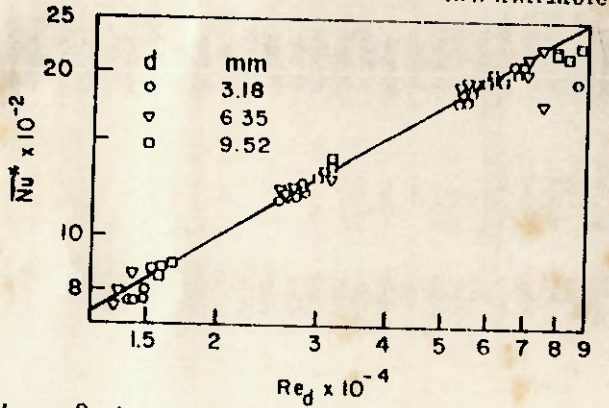

Figure 8 Average Heat Transfer, Hem. Plate
$\overline{Nu}_d^* = \overline{Nu}_d / [Pr^{0.333}\ (d/d_p)^{1.07}]$; $\overline{Nu}_d = \bar{\alpha} d/\lambda$

ACKNOWLEDGMENT

This work has been partially supported under contract NAS3-11175. Dr. R. Nagaraja helped with the collection and processing of the data.

NOMENCLATURE

a^*	dimensionless velocity profile, stagn. point
b	width of jet, m
r	radius of flat target plate, m
R	radius of hemispherical target plate, m
s	length of arc on hemispherical target plate, m
z_n	vertical nozzle-to-plate distance, m

Subscripts

c	condition near center of symmetry, calorimeter diameter, m
o	condition near stagnation point or at nozzle
p	referring to target plate

REFERENCES

1. Hrycak, P., Lee, D.T., Gauntner, J.W., and Livingood, J.N.B., Experimental Flow Characteristics of a Single Turbulent Jet Impinging on a Flat Plate, NASA TN D-5690, Washington, D.C. 1970
2. Hrycak, P., and Lee, D.T., Calculation of Maximum Velocity Decay in Wall Jets, J. of Spacecraft and Rockets, vol. 7, pp. 623-625, 1970
3. Hrycak, P., Jachna, S., and Lee, D.T., A Study of Characteristics of Developing, Incompressible, Axisymmetric Jets, Letters Heat Mass Transfer, vol. 1, pp. 63-72, 1974.
4. Thomann, H., Effect of Streamwise Wall Curvature on Heat Transfer in a Turbulent Boundary layer, J. Fl. Mechanics, vol. 33, pp.283-292, 1968.
5. Dyban, Ye.P., and Mazur, A.I., Heat Transfer from a Flat Jet Flowing into a Concave Surface, Heat Transfer-Soviet Res., vol.2, pp.15-20, 1970.
6. Jachna, S., Axisymmetric Jet Impinging on a Hemispherical Concave Plate, D.Sc. Dissertation, NJIT, Newark, NJ, 1978.
7. Flynn, D.R., Calculation of Thermal Conductivity and Thermal Resistivity of AISI Type 304 Stainless Steel, NBS Report 9869, 1968.
8. Abramovich, G.N., The Theory of Turbulent Jets, MIT Press, Cambridge, Mass., 1963.
9. Hrycak, P., Heat Transfer from a Row of Impinging Jets to Concave Cylindrical Surfaces, Int. J.Heat Mass Transfer, vol.25, pp.407-419, 1982.
10. Schwarz, W.H., and Cosart, W.P., The Two-Dimensional Turbulent Wall Jet, J. Fl. Mechanics, vol. 10, pp. 481-495, 1961.
11. Schlichting, H., Boundary-Layer Theory, 7th ed., McGraw-Hill, 1979.
12. Dyban, Ye.P., and Mazur, A.I., Heat Transfer in the Vicinity of the Stagnation Point Produced by Impingement of a Turbulized Jet with a Baffle, Heat Transfer-Soviet Res., vol. 11, No. 1, pp. 52-58, 1979.
13. Sibulkin, M., Heat Transfer Near the Forward Stagnation Point of a Body of Revolution, J. Aer. Sciences, vol. 19, pp.570-571, 1952.
14. Gardon, R., and Cobonpue, J., Heat Transfer between a Flat Plate and Jets Impinging on It, Int.Dev.Heat Transfer, ASME, pp.454-460, 1962.
15. Gardon, R., and Akfirat, J.C., The Role of Turbulence in Determining the Heat Transfer Characteristics of Impinging Jets, Int.J. Heat Mass Transfer, vol. 8, pp. 1261-1272, 1965.
16. Hrycak, P., Heat Transfer from a Row of Jets Impinging on a Concave Semi-Cylindrical Surface, Proceedings, 6th Int. Heat Transfer Conference, Paper FC-11, vol. 2, pp. 67-72, 1978.
17. Livingood, J.N.B., and Gauntner, J.W., Heat Transfer Characteristics of a Single Circular Jet Impinging on a Concave Hemispherical Shell, NASA TM X-2895, 1973.